TÉCNICO LISBOA

From Light-Front Wave Functions to Parton Distribution Functions

Eduardo Pereira de Oliveira Bento Ferreira

Thesis to obtain the Master of Science Degree in

Engineering Physics

Supervisors: Dr. Gernot Eichmann
Prof. Dr. Alfred Stadler

Examination Committee

Chairperson:	Prof. Dr. Ilídio Pereira Lopes
Supervisor:	Dr. Gernot Eichmann
Member of the Committee:	Prof. Dr. Tobias Frederico

November 2021

To all my friends and family.

Acknowledgements

I would like to use this opportunity to thank a large number of people that I had the fortune of meeting and interacting with throughout this journey (of both writing this thesis, and the university years).

First, I would like to start by thanking both my supervisors, Dr. Gernot Eichmann and Prof. Dr. Alfred Stadler for their extraordinary support in this process. From answering all my questions, to giving me their excellent professional advice, while making me always feel welcome and a part of the team, I could not have asked for better mentors. I would also like to thank LIP and the NPStrong group for welcoming me so warmly.

Next, I would like to thank my friends from secondary school: Miguel Barros, Miguel Chorão, Garcia, Hugo, Marcelo, Vasco e Valente for making that experience such a fun and awesome time.

I also want to thank everyone that I worked with during my two years at NFIST, either from the first year or the second, in which I had the opportunity to be the president (a particular mention must be done to my vice-president Mariana). Those two years were one of the most rewarding things I have done these years.

I am also grateful to all my good friends that I had the pleasure to gain during these times at Técnico: Ana, João ”Braga” Pedro, Caçador, Clara, Diogo Ribeiro, Gaspar, Loureiro, Mariana, Pedro Duarte and Rafael Rodrigues. You have made this experience way more epic and memorable. I will take with me all the countless hours either working together or just having fun (and the two at the same time).

I want to thank my family for their unconditional support and affection. In particular to my father, to my mother and my brother who were always completely supportive and caring. Their constant affection, and guidance (when needed) were fundamental for me to become what I am today.

Lastly, but not least, I would like to wholeheartedly thank the extraordinary Beatriz. For all the support, for all the motivation, for the advice, for the company, for the fruitful discussions, for the general awesomeness of her personality. She was truly fundamental through these years, and for that I am deeply thankful.

Resumo

O objetivo desta dissertação é calcular as funções de onda na frente-de-luz (LFWFs) de estados ligados, a partir da sua funcão de onda de Bethe-Salpeter (BSWF).

A determinação das LFWFs é muito importante no estudo dos hadrões — partículas compostas por quarks e gluões, descritos pela Cromodinâmica Quântica (QCD). O estudo dos hadrões na frente-de-luz possibilita o cálculo de funções de estrutura hadrónicas que descrevem, por examplo, distribuições de momento e spin entre os seus constituintes, como as funções de distribuição de partões (PDFs) que descrevem a distribuição de momento no hadrão.

Nesta dissertação propomos um novo método para o cálculo da LFWF de valência de um sistema de duas particulas interatuantes, baseado na deformação dos caminhos de integração na solução da equação de Bethe-Salpeter, juntamente com métodos de continuação analítica para projetar a BSWF na a frente-de-luz.

Começamos com uma revisão da teoria de estados ligados em QCD, seguindo-se uma descrição da dinâmica da frente-de-luz e do modelo escalar utilizado. Posteriormente, o método de deformação de caminhos será definido, seguido de uma análise dos métodos numéricos utilizados. Os resultados obtidos estão de acordo com os resultados obtidos através do método de Nakanishi, muito utilizado na literatura.

Finalmente, demonstramos que o novo método consegue lidar com a introdução de partículas de massas diferentes e a introdução de um par conjugado complexo de pólos de massa nos propagadores das partículas. O objectivo destas extensões é imitar algumas caracteristicas que poderão vir a ser relevantes numa aplicação do método proposto à QCD.

Palavras-chave: Hadrões, Cromodinâmica Quântica (QCD), Função de onda de Bethe-Salpeter (BSWF), Função de onda da frente de luz (LFWF), Deformações do caminho de integração

Abstract

Our goal is the calculation of the light-front wavefunctions (LFWFs) of bound states from their Bethe-Salpeter wavefunction (BSWF).

This problem is of great importance, for example, in the study of hadrons — the particles composed of quarks and gluons described by Quantum Chromodynamics (QCD). The study of hadrons on the light-front allows for the calculation of several hadronic structure functions that encode, for example, the momentum and spin distributions of their constituents, like the parton distribution functions (PDFs) which describe the momentum distribution inside the hadron.

We propose a new method to calculate the valence LFWF for a system of two interacting particles based on the use of contour deformations in the solution of the Bethe-Salpeter equation, combined with analytic continuation methods for projecting of the obtained BSWF onto the light front.

We start by reviewing of the theory of bound states in QCD, followed by a description of light-front dynamics and a description of the scalar toy model used as a proof of concept. The contour deformation method is then defined, along with a brief review of the numerical methods used. The results obtained with the new method are in excellent agreement with the results obtained with the Nakanishi method used in the literature.

We finally show that the contour deformation method is capable of handling the introduction of particles of different masses and complex conjugate mass poles in the propagators of the particles – mimicking some features that might be relevant in applications of the method to QCD.

Keywords: Hadrons, Quantum Chromodynamics (QCD), Bethe-Salpeter Wavefunction (BSWF), Light-Front Wavefunction (LFWF), Contour Deformations

Contents

List of Tables

List of Figures

Nomenclature

Mathematical symbols and physical constants

g	Coupling constant (as it appears in the Lagrangian)
D^μ	Covariant derivative
z^*	Complex conjugate of z
$\Box^2 = \partial^\mu \partial_\mu$	D'Alembertian operator
$\delta(x)$	Dirac delta function
γ^μ	Dirac gamma matrices
$\Gamma(x)$	Gamma function
A^μ	Gluon field
$\theta(x)$	Heaviside step function
i	Imaginary unit
δ_{ij}	Kroenecker delta function
$\mathcal{L}$	Lagrangian function
$\mathbb{C}$	The set of complex numbers
$\mathbb{R}$	The set of real numbers

Abbreviations

BSWF	Bethe-Salpeter Wave Function
DχSB	Dynamical Chiral Symmetry Breaking
DIS	Deep Inelastic Scattering
DSE	Dyson-Schwinger Equation
GPD	Generalized Parton Distribution
LF	Light-Front (as in Light-Front Dynamics)
LFWF	Light-Front Wave Function
PDF	Parton Distribution Function
QCD	Quantum Chromodynamics
QED	Quantum Electrodynamics
QFT	Quantum Field Theory
SLAC	Stanford Linear Accelaration Center
SM	Standard Model
SU$(\mathbf{n})$	Special Unitary group of rank n
TMD	Transverse Momentum Distribution
UV	Ultraviolet

Chapter 1

Introduction

1.1 Quantum Chromodynamics

The study of the strong force is deeply related to the history of the study of the atom and its nucleus. Atomic nuclei are made of protons and neutrons tightly bound together by the strong force. This structure was hinted at by the regularities found in Mendeleev's periodic table and Rutherford's gold foil experiment — the first showed that atoms were built of smaller particles [1] and the latter showed that the atom was made from a nucleus surrounded by electrons [2].

The discovery of other strongly interacting particles, the hadrons, such as the *pion* and the *kaon* led to the introduction of the *eight-fold way* [3] as a way to organize them. This would later lead to the proposal that these particles were made of something more fundamental — more specifically, Gell-Mann and Zweig proposed the existence of quarks [4–6]. Experimental evidence for the quarks would be obtained for the first time in 1968, in the Stanford Linear Accelerator Center (SLAC), in electron-proton collision events [7]. There is, however, a fundamental problem with the eight-fold way: the Pauli principle is violated for some cases. A new quantum number is required to solve this issue. In this perspective, the notion of the color quantum number appears, which is then systematically introduced through Quantum Chromodynamics (QCD).

QCD is the currently accepted theory that describes the strong interaction. It is a gauge theory that arises by requiring that a Lagrangian is invariant with respect to a local $SU(3)$ symmetry. This defines a *color charge* (hence, chromodynamics), analogous to the electric charge of the theory of electromagnetic interactions (quantum electrodynamics, QED). In the Standard Model, quarks are the only fermions that have color, and their strong interactions are mediated by the exchange of gluons, which, in contrast to the photons from QED, do have color charges as well (this implies that gluon-gluon interactions are possible — this comes from the fact that $SU(3)$ is non-Abelian).

Due to quantum corrections, the magnitude of the strong interaction varies with the energy scale of the participants in what is known as the *running of the coupling constant* α_{QCD}. It is large at low energy scales and becomes increasingly small for larger energy scales. Even though it decreases with the energy scale, the strong interaction is still *stronger* (as the name would imply) than the other interactions — for example, at an energy scale equal to the Z boson mass, $Q = M_{Z^0}$, $\alpha_{QED} \approx \frac{1}{127}$ while $\alpha_{QCD} \approx 0.12$, about 15 times stronger [8].

In QCD, the decrease of the value of the coupling constant with the energy scale is called Asymptotic freedom. This implies that, at high energies (equivalent to small separations between the particles), the strong interaction is very weak, and particles behave almost as if they were free. On the other hand, the increase of the coupling strength with smaller energy scales (equivalent to larger distances

between the particles) is called *confinement* [9]. Together with asymptotic freedom, confinement is one of the emergent features of QCD, and in practice, this means that quarks cannot be observed directly in experiments — they will always appear bound with other quarks in a colorless combination. Any experiment that attempts to study the behavior of QCD must always include hadrons — the quark and gluon bound states, like the proton.

Confinement has another quite striking consequence: as α_{QCD} increases, it will eventually reach a point where $\alpha_{QCD} > 1$. In this region, the perturbative methods that work very successfully with the other interactions will no longer be valid. Usually, the QCD *Landau pole* (the point where perturbative calculations show a divergence in the coupling constant) at $Q = \Lambda_{QCD} \approx 200$ MeV [8] is defined as the boundary between the two regimes. As Λ_{QCD} is in the same order of magnitude as the energy scale of a large number of hadrons — namely the lighter ones such as the proton, neutron, and pion — means that, to study hadrons, one cannot use perturbative methods. A different toolset will be needed to be able to understand QCD at those energy scales — methods such as Lattice QCD [10], effective field theories [11, 12], and functional methods are invaluable assets [13, 14].

1.2 Hadrons and Parton Distribution Functions

Several experiments have been dedicated to the study of hadrons, for instance, HERA, RHIC, and the LHC. Others have been proposed and are in construction, such as the Electron-Ion Collider at the Brookhaven National Laboratory [15] and COMPASS/AMBER at CERN [16].

By studying the results from these experiments one can determine several observable quantities. *Form factors* are some of them and they encode the behavior of the hadron when interacting with bosons. For example, the electromagnetic form factors relate to interactions with photons; the axial form factors relate to the weak bosons, W and Z and the pseudoscalar form factors relate to interactions with pseudoscalar particles such as the pion.

Other quantities that provide information on the internal structure of hadrons can be defined. An especially important subset of these hadronic quantities is the *Parton Distribution Functions* (PDFs). These functions, which are obtained in deep inelastic scattering (DIS) experiments — which consist in $e^- N$ scattering at high energies — encode the internal structure of the hadron, in terms of its partons. *Parton* is the name given to the internal quarks and gluons of a hadron.

In a more forma way, one can define a parton distribution function as a function $f_k(x, Q^2)$ such that $f_k(x, Q^2)dx$ gives the probability that a parton k has a fraction of the longitudinal momentum of the hadron between x and $x + dx$ [17]. These functions vary with the energy scale of the interaction Q^2. Different energy scales probe and reveal more or less detailed information about the constitution of the hadron.

It is easy to see why these functions are particularly important. On one hand, they allow for the study of the internal structure of the hadron. On the other hand, they are very important when analyzing the results of hadronic experiments. Unfortunately, calculating these functions is not simple as they are non-perturbative objects (from the discussion of asymptotic freedom and confinement in section 1.1). Our current understanding of PDFs comes mainly from experimental fits [18, 19] and Lattice QCD simulations [20–22]. Some work has also been carried out in the calculation of PDFs from functional methods [23–26].

One of the ways to calculate the PDFs starts by solving the bound state equation in QCD, the *Bethe-Salpeter Equation* (BSE). The outcome of this equation is the Bethe-Salpeter Wave Function (BSWF) and the mass of the hadron. The next step is to define these quantities in light-front dynamics ([27]) to extract the *Light-Front Wave Function* (LFWF) from the BSWF [28]. PDFs can then be defined as overlaps

of LFWFs [29].

The main challenge in this process is the transformation of the BSWF into the light-front wavefunction. One way to do this transformation is based on the Nakanishi method [30], which avoids numerical problems by defining a smooth weight function g that is used to derive all other quantities, such as the Bethe-Salpeter wavefunction and the light-front wavefunction [31, 32]. The main drawback of this method is that it is necessary to know, beforehand, the analytic structure of the interaction so that the function g can be defined.

In this work, a new method is proposed, which attempts to transform the BSWF to the LFWF directly. It combines contour deformations ([33]) that avoid crossing the singularities in the interaction and analytic continuation methods to do the projection of the BSWF onto the light-front.

1.3 Goals

As mentioned above, the main goal of this work is to present a new method that makes the calculations of LFWF numerically simpler.

To achieve this goal, a simplified model consisting of only scalar particles will be used instead of QCD, as a proof-of-concept. The idea is that by using a simpler theory (in the mathematical and physical sense), it is easier to understand the steps needed and what the main obstacles are. Some modifications of the scalar model, such as the inclusion of particles of different masses and complex conjugate propagator poles will be also studied to mimic some features that might be present in future applications of this method to QCD.

In this work, the BSE will be solved for two scalar particles, followed by the transformation to light-front dynamics and to the light-front wave function. In the end, the *Parton Distribution Amplitude* will be obtained, which gives the probability distribution for one of the two particles to have a specific momentum fraction of the hadron. These parton distribution amplitudes and light-front wave functions will be the starting point in future work for the determination of PDFs, both in the scalar model, and later on in QCD later on.

Additionally, other quantities are also defined in the light-front, such as *Transverse Momentum Distributions* (TMDs) and *Generalized Parton Distributions* (GPDs) that encode additional information on

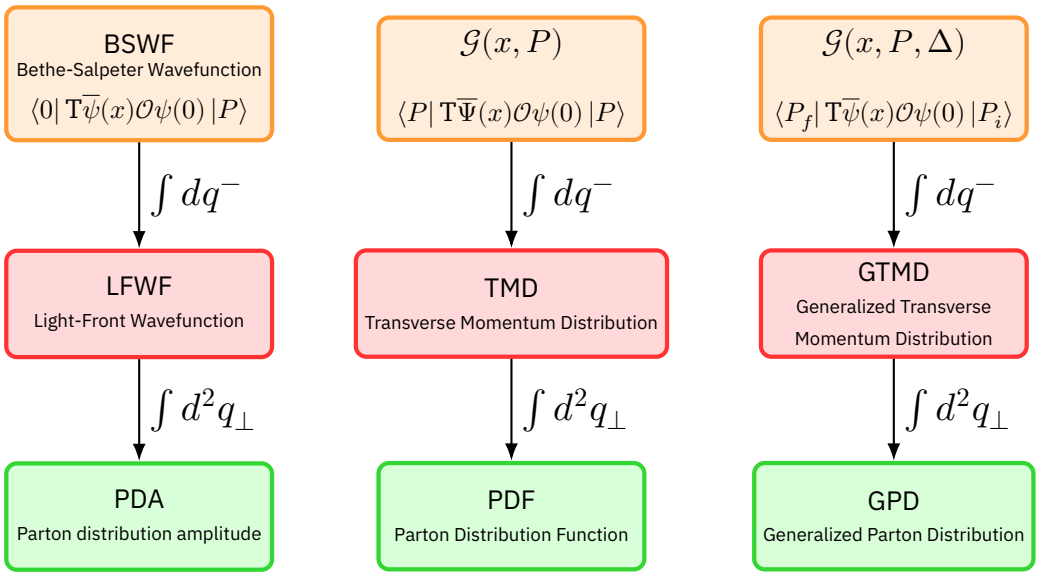

Figure 1.1: Relation between the hadronic correlations and distribution functions in the light-front.

spatial and momentum distributions, enabling what is known as *hadron tomography* [29]. These can be extracted from hadronic correlations in the same way the LFWFs can be extracted from the BSWF, like in figure 1.1 (more details in section 2.5.1).

1.4 Structure

This work is divided into 6 chapters, the first one being this introduction.

In Chapter 2, a brief overview of QCD is presented followed the standard framework for dealing with bound states in a quantum field theory (QFT) as well as the light-front formalism.

Afterwards, in chapter 3, the scalar toy model will be described, followed by a more detailed explanation of the Nakanishi method, which is used to provide a useful comparison for the results of this work. A definition of the proposed contour deformation method is then presented, alongside an overview of the numerical methods used.

Some results and the relevant comparisons with the Nakanishi method are shown in chapter 4.

Chapter 5 contains the extensions that can be made to the scalar model, such as the inclusion of scalar particles of different masses and complex conjugate poles in the propagators. All these additions can be introduced very easily in the proposed method with good results. Finally, closing remarks, as well as some conclusions and future lines of work, are discussed in chapter 6.

Chapter 2

Bound states and QCD

As discussed in the previous chapter, in section (1.3), the main goal of this work is to calculate light-front wavefunctions of two interacting particles.

To do so, we first must understand how bound-states are handled in a quantum field theory, focusing, naturally, on QCD. We start by giving a brief description of QCD, followed by a summary of the state spectrum of QCD and how hadrons can be observed through poles in the correlation functions of the theory. Afterwards, we show how to obtain the bound state equation, the Bethe-Salpeter equation, which is the relativistic analog of the Schrödinger equation for bound states. Finally, we show how to project the Bethe-Salpeter wavefunction to the light-front to be able to extract the light-front wavefunctions.

2.1 QCD Lagrangian

Quantum Chromodynamics is the QFT that describes the strong interaction. It is defined from a Lagrangian function $\mathcal{L}$ from where the equations of motion which dictate the evolution of its quantum fields (quarks and gluons) can be derived.

The starting points for building the QCD Lagrangian are the symmetries that are expected from the theory: Poincaré invariance and local $SU(3)$ gauge symmetry.

Poincaré invariance is, in essence, the requirement that the physical laws of QCD be equivalent in every reference frame. The fields must transform under rotations, boosts and translations according to their representation of the group — they have a well-defined spin. Quarks have spin $\frac{1}{2}$ and are represented by spinors ψ_α (α being the Dirac index), while the gluons are Lorentz vectors with spin 1, represented by A^μ (with μ representing the Lorentz index) [17].

On the other hand, local $SU(3)$ gauge symmetry demands that the theory is invariant for local transformations (ones that have a space-time dependency) of the quark fields. This implies that the transformation,

$$\psi(x) \to U(x)\psi(x), U(x) \in SU(3), \tag{2.1}$$

should result in the same Lagrangian. Enforcing this requirement results in the appearance of the gluon fields, A^μ_a, one for each of the eight generators of the $SU(3)$ group (the Gell-Mann matrices, in the fundamental representation). Quarks are defined to be in the fundamental representation of $SU(3)$ ($\mathbf{3}$, with anti-quarks being in the $\overline{\mathbf{3}}$). In this context, the strong interaction charge, the *color* charge is defined. As the quarks are in the fundamental representation, they behave as 3-dimensional vectors in the color space — implying the existance of 3 basis elements, the *red*, *green* and *blue* color charges (along with the *anti-red*, *anti-green* and *anti-blue* charges).

The process of gauge fixing also introduces eight new anticommuting scalar fields, the unphysical *ghosts*, whose presence is needed for the consistency of the theory, but beyond the scope of this work [34].

Collecting all the symmetries, and requiring that the theory is renormalizable, leads to the Lagrangian of QCD, written as follows, with implicit flavor and color summations [35]:

$$\mathcal{L}_{QCD} = \overline{\psi}(i\not{D} - \mathbf{M})\psi - \frac{1}{4}F_a^{\mu\nu}F^a_{\mu\nu}. \tag{2.2}$$

The quark fields are written as $\psi_{\alpha,i,f}(x)$, with Dirac index α, color index i and flavour index f, while the gluon fields are written as A_a^μ, with Lorentz index μ and color index a. The quark masses were generalized to a *quark mass matrix*, $\mathbf{M} = \text{diag}(m_1, \cdots, m_{N_f})$; $D_\mu = \partial_\mu - igA_\mu$ is the covariant derivative, introduced with the $SU(3)$ local gauge symmetry and $\not{D} = \gamma_\mu D^\mu$, with γ_μ being the Dirac gamma matrices.

The dynamical aspects of the gluons are given by the color trace $F_a^{\mu\nu}F^a_{\mu\nu}$, with $F_a^{\mu\nu}$ being a Lorentz tensor that is function of the derivatives of A_a^μ in the following way:

$$F_{\mu\nu} = \sum_a F^a_{\mu\nu}\mathrm{t}_a = \frac{i}{g}\left[D_\mu, D_\nu\right] = \partial_\mu A_\nu - \partial_\nu A_\mu - ig\left[A_\mu, A_\nu\right], \tag{2.3}$$

where $A_\mu = \sum_a A^a_\mu \mathrm{t}_a$.

In the commutator of equation (2.3) lies the key to the defining features of QCD, as seen in section 1.1. In Abelian theories, such as QED (based on $U(1)$ gauge symmetry) the commutator is zero, and there is no photon-photon interaction. As $SU(3)$ is a non-Abelian group, the commutator is not zero and gluon-gluon interactions are present. It is believed that the ggg and $gggg$ interactions may help to understand color confinement [9].

The Lagrangian (2.2) defines tree-level propagators and three interaction vertices, as seen in figure 2.1. Doing loop diagrams with the tree-level objects results in ultraviolet (UV) divergences, that are removed by the process of *renormalization* which redefines the Lagrangian and its components by including self-energy quantum corrections that cancel the UV divergences.

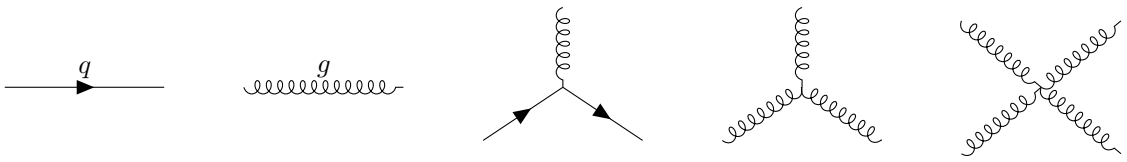

Figure 2.1: Five Feynman diagrams that represent the tree-level elements present in the QCD Lagrangian. From left to right: the quark propagator, the gluon propagator, the quark-gluon vertex, the three-gluon vertex and the four-gluon vertex.

2.2 QCD Spectrum and Bound States

The central objects of interest in a QFT are the *matrix elements* of operators, that is, objects of the form $\langle a|\mathcal{O}|b\rangle$. More specifically, when $\mathcal{O}$ is a time-ordered product of field operators acting on $|0\rangle$, the matrix element is called a *correlation function*:

$$G(x_1, x_2, \cdots, x_N) = \langle 0|\,\mathrm{T}\phi(x_1)\phi(x_2)\cdots\phi(x_N)\,|0\rangle\,, \tag{2.4}$$

where T represents the time-ordered product.

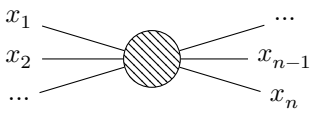

Figure 2.2: Schematic image of a correlation function.

The study of correlation functions is paramount in a QFT as they are related to experimental observables and many important theoretical quantities. Knowing all correlation functions of the system would give the total knowledge of its dynamics.

The discussion about correlation functions requires the knowledge of the physical states predicted by the theory, so the focus now turn to the state spectrum (the available states predicted by the theory) of QCD.

The discussion of confinement in section 1.1 indicates that this question is not as simple as it appears. States composed of single quarks (and colored combinations of several quarks) as well as gluon states have never been observed in experiments. The only experimentally accessible states are bound states — the hadrons. This means that the only correlation functions that are *well defined* in the experimental sense are of the following form, with h being some generic hadron:

$$\langle 0|\cdots|0\rangle\,, \quad \langle 0|\cdots|h\rangle\,, \quad \langle h|\cdots|h\rangle\,, \quad \langle hh|\cdots|h\rangle \quad \cdots \tag{2.5}$$

It follows that studying the state spectrum of QCD is studying its bound state spectrum.

To obtain the bound states of QCD it is mandatory to look at the representation theory of $SU(3)$. Hadrons must have at least a quark and anti-quark pair so that the end product is colorless — or in group theory terms, transform as the singlet representation $\mathbf{1}$. The possible combinations include (an extensive list can be found in [19]):

- *Mesons*, made of a quark-antiquark pair, $q\bar{q}$, as $\mathbf{3}\otimes\bar{\mathbf{3}} = \mathbf{1}\oplus\mathbf{8}$. These include, for example, the pions π, the kaons K and the J/ψ.
- *Baryons*, made of three quarks, qqq, as $\mathbf{3}\otimes\mathbf{3}\otimes\mathbf{3} = \mathbf{1}\oplus\mathbf{8}\oplus\mathbf{8}\oplus\mathbf{10}$. These include, for example, the proton and the neutron.
- *Tetraquarks*, made of two quarks and two anti-quarks $qq\bar{q}\bar{q}$. These can be seen as combination of two mesons: $(\mathbf{3}\otimes\bar{\mathbf{3}})\otimes(\mathbf{3}\otimes\bar{\mathbf{3}}) = (\mathbf{1}\oplus\mathbf{8})\otimes(\mathbf{1}\oplus\mathbf{8}) = \mathbf{1}\oplus\cdots$. These states have only been recently observed at LHC [36–39].
- *Pentaquarks*, made of four quarks and one anti-quarks $qqqq\bar{q}$, which again can be seen as combining a baryon and a meson. These have also been recently observed in LHC [40].
- Repeating the same process for a higher number of quarks should also reveal color singlet states that represent possible hadrons. It is expected, for example, that the atomic nuclei are also included.
- *Glueballs*, made of two gluons gg, as the product of two adjoint $\mathbf{8}$ representations should also contain a singlet state. Just as their quark counterparts, more gluons can be added, as long as a singlet state is available. Glueballs have not yet been identified in experiments.

Having now explored the possible bound states in the theory, the next step is to understand how they appear in the actual calculations — the answer lies in the correlation functions. When, in the physical process behind a correlation function, an exchange of momentum p is such that $p^2 = m_\lambda^2$, where λ is a bound state (specified by the fields involved), then the correlation function will show a pole, whose

residues are the transition matrix elements between the vacuum and the produced hadron. These residues are the *Bethe-Salpeter wave functions* (BSWFs) [41].

In more detail, let G be a generic correlation function with fields $\phi(x)$ [17],

$$G(x_1, \cdots, x_N, y_1, \cdots, y_M) = \langle 0| \, \mathrm{T}\phi(x_1) \cdots \phi(x_N)\phi(y_1) \cdots \phi(y_M) \, |0\rangle \, . \tag{2.6}$$

The completeness relation can be written as follows, where $|\lambda\rangle$ is an element of the QCD state space,

$$\mathbb{1} = \sum_{\lambda} \frac{1}{(2\pi)^3} \int \frac{d^3p}{2E_p} \, |\lambda\rangle \, \langle\lambda| \tag{2.7}$$

Inserting the completeness relation in the middle of (2.6) and focusing only on the portion of the time-ordered product where $x_i^0 > y_j^0$ leads to:

$$G = \sum_{\lambda} \frac{1}{(2\pi)^3} \int \frac{d^3k}{2E_k} \Theta \, \langle 0| \, \mathrm{T}\{\phi(x_1) \cdots \phi(x_N)\} \, |\lambda(k)\rangle \, \langle\lambda(k)| \, \mathrm{T}\{\phi(y_1) \cdots \phi(y_M)\} \, |0\rangle + \text{other terms}, \tag{2.8}$$

where $\Theta = \theta(\min(x_1^0, \dots, x_N^0) - \max(y_1^0, \dots, y_N^0))$ implements the $x_i^0 > y_j^0$ condition, and the other terms refers to the remainder of the original time-ordered products. It is also possible to place the completeness relation between any other pair of fields, paying special attention not to end up with single-quark states, thus correlation functions can contain a large number of bound states of different kinds.

The coordinates x_i and y_i can be re-expressed by introducing two *total* coordinates X and Y such that $x_i = X + x_i'$ and $y_i = Y + y_i'$. Translation invariance dictates that the total coordinate only adds a phase to the correlation function $\langle 0| \cdots |\lambda\rangle$. Defining, in a very suggestive way

$$\Psi(\{x_i\}, k) = \langle 0| \, \mathrm{T}\{\phi(x_1) \cdots \phi(x_N)\} \, |\lambda(k)\rangle \, , \tag{2.9}$$

and applying translation invariance, G can be written as:

$$G = \sum_{\lambda} \frac{1}{(2\pi)^3} \int \frac{d^3k}{2E_k} \Psi(\{x_i\}, k)\Psi^\dagger(\{y_j\}, k) e^{ik\cdot z} \theta(z^0 - \Delta) + \text{other terms}, \tag{2.10}$$

where $z = X - Y$, and $\Delta = \min({x'}_1^0, \dots, {x'}_N^0) - \max({y'}_1^0, \dots, {y'}_N^0)$. The step function can be represented as an integral: $\theta(x) = \int_{-\infty}^{\infty} d\omega \frac{i}{\omega + i\epsilon} e^{-i\omega x}$. Doing this substitution in G results in:

$$G = \sum_{\lambda} \frac{1}{(2\pi)^3} \int \frac{d^3k}{2E_k} \Psi(\{x_i\}, k)\Psi^\dagger(\{y_j\}, k) e^{ik\cdot z} \int_{-\infty}^{\infty} d\omega \frac{i}{\omega + i\epsilon} e^{-i\omega(z^0 + \Delta)} + \text{other terms}. \tag{2.11}$$

The next step is writing the Fourier transform of G in the variable z:

$$\begin{aligned} &\mathrm{FT}\,[G]\,(p) = G(p) = \\ &= \sum_{\lambda} \int_{-\infty}^{\infty} d\omega \frac{i}{\omega + i\epsilon} e^{-i\omega\Delta} \int \frac{d^3k}{2E_k} \Psi(\{x_i\}, k)\Psi^\dagger(\{y_j\}, k) \int d^4z e^{iz\cdot p} e^{i\omega z^0} e^{-iz\cdot k} + \text{other terms}. \end{aligned} \tag{2.12}$$

The last integration in z gives two δ-functions, such that:

$$\begin{aligned} &G(p) = \\ &= \sum_{\lambda} \int_{-\infty}^{\infty} d\omega \frac{i}{\omega + i\epsilon} e^{-i\omega\Delta} \int \frac{d^3k}{2E_k} \Psi(\{x_i\}, k)\Psi^\dagger(\{y_j\}, k) \delta^3\left(\vec{p} - \vec{k}\right) \delta\left(p^0 - E_\lambda - \omega\right) + \text{other terms}, \end{aligned} \tag{2.13}$$

and the remaining integrations take care of the newly created δ-functions, leaving G as a summation in

λ only:

$$G(p) = \sum_{\lambda} \frac{\Psi(\{x_i\}, p)\Psi^{\dagger}(\{y_j\}, p)}{2E_{\lambda}} \frac{ie^{-i(p^0 - E_{\lambda})\Delta}}{p^0 - E_{\lambda} + i\epsilon} + \text{other terms.} \tag{2.14}$$

Setting the Ψ aside for a moment, the remainder can be written in a more clear way when $p^2 \to m_{\lambda}^2$:

$$\frac{i}{2E_{\lambda}} \frac{ie^{-i(p^0 - E_{\lambda})\Delta}}{p^0 - E_{\lambda} + i\epsilon} = \frac{i\left(p^0 + E_{\lambda}\right)}{2E_{\lambda}} \frac{ie^{-i(p^0 - E_{\lambda})\Delta}}{p^0 - E_{\lambda} + i\epsilon} \to \frac{i}{p_0^2 - m_{\lambda}^2 + i\epsilon}, \tag{2.15}$$

which, when applied to G, reveals its pole spectrum. G is, in essence, a sum of terms that, when $p^2 \to m_{\lambda}^2$ will show a pole whose residues are the $\Psi(\{x_i\}, p)\Psi^{\dagger}(\{y_i\}, p)$:

$$G(p^2 \to m_{\lambda}^2) = \frac{i\Psi(\{x_i\}, p)\Psi^{\dagger}(\{y_i\}, p)}{p^2 - m_{\lambda}^2 + i\epsilon} + \text{finite terms.} \tag{2.16}$$

The Bethe-Salpeter wavefunction can now be identified as the residues of those poles: $\Psi(\{x_i\}, p)$. This idea is presented in a more schematical way in figure 2.2.

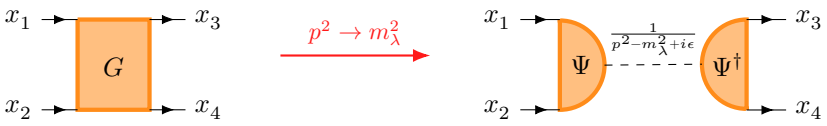

Figure 2.3: Schematic view of the creation of poles and the appearance of BSWF from correlation functions, in the limit $p^2 \to m_{\lambda}^2$.

These functions describe the hadron, in a similar way to the wavefunction in non-relativistic QM, but without the probabilistic interpretation as these objects transform under finite-dimensional non-unitary representations of the Poincaré group.

2.3 Form Factors and Parton Distribution Functions

Following the arguments so far, it is clear that the experimental study of QCD is intertwined with the experimental study of hadrons. The usual experiments consist of the scattering of hadrons with several types of other particles. From these events, it is possible to extract, for example, the hadronic *form factors*. These functions encode how hadrons interact with various types of currents, such as vector, axial, scalar, and pseudo-scalar currents.

One of the most relevant scattering experiments is the scattering of an electron with a nucleon (proton or neutron), namely $e^- N$ scattering. The physical interaction proceeds via the exchange of virtual photons — as QED has a very small coupling constant, $\alpha_{QED} \approx \frac{1}{137}$, it is dominated by a single photon exchange, as shown on the left side of figure 2.4.

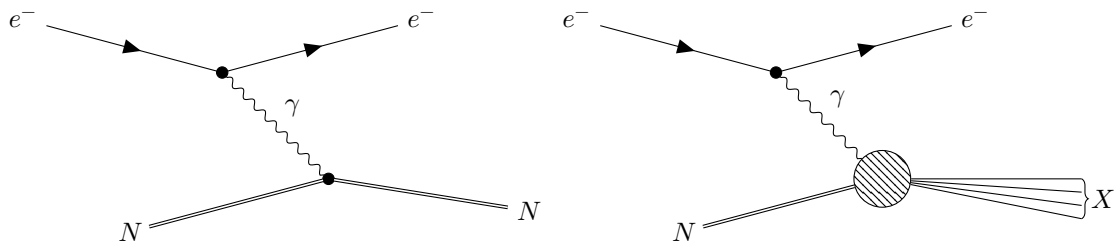

Figure 2.4: Left: Schematic view of a $e^- N$ scattering event. Right: Schematic view of a deep inelastic scattering event. The high energy of the virtual photon allows for the probing of the inside of the hadron

$e^- N$ scattering events give information on how hadrons couple to vector currents. The resulting form factors are the electromagnetic form factors, which give information on electric charge and magnetization distributions inside the hadron. These form factors were the first indications that the proton and neutron are not point-like particles — this discovery by Robert Hofstadter earned him the 1961 Nobel prize in physics [42].

Theoretically, form factors are contained in the general matrix elements

$$\langle p_1', p_2', ...| \, j^\Gamma(x) \, |p_1, p_2, ...\rangle \,, \tag{2.17}$$

where $\langle p_1', p_2', ...|$ are the outgoing particles, $|p_1, p_2, ...\rangle$ are the incoming particles, and $j^\Gamma(x)$ is an off-mass shell Dirac-flavour current that interacts with the incoming particles.

After removing the spinors, polarization vectors and so on for higher spin particles, the remainder can be written as

$$\mathcal{M}^{\mu\nu...}_{\alpha\beta...} = \sum_i F_i(p_j^2, {p'}_k^2, ...)\tau_i(p_1, p_2, ..., p_1', p_2', ...)^{\mu\nu...}_{\alpha\beta...}. \tag{2.18}$$

Equation (2.18) is an expansion of $\mathcal{M}$ in an appropriate tensor basis, with momentum-depedent tensors τ_i that give the correct tensorial stucture to $\mathcal{M}$. The coefficients of the expansion are the form factors F_i which only depend on Lorentz-invariant momentum terms like p^2 and $p_i \cdot p_j$.

The theoretical calculation of these quantities starts with the observation that *decay constants* can be calculated from the Bethe-Salpeter WF by contraction with a Dirac-flavor matrix $\Gamma \mathrm{t}_a$, where Γ can be, for example, $\mathbb{1}, i\gamma_5, \gamma^\mu, \gamma_5\gamma^\mu$ for scalar, pseudoscalar, vector, axial-vector currents respectively:

$$\langle 0| \, j^\Gamma \, |\lambda(p)\rangle = \Gamma^{\alpha\beta}(\mathrm{t}_a)_{ij} \, \langle 0| \, \psi_{i\alpha}(x)\overline{\psi_{j\beta}}(x) \, |\lambda(p)\rangle \,. \tag{2.19}$$

Doing the same process for a hadron-hadron matrix element, it is possible to obtain the desired matrix elements:

$$\langle \lambda'(p_f)| \, j^\Gamma \, |\lambda(p_i)\rangle = \Gamma^{\alpha\beta}(\mathrm{t}_a)_{ij} \, \langle \lambda'(p_f)| \, \psi_{i\alpha}(x)\overline{\psi_{j\beta}}(x) \, |\lambda(p_i)\rangle \,. \tag{2.20}$$

The current j^Γ interacts with the hadron by coupling to quarks inside the bound-state, as in figure 2.5.

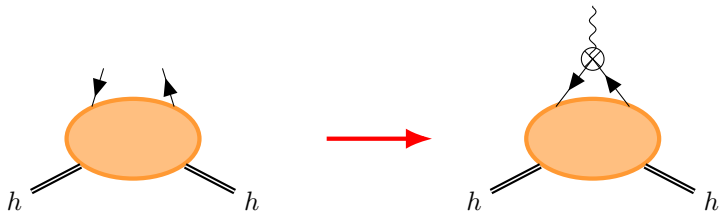

Figure 2.5: Schematic view of the contraction of a Dirac matrix with the hadron h four-point function to obtain the hadron matrix elements.

Going back to the $e^- N$ scattering case, for very high-energy reactions, the virtual photon can carry enough energy to break the hadron apart, creating reactions like $eN \to eX$, where X represents the resulting particles from the hadron. This process is known as *Deep Inelastic Scattering* (DIS), represented on the right side of figure 2.4. As the photon is now energetic enough to probe the inside of the hadron, these experiments give access to the partonic structure of the hadron, that is, its contents and its parton distribution functions.

Let X be defined as the end state of a deep-inelastic scattering experiment (which may include more than one particle) and M' be the sum of the invariant masses of the end state. In the case that $M' \leq M$, where M is the mass of the nucleon, one defines the *Bjorken variable* $x \in (0, 1]$ which determines how inelastic the reaction is. The case $M = M'$ corresponds to $x = 1$, that is, elastic $e^- N$ scattering, and

$x \to 0$ corresponds to increasingly inelastic events.

The limit where $\nu = \frac{p_i \cdot q}{M} \to \infty$ for constant x, where p_i is the incoming hadronic momentum and q is the transferred momentum, is called the *Bjorken limit* [43]. In this limit, the form factors do not depend on the transferred momentum, but only on the Bjorken variable x. This behavior is named *Bjorken scaling* and it led to the development of the *parton* model, where the hadrons are seen as collections of on-shell quarks and gluons.

Going to the infinite-momentum frame, one assumes that the momentum of each parton is collinear with the total momentum (as the transverse part will be very small in comparison), and each has a specific fraction of the longitudinal momentum ξ_i. The value of the Bjorken x is then associated with to the longitudinal momentum fraction of the parton. A photon only couples to partons that have a momentum fraction of $\xi_i = x$. That way, the momentum distribution of the particles inside the hadron can be probed.

In this context, the concept of parton distribution functions (PDFs) appears naturally as the momentum distributions $f_k(\xi)$, such that $f_k(\xi)d\xi$ is the probability density that a parton of species k carries a momentum fraction between ξ and $\xi + d\xi$ [17].

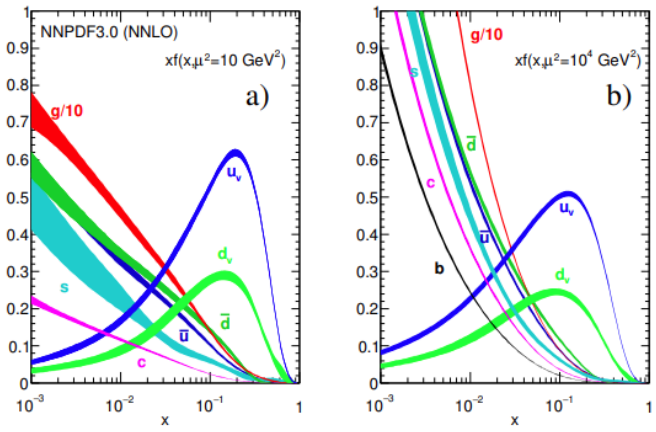

Figure 2.6: The proton's parton distribution functions, measured at different energy scales. (Adapted from [19].)

A comparison of the left and right panels in figure 2.6 makes clear that the Bjorken scaling observation is not perfect as the PDFs change with the energy scale. The resolution of the photon probe will depend on the coupling constant, introducing a scale factor. The main implication is that the hadron will look different to an incoming photon depending on the energy. Low energy photons see the hadron as a point charge. Increasing the energy will reveal the valence partons. These partons determine the external properties of the hadron. Higher-energy photons will be able to distinguish the sea partons, as well as the valence partons. The DGLAP (Dokshitzer, Gribov, Lipatov, Altarelli, Parisi) equations allow the connection of the PDFs at different energy scales [44–46].

One way to calculate PDFs from non-perturbative methods is through overlaps of LFWFs [29]. The calculation of the LFWFs is the main subject of this work.

LFWFs are calculated by projecting the BSWF (more details in section 2.5) onto the light-front. The first step is, therefore, the calculation of BSWF, which is presented in the next section (2.4).

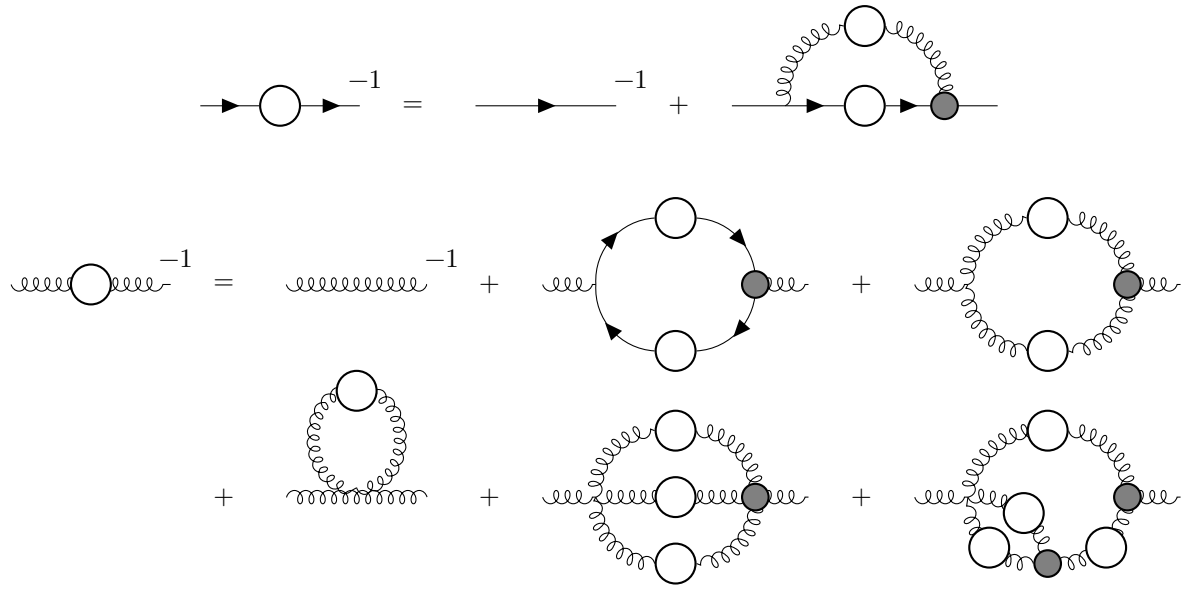

Figure 2.7: Above: the quark DSE. Below: the gluon DSE. In the gluon DSE the ghost fields contributions were omitted and the prefactors from the symmetrization were suppressed.

2.4 Dyson-Schwinger Equations and Bethe-Salpeter Equation

In addition to perturbation theory, there are other ways to calculate the correlation functions G of a QFT.

Dyson and Schwinger derived an infinite system of coupled integral equations that relate the correlation functions of a theory to each other [47, 48]. These are the *Dyson-Schwinger equations* (DSEs). They are the quantum equations of motion that allow for the determination of the full correlation functions including the quantum corrections — also known as *dressed* correlation functions. The solution of such equations constitutes what in the literature is called the *Functional Methods*.

The functional methods are one of the main methods of non-perturbative analysis of QCD, alongside Lattice QCD, where the fields are simulated and evolved in a discretized four-dimensional space-time; and effective field theories, which attempts to use hadrons as fundamental degrees of freedom and build a phenomenologic Lagrangian that mimics the desired QCD behavior.

In practical calculations, however, it is impossible to solve infinitely many coupled integral equations, so there is the need to truncate the system at some point in order to generate a finite closed set of equations. Usually, relations such as the *Ward-Takahashi identities* (in the Abelian case) and the *Slavnov-Taylor identities* (in the non-Abelian case), which arise from gauge symmetry and add extra relations between the n-point functions, can help to close the system. In addition, some ansätze (guided by information obtained by other means, for example, Lattice QCD) are also used to model the truncated parts of the system. The truncation must done in such a way that the resulting truncated system can replicate the desired properties of QCD [49].

It is possible to adapt the schematic notation used in Feynman diagrams to the DSEs and, by using a hollow white circle to denote dressed propagators and a filled circle to denote dressed vertices, one can write some QCD DSEs, in pictorial form, in figure 2.7 [17, 49]. There is an ordering in these functions, which is seen, for example, in the quark DSE which depends on the qqg vertex DSE and the gluon DSE. The gluon DSE, on the other hand, depends on the quark DSE, on the qqg vertex DSE, the ggg vertex DSE and the $gggg$ vertex DSE (and the ghost loop, which is not shown in 2.7).

In general, the DSEs create a tower of infinitely many coupled equations, starting with the 2-point function. The DSEs are exact, and as such, they contain in themselves the perturbation theory ex-

pansions. For example, if the dressed propagator is Δ, the *classical* (tree-level, as it appears in the Lagrangian) propagator is Δ_0 and the sum of self-energy contributions is Σ, the DSE for Δ is:

$$\Delta = \Delta_0 + \Delta_0 \Sigma \Delta. \tag{2.21}$$

Σ is the term that contains the dependence on the other n-point functions. The DSEs in figure 2.7 are exactly of this form, but with the Σ term expanded in its individual contributions. Iterating the solution for Δ back in the DSE generates a series of terms

$$\Delta = \Delta_0 + \Delta_0 \Sigma \Delta = \Delta_0 + \Delta_0 \Sigma \Delta_0 + \Delta_0 \Sigma \Delta_0 \Sigma \Delta = ... \tag{2.22}$$

where higher order terms can be ignored if the coupling constant is $|g| < 1$, generating the perturbative expansion. However, equation (2.22) always results in the exact solution due to the last Δ, no matter what the value of the coupling constant g, in the same way that

$$f(x) = 1 + xf(x) = 1 + x + x^2 f(x) = 1 + x + x^2 + x^3 f(x) \, ... \tag{2.23}$$

always resolves to $f(x) = \frac{1}{1-x}$ even though the series expansion $f(x) = \sum_n x^n$ only converges to $\frac{1}{1-x}$ for $|x| < 1$.

The DSEs also play a fundamental role when doing bound-state calculations. Defining G to be, for simplicity, a quark four-point correlation function (which, as discussed in section 2.2, contains the meson spectrum), T to be the scattering matrix (dictating the interaction between the quarks) and G_0 to be the product of quark and anti-quark dressed propagators, one can write [13]

$$G = G_0 + G_0 T G_0. \tag{2.24}$$

In simple terms, G is *made* of two possible situations: a quark and anti-quark *pass* one another, without interacting (the G_0 term); or a quark and anti-quark *meet*, interact and propagate further (the $G_0 T G_0$ term). The four-point function G is the solution of a scattering equation of the form of equation (2.21) [13]:

$$G = G_0 + G_0 K G \quad \Leftrightarrow \quad T = K + K G_0 T \tag{2.25}$$

K is defined as the interaction kernel, that is, the collection of all diagrams that are two-particle irreducible with respect to the quark propagators. This includes all diagrams except those that can be cut into two pieces by cutting a quark and anti-quark line since these will be generated by iteration from the irreducible ones.

In the spirit of equation (2.22), one can analyse the equation for G and T. By iteration, one has:

$$G = G_0 + G_0 K G = G_0 + G_0 K G_0 + G_0 K G_0 K G = ... \, , \tag{2.26}$$

$$T = K + K G_0 T = K + K G_0 K + K G_0 K G_0 T = ... \, . \tag{2.27}$$

G (and T as well) can therefore be viewed as an infinite sum of terms grouped by the number of interactions between the quark and anti-quark lines. The sum starts with no interactions, followed by a term where the particles interact once, then by a term where particles interact twice, then three times, and so on up to infinity. Again, just like equation (2.23), equations (2.26) and (2.27) are always exact due to the last term (G and T respectively).

The connection with bound states enters through the discussion of section 2.2 about how hadrons create poles in the correlation functions of the theory. Thus, when $p^2 \to m_\lambda^2$, where λ is a meson, G is

expected to be of the form of equation (2.16):

$$G \to \frac{\Psi\bar{\Psi}}{p^2 - m_\lambda^2 + i\epsilon} \quad \Leftrightarrow \quad T \to \frac{\psi\bar{\psi}}{p^2 - m_\lambda^2 + i\epsilon}. \tag{2.28}$$

From equation (2.24) it is possible to see that $\Psi = G_0\psi$. ψ is the *Bethe-Salpeter amplitude*, or in short form as it will be used from now one, the *amplitude*. Replacing equation (2.28) into the DSEs of equation (2.25), one obtains:

$$G = G_0 + G_0KG \quad \Leftrightarrow \quad \frac{\Psi\bar{\Psi}}{p^2 - m_\lambda^2 + i\epsilon} = G_0 + G_0K\frac{\Psi\bar{\Psi}}{p^2 - m_\lambda^2 + i\epsilon} \tag{2.29}$$

Comparing the residues on both sides gives:

$$\Psi = G_0K\Psi \quad \Leftrightarrow \quad \psi = KG_0\psi, \tag{2.30}$$

which are, respectively, the *Bethe-Salpeter Equation* (BSE) for the wavefunction and the amplitude [13]. Similar to how the correlation function displays hadronic poles, the Dyson-Schwinger equation gives rise to the Bethe-Salpeter equation when $p^2 \to m_\lambda^2$. In graphical form:

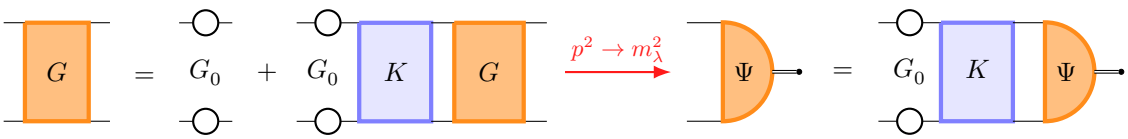

Figure 2.8: On the left, the DSE for G is shown. When $p^2 \to m_\lambda^2$, the DSE gives rise to the BSE, shown on the right.

Equation (2.30) has a very similar form to an eigenvalue equation (it amounts to calculating the eigenvector ψ such that the eigenvalue of KG_0 is 1). To this end, one introduces an artificial eigenvalue $\lambda(p^2)$ in the equation:

$$\lambda(p^2)\psi = KG_0\psi. \tag{2.31}$$

The mass of the bound state is then determined by the value of p^2 such that $\lambda(p^2) = 1$. If, on the other hand, the eigenvalue spectrum of KG_0 is collected as $\lambda_i(p^2)$, then it is also possible to determine the excited states, in the same way as the ground state, by finding $p^2 = m_i^2$ such that $\lambda_i(p^2 = m_i^2) = 1$.

2.5 Light-Front Dynamics and Light-Front Wave Functions

There are several forms of relativistic dynamics. Usually, when working with scattering events and cross-sections, it is beneficial to define the needed commutation relations at a time $t = 0$ — known as the canonical quantization. Quantities are defined at $t = 0$, evolved in space-time according to the dynamics of the system, and measured at a later time t.

There are, however, other ways to quantize the theory. Dirac proposed three different forms of dynamics: equal-time (the canonical), as described above; light-front and point form [27]. All these methods are equivalent and transform into each other via unitary transformations.

Light-front dynamics are defined by an initial hypersurface given by

$$x^0 + x^3 = 0, \tag{2.32}$$

using a Minkowski four-vector $x^\mu = (x^0, x^1, x^2, x^3)$, with the usual metric $g^{\mu\nu} = \text{diag}(+, -, -, -)$. Based

on equation (2.32), the light-front coordinates x^+ and x^- are defined as:

$$x^+ = x^0 + x^3 \qquad\qquad x^- = x^0 - x^3. \tag{2.33}$$

Equation (2.32) can then be written simply as $x^+ = 0$. The remaining two dimensions are transversal to the initial surface in equation (2.32), and as such, are included in a two-dimensional vector $\vec{x}_\perp = \{x^1, x^2\}$. x^μ can be written as:

$$x^\mu = \{\vec{x}_\perp, x^+, x^-\}, \tag{2.34}$$

and the curly brackets $\{\}$ will denote the light-front components of a four-vector from now on. Inner products in light-front components are then

$$x \cdot y = x^0 y^0 - x^1 y^1 - x^2 y^2 - x^3 y^3 = \frac{1}{2}\left(x^- y^+ + y^- x^+\right) - \vec{x}_\perp \cdot \vec{y}_\perp. \tag{2.35}$$

From equation (2.33) the four-momentum integration measure in light-front components follows as:

$$\int d^4p = \frac{1}{2}\int d^2p_\perp \int dp^+ \int dp^-. \tag{2.36}$$

Light-front dynamics has some advantages compared to equal-time dynamics for calculating the properties of hadrons. Firstly, as mentioned in the end of section 2.3, the light-front is the natural frame to define PDFs, as these are simply the overlap of light-front wave functions. Secondly, Bjorken scaling indicates that, on the light front, hadrons are made of point-like partons with a certain fraction ξ_i of the total longitudinal momentum p_i of the hadron.

Arguably, the most important property of light-front dynamics is the simpler vacuum. In light-front dynamics, it is possible to prove that for a longitudinal momentum $p^+ \geq 0$, it follows automatically that $p^- \geq 0$. This implies that the vacuum, defined as the zero-momentum state, only contains particles that have $p^+ = 0$. On the other hand, in equal-time dynamics, it is possible to have zero total momentum states with an arbitrary number of particles, so the vacuum $|0\rangle$ is the overlap of an infinite number of Fock states with definite particle number [31]. In practice, this fact allows writing the hadronic states as a sum of an infinite number of Fock states with a definite particle number, whose coefficients are the light-front wave functions $\Psi^{(n)}_{LF}(\{\xi_i, \vec{k}_{i\perp}\})$ [31].

The light-front wave functions are the probability distributions of the hadron being in a state with N constituents, each with a fraction ξ_i of the longitudinal momentum, and intrinsic transverse momentum $\vec{k}_{i\perp}$. Note that there is a light-front wave function for each number N of particles. The wavefunction with the minimal number of particles (for example, $N = 2$ for mesons, $N = 3$ for baryons and so on), are known as the light-front *valence* wave functions. They provide the leading order term in the expansion.

Focusing on the two-particle valence wave function, the objective of this work is to derive them from the BSWF through a suitable projection. The first step is to define a light-like vector n such that $n^2 = 0$ and $n^- = 2$. Taking a generic four-vector x and doing the inner product with n will result in the x^+ component.

The Bethe-Salpeter wave function on the light front can be written as function of a spatial coordinate $x = \lambda n + \vec{x}_\perp$, where λ is a scalar, $\vec{x}_\perp$ is a transverse component, $x^+ = 0$, and P is the total momentum:

$$\Psi(\lambda n + \vec{x}_\perp, P) = \int \frac{d^4q}{(2\pi)^4} e^{-iq\cdot(\lambda n + \vec{x}_\perp)} \Psi(q, P). \tag{2.37}$$

Equation (2.37) is just the inverse Fourier transform from momentum space to coordinate space, at $x = \lambda n + \vec{x}_\perp$.

The light-front (valence) wave function is defined as the Fourier transform of equation (2.37) with

respect to x^- and $\vec{x}_\perp$, up to a prefactor C, to be determined later:

$$\Psi_{LF}(k^+, \vec{k}_\perp) = C \int \frac{d\lambda}{2\pi} \int \frac{d^2x_\perp}{(2\pi)^2} e^{i\lambda k^+} e^{i\vec{k}_\perp \cdot \vec{x}_\perp} \Psi(\lambda n + x_\perp, P). \tag{2.38}$$

Note that $k \cdot n = k^+$. Replacing $\Psi(\lambda n + \vec{x}_\perp, P)$ from the definition of equation (2.37) results in

$$\Psi_{LF}(k^+, \vec{k}_\perp) = C \int \frac{d^4q}{(2\pi)^4} \Psi(q, P) \int \frac{d^2x_\perp}{(2\pi)^2} e^{i(\vec{k}_\perp - \vec{q}_\perp)\cdot \vec{x}_\perp} \int \frac{d\lambda}{2\pi} e^{i\lambda(k^+ - q^+)}. \tag{2.39}$$

The last two integrations, in $\vec{x}_\perp$ and λ, result each in a Dirac-δ function that matches the external and the internal variables:

$$\Psi_{LF}(k^+, \vec{k}_\perp) = C \int \frac{d^4q}{(2\pi)^4} \Psi(q, P) \delta^2\left(\vec{k}_\perp - \vec{q}_\perp\right) \delta(k^+ - q^+). \tag{2.40}$$

Taking the integration measure as in equation (2.36) results in the very straightfoward definition of the light-front wave function as the integration of the Bethe-Salpeter wave function in q^-, at $q^+ = k^+$ and $\vec{q}_\perp = \vec{k}_\perp$:

$$\Psi_{LF}(\alpha, \vec{k}_\perp) = \frac{C}{2(2\pi)^4} \int dq^- \Psi\left(q^-, q^+ = \frac{\alpha}{2}P^+, \vec{q}_\perp = \vec{k}_\perp, P\right), \tag{2.41}$$

where k^+ is written as a fraction $\frac{\alpha}{2}$ of the $+$ component of the total momentum P.

A *parton distribution amplitude* (PDA) is defined by integration over $k_\perp$ of the light-front wave function:

$$\phi(\alpha) = \int d^2k_\perp \Psi_{LF}(\alpha, \vec{k}_\perp). \tag{2.42}$$

The same result can be obtained by taking the Fourier transform of equation (2.37) in x^- only, and with $x = \lambda n$ ($\vec{x}_\perp = \vec{0}$). The practical use of the equations (2.41) and (2.42), alongside the Bethe-Salpeter equation in equation (2.30) will be discussed in chapter 3.

2.5.1 Other hadronic properties

Similar to the definition of the light-front wave function and the parton distribution amplitude, other hadronic properties are defined, by doing the same transformation done to the Bethe-Salpeter wave function, but with different correlation functions [29], as shown in figure 1.1.

Starting with a correlator like (with $\mathcal{O}$ an operator)

$$\mathcal{G}(x, P) = \langle P | \, \mathrm{T}\overline{\psi}(x)\mathcal{O}\psi(0) \, | P \rangle \,, \tag{2.43}$$

one defines the analog of the PDA, the parton distribution function (as in section 2.3):

$$\mathrm{PDF}(\alpha) \propto \int \frac{d\lambda}{2\pi} e^{i\lambda\frac{\alpha}{2}P^+} \mathcal{G}(\lambda n, P), \tag{2.44}$$

and the analog of the LFWF, the *transverse momentum distribution* (TMD) as

$$\mathrm{TMD}(\alpha, \vec{k}_\perp) \propto \int \frac{d\lambda}{2\pi} \int \frac{d^2x_\perp}{(2\pi)^2} e^{i\lambda\frac{\alpha}{2}P^+} e^{i\vec{k}_\perp \cdot \vec{x}_\perp} \mathcal{G}(\lambda n + \vec{x}_\perp, P). \tag{2.45}$$

.

Similarly, with a correlator like

$$\mathcal{G}(x, \Delta, P) = \langle P_f | \, \mathrm{T}\overline{\psi}(x)\mathcal{O}\psi(0) \, | P_i \rangle \,, \tag{2.46}$$

where $P = \frac{P_i + P_f}{2}$ and $\Delta = P_f - P_i$, the analog of the PDA is the *generalized parton distribution* (GPD):

$$\text{GPD}(\alpha, \Delta) \propto \int \frac{d\lambda}{2\pi} e^{i\lambda \frac{\alpha}{2} P^+} \mathcal{G}(\lambda n, \Delta, P), \tag{2.47}$$

and the analog of the LFWF is the *generalized transverse momentum distribution* (GTMD):

$$\text{GTMD}(\alpha, \vec{k}_\perp, \Delta) \propto \int \frac{d\lambda}{2\pi} \int \frac{d^2 x_\perp}{(2\pi)^2} e^{i\lambda \frac{\alpha}{2} P^+} e^{i\vec{k}_\perp \cdot \vec{x}_\perp} \mathcal{G}(\lambda n + \vec{x}_\perp, \Delta, P). \tag{2.48}$$

Integrating the PDA over α results in a probability; the PDF results in the hadronic charge and the GPD results in the hadron form factors.

Knowing how to calculate quantities such as the Bethe-Salpeter wave function, equations (2.43) and (2.46) and having a mature and well-established method of projecting to the light-front, a large number of hadronic properties and observables can be calculated, allowing for spatial and momentum tomography of hadrons.

Chapter 3

Calculating Light-Front Wave Functions

In the previous chapter, the theoretical tools for the calculation of bound states and their properties were presented. The next logical step is to analyze how those tools can be used in practice.

For example, solving the Bethe-Salpeter equation (2.30) presents some challenges, as the analytic structure of the kernel and the propagators imposes some restrictions on the numerically available domains. On the same note, equation (2.41) shows a formally simple integral that, however, requires some analytic continuation method as the BSE does not provide information on the whole domain needed to compute the LFWF. The present chapter describes one of the methods currently used to overcome these difficulties, based on the Nakanishi method. Afterwards, a new method will be proposed, which is the purpose of this work and the focus of this chapter.

As discussed in the introductory chapter, in section 1.3, a scalar toy model will be used instead of QCD. Some extensions of this scalar model that will help to close the gap with QCD will also be considered in chapter 5.

3.1 Euclidean conventions

From now on, a Euclidean metric will be used instead of the Minkowski one, which amount to changing a Euclidean metric $g_E^{\mu\nu} = \text{diag}(+,+,+,+)$. A four-vector $x = (x^0, x^1, x^2, x^3)$ is written as:

$$x = [x^1, x^2, x^3, x^4], \tag{3.1}$$

by defining $x^4 = ix^0$. From now on, square brackets [] will be used to denote vectors written in Euclidean coordinates, alongside the curly brackts for light-front coordinates (as in section 2.5). A generic four-vector p is written as:

$$p = \begin{bmatrix} \vec{p}_\perp \\ p^3 \\ ip^0 = p^4 \end{bmatrix} = \begin{Bmatrix} \vec{p}_\perp \\ p^+ \\ p^- \end{Bmatrix}. \tag{3.2}$$

Denoting Euclidian variables with a subcript E, scalar products acquire minus signs:

$$p \cdot q = p^0 q^0 - p^1 q^1 - p^2 q^2 - p^3 q^3 = -p^1 q^1 - p^2 q^2 - p^3 q^3 - p^4 q^4 = -p_E \cdot q_E. \tag{3.3}$$

The obvious corollary of equation (3.3) is that the norm of four-vectors also acquires a minus sign:

$$p^2 = (p^0)^2 - |\vec{p}|^2 = -|\vec{p}|^2 - (p^4)^2 = -(p_E)^2, \tag{3.4}$$

where $\vec{p} = (p^1, p^2, p^3)$ denotes the spatial part of the four-vector. A four-vector p_E is called spacelike if $p_E^2 > 0$ and timelike if $p_E^2 < 0$. In particular, on-mass shell particles have a momentum squared $p_E^2 = -m^2$.

The light-front definitions will be the same as in equation (2.33). In the Euclidean variables, and dropping the E subscript, the scalar product becomes:

$$x \cdot y = \vec{x}_\perp \cdot \vec{y}_\perp - \frac{1}{2}\left(x^- y^+ + y^- x^+\right), \tag{3.5}$$

which differs from equation (2.35) by a global minus sign. In the same way, the vector n of section 2.5 can be written in Euclidean variables as:

$$n = \begin{bmatrix} \vec{0} \\ -1 \\ i \end{bmatrix} = 2 \begin{Bmatrix} \vec{0} \\ 0 \\ 1 \end{Bmatrix}, \tag{3.6}$$

and $p \cdot n = -p^+$.

3.2 Scalar Model

The scalar toy model in consideration consists of two scalar particles, ϕ and χ, of mass m and μ respectively. The theory is defined by a simple Lagrangian, whose interacting part is

$$\mathcal{L}_{int} = g\phi\phi\chi. \tag{3.7}$$

Note that, for dimensional consistency, the coupling constant g has dimensions of mass 1. By defining the dimensionless coupling constant c and the mass ratio β, the mass m drops out from the calculations and its only the purpose is setting a scale:

$$c = \frac{g^2}{(4\pi m)^2}, \qquad \beta = \frac{\mu}{m}. \tag{3.8}$$

This scalar model has only three tree-level diagrams in the Lagrangian, whose Feynman rules are given in figure 3.1.

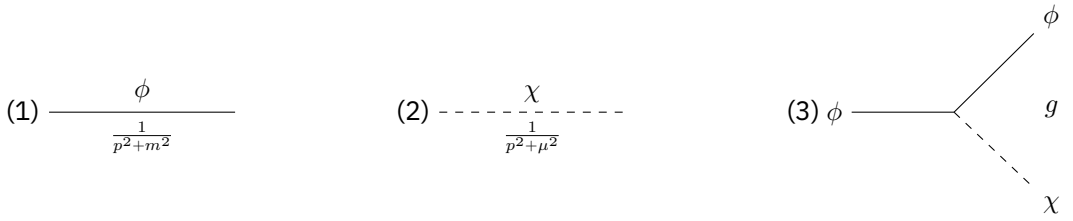

Figure 3.1: Feynman rules for the tree-level diagrams on the scalar model Lagrangian. From left to right: the ϕ propagator, the χ propagator and the $\phi\phi\chi$ vertex.

The process for calculating the bound states for this model starts by writing down its Bethe-Salpeter equation in (2.30). For that, two assumptions will be made.

The first one is related to G_0. In principle, G_0 is the product of the two (dressed) propagators $D_\chi(p^2)$ and $D_\phi(p^2)$, which should be obtained via their Dyson-Schwinger equations. In the following, (based on [33]), it is assumed that the dressing effects are relatively small, and that the tree-level propagators are a good enough approximation.

The second approximation is related to the structure of the interaction kernel K. In this work, a single ladder exchange is considered, which consists of two ϕ particles interacting via a single χ particle. In the limit where $\beta \to 0$, that is, $\mu \to 0$ (massless exchange particle), this model is known as the *Wick-Cutkosky* model, and is solvable analytically [50–52].

Making evident the loop integration in the Bethe-Salpeter equation and using the previous assumptions, the application of equation (2.30) to the scalar model yields an equation for the amplitude ψ:

$$\psi(q,P) = \int \frac{d^4q'}{(2\pi)^4} K(q,q') G_0(q',P) \psi(q',P), \tag{3.9}$$

where K and G_0 are, respectively:

$$K(q,q') = \frac{g^2}{(q-q')^2+\mu^2}, \tag{3.10}$$

$$G_0(q,P) = \frac{1}{q_1^2+m^2}\frac{1}{q_2^2+m^2}. \tag{3.11}$$

The kinematics are defined such that P is the total momentum, q is the external relative momentum, q' is the loop momentum, and q_1 and q_2 are the momenta of each particle. Writing these quantities as functions of three four-vectors n, k and P, where $k^+ = 0$ so that $k \cdot n = 0$, one obtains

$$q = k + (\xi - \eta)P, \tag{3.12}$$

$$q_1 = q + \eta P = k + \xi P, \tag{3.13}$$

$$q_2 = -q + (1-\eta)P = -k + (1-\xi)P, \tag{3.14}$$

where the parameter $\eta \in [0,1]$ is an arbitrary momentum partitioning parameter, and ξ is the light-front momentum fraction:

$$\xi = \frac{q_1 \cdot n}{P \cdot n} = \frac{q_1^+}{P^+} = 1 - \frac{q_2 \cdot n}{P \cdot n} = 1 - \frac{q_2^+}{P^+}. \tag{3.15}$$

Having defined the form and content of the Bethe-Salpeter equation for the scalar model, the focus will now be on the calculation of the valence LFWF. The Nakanishi representation is one of the methods used to calculate the LFWFs and will be presented in the next section.

3.3 Light-front wave functions from the Nakanishi representation

Looking at equation (3.9) and the definitions of the propagator and the kernel, equations (3.11) and (3.10), respectively, one can see that there are singularites that require special attention.

The problem of solving the Bethe-Salpeter equation is a numerically difficult one. Nakanishi proposed a method that leads to the definition of a spectral representation of any multi-leg transition amplitude built by an infinite series of Feynman diagrams [32, 53]. In this case, the main idea is to express the BSWF as the integration of a non-singular weight function, known as the *Nakanishi weight function* $g(x,z) = (1-z^2)h(x,z)$, multiplied with a denominator that contains the analytic structure. The desired quantities to be calculated are then expressed as functions of the weight function.

The light-front wave function can be derived from the weight function g by [32]:

$$\Psi_{LF}(x,z) = \frac{(1-z^2)^2}{4\sqrt{2}} \int_0^\infty dx' \frac{h(x',z)}{\left[x'+x+1+t(1-z^2)\right]^2}, \tag{3.16}$$

where $x = \frac{\mathbf{k}_\perp^2}{m^2}$, $z = 1 - 2\frac{k_1^+}{P^+}$ (equally for the primed variables x' and z') and $t = \frac{P^2}{4m^2} = \frac{-M^2}{4m^2}$, with P the total momentum.

When using the Nakanishi representation, the object of focus is shifted to the weight function g and everything else is derived from the g function. The main problem is finding the g function. One can derive an equation for the weight function from the BSE [31, 32]:

$$\int_0^\infty dx' \frac{h(x',z)}{\left[x'+\mathcal{N}(x,z)\right]^2} = \int_0^\infty dx' \int_{-1}^1 dz' V(x,z,x',z') \frac{1-z'^2}{1-z^2} h(x',z'), \tag{3.17}$$

where several functions were defined to make the expression more compact [31]:

$$\mathcal{N}(x,z) = x + 1 + t(1-z^2), \tag{3.18}$$

$$V(x,z,x',z') = \frac{c}{2} \frac{1}{\mathcal{N}(x,z)} \int_0^1 dv \left[K(v,z,z',x,x') + K(v,-z,-z',x,x')\right], \tag{3.19}$$

$$K(v,z,z',x,x') = \frac{\theta(z'-z)(1+z)^2 v^2}{\left[v(1-v)(1+z')\mathcal{N}(x,z) + v^2(1+z)\mathcal{N}(x',z') + (1-v)(1+z)(\beta+vx')\right]^2}. \tag{3.20}$$

Writing equation (3.17) in a more compact and symbolic way, denoting the integrations of g in the left and right hand side, respectively, as operators $\mathbf{B}$ and $\mathbf{K}$, the generalized eigenvalue problem structure of this equation becomes obvious:

$$\lambda \mathbf{B}\, h = \mathbf{K}\, h \Rightarrow \lambda h = \mathbf{B}^{-1}\, \mathbf{K}\, h, \tag{3.21}$$

where an artificial eigenvalue λ was introduced, in the same spirit as in the discussion of the eigenvalue spectrum of the BSE, at the end of section 2.4. Naturally, the solution of this equation is only valid if the operator $\mathbf{B}$ is invertible, that is, if $\mathbf{B}^{-1}$ exists and is well defined (more details in section 3.5). In practical numerical calculations it is necessary to add a small regularization parameter ϵ, to ensure good numerical inversion of the operator $\mathbf{B}$ [31, 32] .

The Nakanishi representation has been very successful in the study of the BSE, the LFWF and other structure functions. There have been many instances in the literature where the Nakanishi representation was instrumental, for example, in the calculation of pion and kaon light-front wave functions and structure functions like PDFs and GPDs. Some recent examples can be found in [54–56].

However, from equations (3.17) through (3.20), it is possible to understand one of the drawbacks of using the Nakanishi representation. It is necessary to know in full detail the structure of the integral, and in particular, it is necessary to derive the representation for each problem anew. Although this is manageable in the simpler cases, like the one in this study, the calculation can get very intricate and difficult to manage (as an example, see the calculation for the crossed-ladder kernel in [31]).

Additionally, the Nakanishi representation cannot access the resonance spectrum, that is, situations where $P^2 = -M^2 < -(m_1+m_2)^2$ [32].

3.4 Light-front wave functions from contour deformations

In an attempt to solve, or at least offer some improvement in relation to such drawbacks, a new method for solving the BSE and calculating the LFWF is presented.

The main idea of this method is to take equations (2.30), (2.41) and (2.42) exactly as they are, understand what restrictions are imposed by the analytic structure of the integration, work around them by deforming the integration path (hence *contour deformations*) in order to keep the desired definitions of the equations, and use analytical continuation methods to extrapolate information where needed.

The first step is to analyze the analytic structure of equation (2.30). For that purpose, one needs to specify the kinematics of the system.

3.4.1 Kinematics

In principle, the choice of kinematics is of no importance to the physical output of the calculations. It is, however, helpful to choose one set of kinematic variables such that the mathematical formulation is simpler. In this work, the rest frame of the hadron will be chosen as a reference frame. Therefore, the four-vectors P and k, from equations (3.12) to (3.14) can be written as:

$$k = m\sqrt{x}\begin{bmatrix} 0 \\ 0 \\ \sqrt{1-\omega^2} \\ \omega \end{bmatrix}, \quad P = 2m\sqrt{t}\begin{bmatrix} 0 \\ 0 \\ 0 \\ 1 \end{bmatrix}. \tag{3.22}$$

The three Lorentz-invariant quantities in the problem are:

$$x = \tfrac{k^2}{m^2}, \quad \omega = \hat{k}\cdot\hat{P}, \quad t = \tfrac{P^2}{4m^2} = -\tfrac{M^2}{4m^2}. \tag{3.23}$$

Working with two particles of equal mass m, the momentum partitioning parameter η in (3.12) is chosen to be $\eta = \frac{1}{2}$ and the relative momentum is now $q = k + \frac{\alpha}{2}P$. The particle momenta q_1 and q_2 can now be written as:

$$q_1 = k + \xi P = k + \left(\frac{1+\alpha}{2}\right)P, \qquad q_2 = -k + (1-\xi)\,P = -k + \left(\frac{1-\alpha}{2}\right)P. \tag{3.24}$$

A new light-front momentum partitioning α was introduced as $\alpha = 2\xi - 1$ (the z variable from the previous section corresponds to $-\alpha$) , and because $\xi \in [0,1]$, the physical domain for α is the interval $[-1,1]$. An equal momentum fraction of $\xi = \frac{1}{2}$ is now mapped to $\alpha = 0$.

As the particles are indistinguishable and the labeling of which particle has momentum q_1 or q_2 is arbitrary, the problem must be invariant under transformations of the kind $q_1 \leftrightarrow q_2$. Equation (3.24) and (3.23) state that these transformations are equivalent to the combination of two transformations:

$$\alpha \to -\alpha \qquad\qquad \omega \to -\omega. \tag{3.25}$$

Next one can write the propagators and the interaction kernel in terms of these new variables. Starting by replacing the defintions of q_1 and q_2 from equation (3.24) into equation (3.11), the propagator product $G_0(k,P)$, which should only depend on the Lorentz invariants of equation (3.23) and α, is writ-

ten as:

$$\begin{aligned} m^4 G_0(x,\omega,t,\alpha) &= \frac{m^2}{q_1^2+m^2}\frac{m^2}{q_2^2+m^2} = \\ &= \frac{m^2}{\left(k^2+\frac{P^2}{4}(1+\alpha)^2+(1+\alpha)\,k\cdot P+m^2\right)}\frac{m^2}{\left(k^2+\frac{P^2}{4}(1-\alpha)^2-(1-\alpha)k\cdot P+m^2\right)}. \end{aligned} \tag{3.26}$$

Using the definitions of the Lorentz invariants of equation (3.23), $G_0(x,\omega,t,\alpha)$ is written as:

$$\begin{aligned} m^4 G_0(x,\omega,t,\alpha) &= \\ &= \frac{1}{\left(x+t(1+\alpha)^2+2(1+\alpha)\omega\sqrt{x}\sqrt{t}+1\right)}\frac{1}{\left(x+t(1-\alpha)^2-2(1-\alpha)\omega\sqrt{x}\sqrt{t}+1\right)}. \end{aligned} \tag{3.27}$$

Writing this a more compact way, the end result for $G_0(x,\omega,t,\alpha)$ is:

$$m^4 G_0(x,\omega,t,\alpha) = \frac{1}{(x+1+t+\alpha^2 t+2\alpha\omega\sqrt{x}\sqrt{t})^2-4t(\alpha\sqrt{t}+\omega\sqrt{x})^2}. \tag{3.28}$$

In this form, it is very easy to see that G_0 is invariant under particle exchange symmetry of equation (3.25).

The next step is to write the interaction kernel $K(q',q)$ in these new coordinates. Defining, in analogy to equation (3.12), the loop momentum q' as $q' = k' + \frac{\alpha}{2}P$, one obtains:

$$q'-q = k'+\frac{\alpha}{2}P-k-\frac{\alpha}{2}P = k'-k. \tag{3.29}$$

When writing the loop momentum it is, therefore, only necessary to determine the k' vector, which can be written as a generic four-vector, with all components populated, in hyperspherical coordinates:

$$k' = m\sqrt{x'}\begin{bmatrix}\sqrt{1-\omega'^2}\sqrt{1-y^2}\sin\vartheta\\ \sqrt{1-\omega'^2}\sqrt{1-y^2}\cos\vartheta\\ \sqrt{1-\omega'^2}y\\ \omega'\end{bmatrix}, \tag{3.30}$$

where, as in (3.22), $k'^2 = m^2 x'^2$.

The interaction kernel is defined in (3.10), and expanding the momentum variables results in (with g^2 factored out):

$$m^2 K(q',q) = \frac{m^2}{(q-q')^2+\mu^2} = \frac{m^2}{(k-k')^2+\mu^2} = \frac{m^2}{k^2+k'^2-2k\cdot k'+\mu^2}. \tag{3.31}$$

In terms of the variables of equation (3.23) and (3.30), the kernel becomes:

$$\begin{aligned} m^2 K(x,\omega,x',\omega',y) &= \frac{1}{x+x'+\beta^2-2\sqrt{x}\sqrt{x'}\Omega(\omega,\omega',y)}, \\ \Omega(\omega,\omega',y) &= \omega\omega'+\sqrt{1-\omega^2}\sqrt{1-\omega'^2}y. \end{aligned} \tag{3.32}$$

Having determined the forms of the propagators G_0 and the interaction kernel K, the only missing piece is to determine how to write the four-momentum loop integration measure $\int d^4q'$, which, using the variables of (3.30), is written as:

$$\frac{1}{2}m^4\int_0^\infty dx'x'\int_{-1}^1 d\omega'\sqrt{1-\omega'^2}\int_{-1}^1 dy\int_0^{2\pi} d\vartheta. \tag{3.33}$$

Collecting all the pieces, the BSE (equation (3.9)) to be solved is given by:

$$\begin{aligned}&\psi(x,\omega,t,\alpha) = \\ &= \frac{g^2}{m^2}\frac{1}{(2\pi)^3}\frac{1}{2}\int_0^\infty dx' x' \int_{-1}^{1} d\omega' \sqrt{1-\omega'^2} G_0(x',\omega',t,\alpha) \int_{-1}^{1} dy K(x,\omega,x',\omega',y)\psi(x',\omega',t,\alpha),\end{aligned} \tag{3.34}$$

where the mass factors in equations (3.28) and (3.32) were absorbed in the definition of G_0 and K respectively, and the trivial integration in ϑ was already performed. The Bethe-Salpeter equation (3.34) is symmetric with respect to the transformation (3.25), as expected, both in the external and the loop variables.

The integration in y can be done analytically, for this particular interaction kernel, using the following relation:

$$\int_{-1}^{1} dy \frac{1}{A-By} = \frac{\log(A+B) - \log(A-B)}{B}. \tag{3.35}$$

3.4.2 Analytic structure of the Bethe-Salpeter equation

One can now explore the analytic structure of the Bethe-Salpeter equation in order to define a contour deformation that allows recovering the desired physical solutions.

From the definitions (3.28) and (3.32), it is easily seen that the sources of all singularities and branch cuts are the propagators G_0 and the interaction kernel K.

3.4.2.1 Propagators

The process of finding the singularities of the propagator, for this specific system, is easy as the propagator is known explicitly.

It is important to remember that, in general, the propagator has to be obtained by solving the corresponding Dyson-Schwinger equation. Most problems can only be solved numerically, giving no analytical information about the location of the singularities. In principle, however, the method presented here does not need to know the exact location of all singularities — there may even exist an infinite number of them, and their exact locations may be unknown. One only needs to know a region that is guaranteed to be without singularities, and if the path can be deformed to stay within that safe region.

In any case, in the scalar model, the singularities can be analytically found by examining the denominator of G_0 and equating it to zero, solving in this case for ω:

$$(x+1+t+\alpha^2 t + 2\alpha\omega\sqrt{t}\sqrt{x})^2 - 4t(\alpha\sqrt{t}+\omega\sqrt{x})^2 = 0 \implies \omega^{\pm} = f_{\pm}(x,\alpha,t). \tag{3.36}$$

As the denominator is of order ω^2, there are two solutions for the equation, $\omega_{\pm}$:

$$\omega_{+} = -\frac{x+1+(1+\alpha)^2 t}{2(1+\alpha)\sqrt{x}\sqrt{t}}, \qquad \omega_{-} = \frac{x+1+(1-\alpha)^2 t}{2(1-\alpha)\sqrt{x}\sqrt{t}}. \tag{3.37}$$

After the intergration in ω' in equation (3.34), these two poles will become branch cuts in the complex x plane. For simplicity, the plane $\sqrt{x}$ will be considered instead. Each pole in (3.37) is a quadratic function in $\sqrt{x}$, so there will be two curves for each pole, labeled $\sqrt{x}^{\lambda}_{\pm}$, where the subscript is related to

the pole in ω and the superscript λ distinguishes between the two curves for each pole:

$$\sqrt{x}_{+}^{\lambda=+} = -(1+\alpha)\left[\sqrt{t}\omega + i\sqrt{t(1-\omega^2) + \frac{1}{(1+\alpha)^2}}\right], \tag{3.38}$$

$$\sqrt{x}_{+}^{\lambda=-} = -(1+\alpha)\left[\sqrt{t}\omega - i\sqrt{t(1-\omega^2) + \frac{1}{(1+\alpha)^2}}\right], \tag{3.39}$$

$$\sqrt{x}_{-}^{\lambda=+} = (1-\alpha)\left[\sqrt{t}\omega + i\sqrt{t(1-\omega^2) + \frac{1}{(1-\alpha)^2}}\right], \tag{3.40}$$

$$\sqrt{x}_{-}^{\lambda=-} = (1-\alpha)\left[\sqrt{t}\omega - i\sqrt{t(1-\omega^2) + \frac{1}{(1-\alpha)^2}}\right]. \tag{3.41}$$

It is instructive to look at some special points along the curves $\sqrt{x}_{\chi}^{\lambda}$, and for that purpose we write the curves as:

$$\sqrt{x}_{\chi}^{\lambda} = A(\chi,\alpha,t)i\left(\omega + \lambda\sqrt{\omega^2 + C(\chi,\alpha,t)^2}\right). \tag{3.42}$$

These relations can be thought of as parametric representations of the variable $\omega \in [-1,1]$ that describe a curve in the $\sqrt{x}$ plane where the integral has a branch cut. These cuts depend on $\sqrt{t}$ and α — this must be taken into consideration when designing an integration path. The main features of these curves are described in the appendix A

At $\alpha = 0$, the $\sqrt{x}_{+}^{\lambda}$ and $\sqrt{x}_{-}^{\lambda}$ cuts coincide. This point also marks the location where the paths exchange their roles - that is, the paths obey the following transformation:

$$\alpha \to -\alpha \implies \sqrt{x}_{\chi}^{\lambda} \to -\sqrt{x}_{-\chi}^{\lambda}, \tag{3.43}$$

where $\chi = \pm$ was used to denote the subscript.

At the endpoints $\omega = \pm 1$, the curves take a very simple form:

$$\omega = -1 \implies \sqrt{x}_{\chi}^{\lambda} = \begin{cases} -(1-\alpha)\sqrt{t} + i\lambda, & \chi = - \\ (1+\alpha)\sqrt{t} - i\lambda, & \chi = + \end{cases}, \tag{3.44}$$

$$\omega = 1 \implies \sqrt{x}_{\chi}^{\lambda} = \begin{cases} (1-\alpha)\sqrt{t} + i\lambda, & \chi = - \\ -(1+\alpha)\sqrt{t} - i\lambda, & \chi = + \end{cases}, \tag{3.45}$$

which help in finding a region in the $\sqrt{x}$ plane where there are no cuts, following the construction at the end of appendix A. A line passsing through the origin and crossing the point $\sqrt{t}$ avoids the branch cuts.

The construction of figure 3.2 indicates the regions that might contain the propagator branch cuts, obtained by a generalization of the curves of equation (3.42) for a fixed value of $\sqrt{t}$ and α (a more detailed argument is presented at the end of appendix A). Even though the propagator cuts for this problem will only be a subset of the shaded regions of figure 3.2, it is still instructive to consider the whole regions when designing a path deformation as this guarantees that all branch cuts are avoided, and allows for an analysis that is independent of the particular details of this problem.

In the particular case of figure 3.2, the outermost point in the green dashed line is $(1+\alpha)\sqrt{t}$. That is only the case for $\alpha > 0$. For the $\alpha < 0$ case, the outermost point will be $(1-\alpha)\sqrt{t}$. The generic form for the outermost point, for every value of $\alpha \in [-1,1]$ is therefore:

$$\max(1+\alpha, 1-\alpha)\sqrt{t}. \tag{3.46}$$

When $C(\chi,\alpha,t)$ in equation (3.42) is a pure imaginary number, as per the discussion in appendix A,

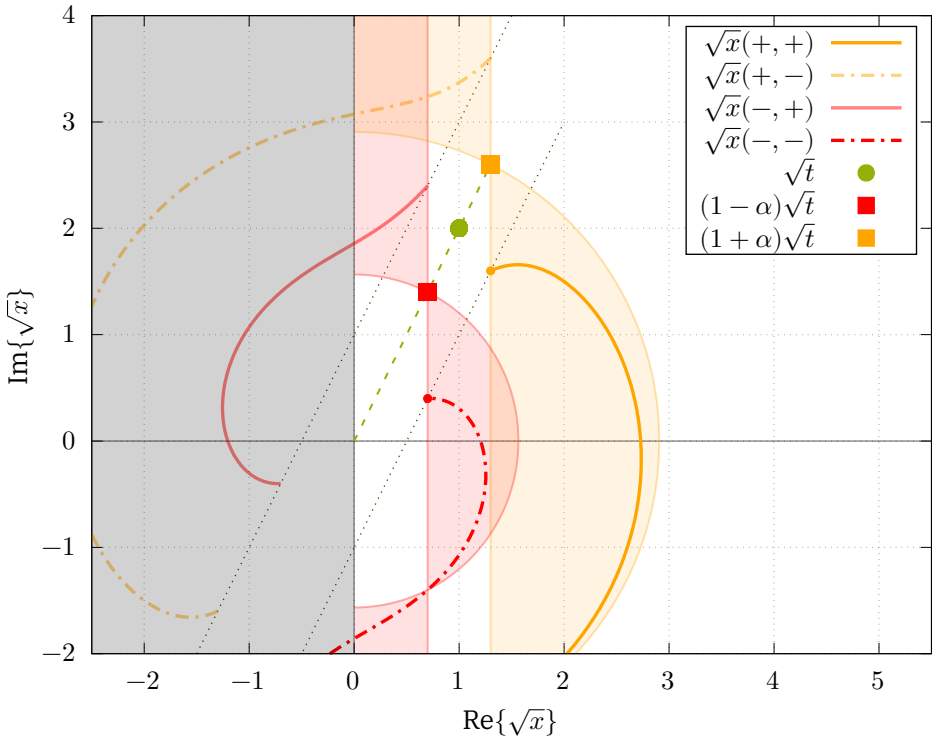

Figure 3.2: Plot of the branch cuts $\sqrt{x}^{\lambda}_{\chi} \equiv \sqrt{x}(\chi,\lambda)$ of G_0 in the complex $\sqrt{x}$ plane, for $\alpha = 0.3$ and $\sqrt{t} = 1 + 2i$. The real axis is intersected by one of the cuts generated by G_0 thus requiring contour deformations. The shaded areas indicate the regions of the $\sqrt{x}$ plane where there might be branch cuts.

the curves will close around the origin, making it impossible to create a viable contour. This condition holds if:

$$\mathrm{Re}\{C\} = \mathrm{Re}\left\{ i\left(1 + \frac{1}{t(1+\chi\alpha)^2}\right)\right\} = 0 \implies t \in \mathbb{R}, \tag{3.47}$$

that is, for purely imaginary values of $\sqrt{t}$, there are no paths that will not cross a branch cut. This limitation requires the introduction of a real part to $\sqrt{t}$ and the physical case will be recovered for $\mathrm{Re}\{\sqrt{t}\} \to 0$. It may also be possible to recover solutions of the Bethe-Salpeter equation for these ranges of values of $\sqrt{t}$ by an analytic continuation of the results with a non-zero real part.

The cuts will cross the real axis when the point $\omega = -1$, for the $(\chi,\lambda) = (+,+)$ cut, or the point $\omega = 1$, for the $(\chi,\lambda) = (-,-)$ cut cross the real axis. Using the results in (3.45) and (3.44), the condition is:

$$\mathrm{Im}\{(1+\alpha)\sqrt{t} - i\} < 0 \ \wedge\ \mathrm{Im}\{(1-\alpha)\sqrt{t} - i\} < 0 \implies \mathrm{Im}\{\sqrt{t}\} < \frac{1}{1-\alpha} \ \wedge\ \mathrm{Im}\{\sqrt{t}\} < \frac{1}{1+\alpha}. \tag{3.48}$$

These relations can be inverted and give a range in α, where, for a given value of $\sqrt{t}$, it is possible to integrate without contour deformations, which can be helpful when solving the Bethe-Salpeter equation numerically.

3.4.2.2 Interaction Kernel

The interaction kernel, as written in equation (3.32), also has singularities that need to be addressed. By equating the denominator of the kernel to zero, the location of the singularities can be written as a

function of the integration variable $\sqrt{x'}$:

$$\sqrt{x'}_{\chi} = \sqrt{x}\Omega + \chi i\sqrt{x(1-\Omega^2)+\beta^2}, \tag{3.49}$$

where $\chi = \pm$ and Ω is the function defined in equation (3.32). The denominator is quadratic in $\sqrt{x'}$, so there are two sets of singularites, distinguished by χ. Note that there is no dependence in α nor in $\sqrt{t}$.

The main difference, however, is that the kernel cuts are now, due to Ω, functions of ω, ω' and y. A look at the definition of Ω, while keeping in mind that $\omega, \omega', y \in [-1, 1]$, reveals that $\Omega(\omega, \omega', y)$ can only take on real values in the same region $[-1, 1]$. Thus, one can consider Ω as a variable itself, with domain $[-1, 1]$. Equation (3.49), therefore, defines two curves via two parametric equations of the variable $\Omega \in [-1, 1]$, and can be written in the form:

$$\sqrt{x}\left(\Omega - \chi\sqrt{\Omega^2 - \left(1 + \frac{\beta^2}{x}\right)}\right), \tag{3.50}$$

which has the form of the propagator cuts (the analysis in appendix A applies).

A complication appears due to the fact that equation (3.34) is an integral equation. To solve this equation, it is necessary to evaluate the Bethe-Salpeter wave function in the same path in $\sqrt{x}$ as it is integrated — solving the integral equation requires the reintroduction of the obtained solution in the right-hand side of equation (3.34), as it will be solved by iteration.

Two consequences emerge: firstly, the accessible region in the x plane is dictated by the integration path picked in the x' integration. Secondly, because the kernel cuts depend on x as well, for each point in the x plane that is evaluated, the kernel cuts define a different region in the x' plane. To make sure that no branch cuts are intersected, the selected path in x' for a given value of x must also be outside any of the regions defined by the previous values of x [33].

In order to find a region where it is possible to define a path in x', it is again helpful to study the endpoints of the branch cuts, that is, the points $\Omega = \pm 1$. Simply evaluating equation (3.49) at $\Omega = \pm 1$ results in:

$$\Omega = -1 \implies \sqrt{x'}_{\chi} = \begin{cases} -\sqrt{x} - i\beta, & \chi = - \\ -\sqrt{x} + i\beta, & \chi = + \end{cases}, \qquad \Omega = 1 \implies \sqrt{x'}_{\chi} = \begin{cases} \sqrt{x} - i\beta, & \chi = - \\ \sqrt{x} + i\beta, & \chi = + \end{cases}. \tag{3.51}$$

The endpoints define two vertical lines: one that goes through the $\Omega = -1$ points, and another that goes through the $\Omega = 1$ points. Just like the propagator cuts, the kernel cuts will start at one of these lines and end at the other. This property ensures that, as long as the real part in the path in $\sqrt{x'}$ keeps increasing, the cuts belonging to previous points in the path will not be crossed.

The limiting case $\beta \to 0$ is also of particular interest as the cuts define a circle of radius $\sqrt{x}$, centered in the origin (just like at the end of appendix A).

The combination of these two properties entails that if a path is such that the value of $\mathrm{Re}\,\sqrt{x'}$ and $|\sqrt{x'}|$ always increases, then it will avoid the cuts of the kernel. This can be seen in the construction of figure 3.3 (note the similarities with figure 3.2), and keeping in mind that a structure like that will appear for every value of $\sqrt{x}$ that is considered [33].

3.4.3 Integration path

Having explored the analytic structure of both the propagators and the interaction kernel, it is now possible to design an integration path in the $\sqrt{x'}$ plane that avoids the branch cuts, while starting at the origin and ending at $+\infty$ on the real axis.

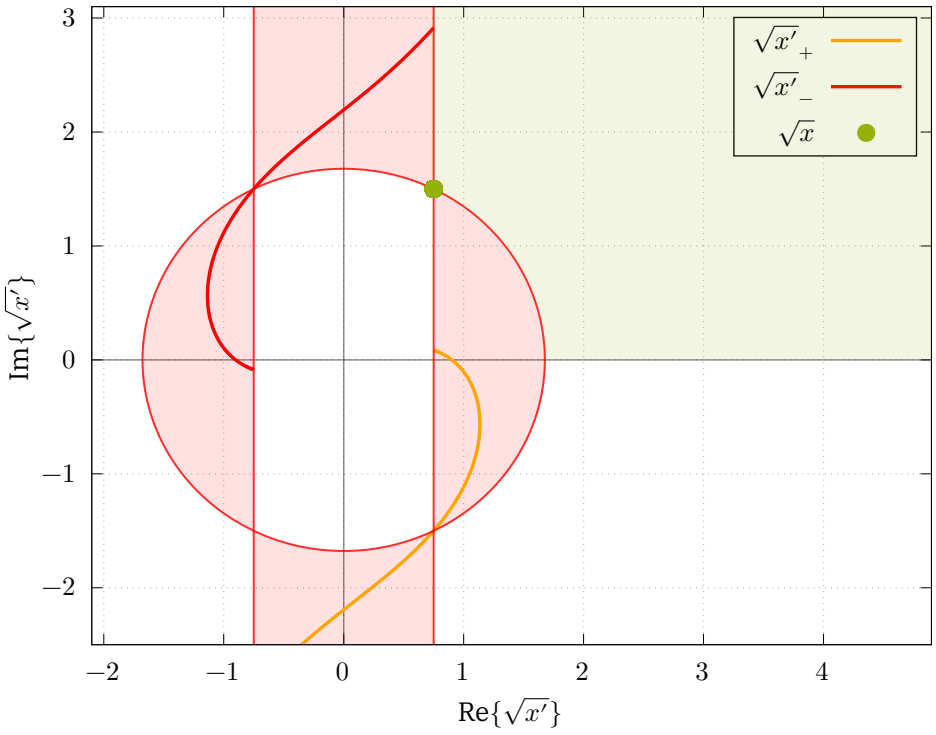

Figure 3.3: Plot of the kernel cuts $\sqrt{x'}_\chi$ for $\beta = 2$ and $\sqrt{x} = 1 + 2i$. The red shaded regions mark the possible location of the cuts, while the green region marks a safe region for the next value of $\sqrt{x}$.

Two major constraints need to be considered, which are the summary of the properties of the propagators and the kernel cuts.

The propagator cuts dictate the necessity that the path, which starts at the origin, exits the outermost circle at the point

$$\sqrt{\tau} \equiv \max\left(1+\alpha, 1-\alpha\right)\sqrt{t}. \tag{3.52}$$

The path also needs to avoid the same circle when returning to the real axis.

On the other hand, the kernel cuts require that the path always keeps increasing in both the absolute value and in the real part. In order to comply with these requirements, the non-deformed path is split into three different segments, each parametrized by $\gamma_1(z)$, $\gamma_2(z)$ and $\gamma_3(z)$, such that:

$$\int_0^\infty dx' = 2\int_0^\infty \sqrt{x'}d\sqrt{x'} \to 2\left(\int_{\gamma_1} + \int_{\gamma_2} + \int_{\gamma_3}\right)\sqrt{x'}d\sqrt{x'}, \tag{3.53}$$

keeping in mind that the original integration in the BSE in (3.34) is defined in x' while the paths γ_i define the contour in the $\sqrt{x'}$ plane, thus requiring a change of variable.

The first path, γ_1, is the portion that goes from the origin to outside the circle defined by the propagator cuts, via the $\sqrt{t}$ line. The second path, γ_2, returns to the real axis, and the third path, γ_3, then continues on the real axis up to infinity.

To assist the numerical calculations, the three path components are parametrized by a z variable, $z \in [-1, 1]$. It is also helpful to define some auxiliary quantities. A straight line which starts in A and ends in B, with $A, B \in \mathbb{C}$, is parametrized (as a function of a variable $z \in [-1, 1]$) by:

$$\gamma(z) = Bz_+ + Az_-, \qquad z_+ = \frac{1+z}{2}, \qquad z_- = \frac{1-z}{2}. \tag{3.54}$$

The first derivative of γ, with respect to z, is naturally:

$$\gamma'(z) = \frac{B-A}{2}. \tag{3.55}$$

One can then define explicitly the three path components to be used in this work. The first component is as the straight line going from the origin to the point $\sqrt{\tau}$:

$$\gamma_1(z) = \sqrt{\tau} z_+, \qquad \gamma_1'(z) = \frac{\sqrt{\tau}}{2}. \tag{3.56}$$

The second component, γ_2, which goes from $\sqrt{\tau}$ back to the real axis while avoiding the propagator cuts, is perhaps the most complicated portion of the path. This component must increase the absolute value of the $\sqrt{x'}$ while also decreasing its argument (to return to the real axis). For that, it is helpful to write:

$$\gamma_2(z) = R(z) e^{i\Theta(z)}, \tag{3.57}$$

where $R(z)$ and $\Theta(z)$ are two linear functions in z. The radial component $R(z)$ is chosen such that the absolute value of $\sqrt{x'}$ increases along the path and reaches the real axis with $|\sqrt{x}| = r_{max}|\sqrt{\tau}|$. The angular component $\Theta(z)$ is such that it starts at $\arg(\sqrt{\tau})$ and ends at zero. The analytical expressions for the two functions are:

$$R(z) = |\sqrt{\tau}| \left(r_{max} z_+ + z_-\right), \tag{3.58}$$

$$\Theta(z) = \arg(\sqrt{\tau}) z_-. \tag{3.59}$$

The respective derivatives are:

$$R'(z) = |\sqrt{\tau}| \left(\frac{r_{max}-1}{2}\right), \qquad \Theta'(z) = -\frac{\arg(\sqrt{\tau})}{2}, \tag{3.60}$$

so one can write the derivative of γ_2 as:

$$\gamma_2'(z) = R(z)' e^{i\Theta(z)} + iR(z)\Theta'(z) e^{i\Theta(z)} = \left(R'(z) + i\Theta'(z) R(z)\right) e^{i\Theta(z)}. \tag{3.61}$$

The last component of the integration path, γ_3, is the line going from $\sqrt{x'} = r_{max}|\sqrt{\tau}|$ up to ∞, always along the real axis. The desired function must display two aspects: it must go to ∞ for $z \to 1$ and it must be equal to $c \equiv r_{max}|\sqrt{\tau}|$ for $z = -1$. The first aspect is taken care of by defining γ_3 as a rational function of z, with denominator $1 - z$. The second aspect is also taken care of by defining the numerator of γ_3 as $1 + z + 2c$. The third component can then be written as:

$$\gamma_3(z) = \frac{1+z+2c}{1-z}, \qquad \gamma_3'(z) = \frac{2\,(1+c)}{(1-z)^2}. \tag{3.62}$$

An illustrative plot is given in figure 3.4.

3.4.4 From Bethe-Salpeter wavefunctions to Light-Front wavefunctions

Having discussed and presented a tentative integration path that can go around the singularities of both the propagator and the interaction kernel, one may calculate the BSWF using the BSE of (3.34).

The next step in the calculation of the LFWF, and afterwards, the PDF, is to solve explicitly the integrals of equations (2.41) and (2.42). To this end, one needs to understand the integration in q^- and implement the condition $k^+ = 0$ used in the definition of the four-vector q in section (3.2). This is done

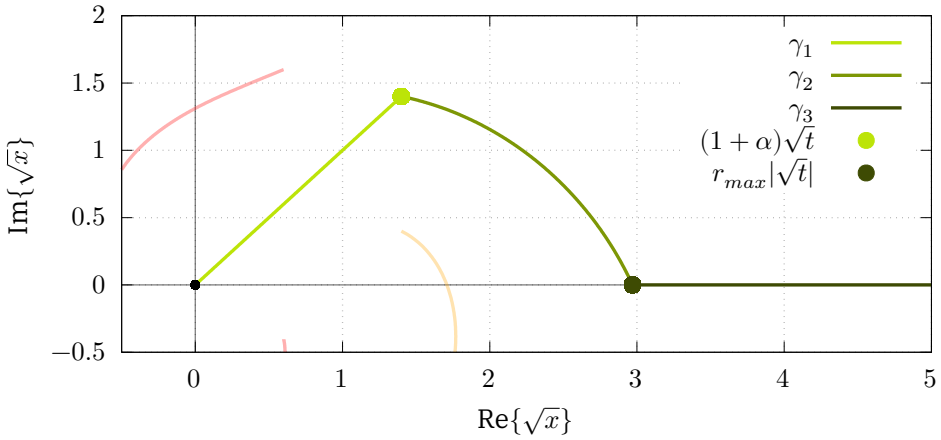

Figure 3.4: Plot of the integration path for $\sqrt{t} = 1 + i$, $\alpha = 0.4$ and $r_{max} = 1.5$. The red and orange lines are the propagator cuts.

by considering k and P in a moving frame:

$$P = 2m\sqrt{t}\begin{bmatrix} 0 \\ 0 \\ \sqrt{1-Z^2} \\ Z \end{bmatrix}, \qquad k = m\sqrt{x}\begin{bmatrix} \sqrt{1-z^2}\sqrt{1-y^2}\sin\vartheta \\ \sqrt{1-z^2}\sqrt{1-y^2}\cos\vartheta \\ \sqrt{1-z^2}y \\ z \end{bmatrix}. \tag{3.63}$$

The total momentum P gains an extra variable Z, and the condition $k^+ = 0$ implies that $y = iz/\sqrt{1-z^2}$. The Lorentz invariants are equal to the ones of equation (3.23):

$$x = \frac{x^2}{m^2} = \frac{k_\perp^2}{m^2}, \qquad \omega = \hat{k}\cdot\hat{P}, \qquad t = \frac{P^2}{4m^2}. \tag{3.64}$$

The variable x now plays the role of the transverse momentum squared. One can now write q^- as

$$q^- = -\frac{2m^2}{P^+}\left(2\sqrt{x}\sqrt{t}\omega + \alpha t\right). \tag{3.65}$$

x, t and α are all fixed external variables to the integral of (2.41) — ω is the integration variable. As the original domain in q^- is $(-i\infty, i\infty)$ and $\sqrt{t} = \frac{iM}{2m}$, then $\omega \in (-\infty, \infty)$. The integral of equation (2.41) defines the LFWF, which can also be written in its adimensional form $\tilde{\Psi}_{LF}$:

$$\Psi_{LF}(x,\alpha) = d\widetilde{\Psi}_{LF}(x,\alpha) = d\left(\frac{2\sqrt{x}\sqrt{t}}{i\pi}\int_{-\infty}^{\infty} G_0(x,\omega,\alpha,t)\,\psi(x,\omega,\alpha,t)\,d\omega\right), \tag{3.66}$$

where $d \in \mathbb{C}$ is just a constant, and the BSWF Ψ is expressed in terms of the amplitude ψ.

The parton distribution amplitude $\phi(\alpha)$ is the integral of the LFWF along the path in x, and a dimensionless version $\tilde{\phi}(\alpha)$ can be defined as well:

$$\phi(\alpha) = \int \Psi_{LF}(x,\alpha)\,dx = d\int \widetilde{\Psi}_{LF}(x,\alpha)\,dx = d\tilde{\phi}(\alpha). \tag{3.67}$$

As P and k are now in the moving frame, the solution of the BSE is $\Psi(x,z,y,Z,t,\alpha)$ is now a function of the kinematic quantities of (3.63), with

$$\hat{k}\cdot\hat{P} = zZ + \sqrt{1-z^2}\sqrt{1-Z^2}y \to z\left(Z + i\sqrt{1-Z^2}\right), \tag{3.68}$$

where the last statement is obtained by imposing the $k^+ = 0$ condition. As the BSWF is Lorentz-invariant, the moving frame solution must match the rest-frame solution:

$$\Psi(x, y, z, Z, t, \alpha) = \Psi(x, \omega, t, \alpha), \tag{3.69}$$

and the integral of equation (3.66) can be done with the rest-frame Ψ solution from solving equation (3.34).

Repeating the argument of section 3.4.2.2, the BSWF is only known in the integration domain, that is, $\omega \in [-1, 1]$, and x along the path used, which will either be the standard integration path $x \in [0, \infty)$, or the deformed path, if the cuts so demand.

To obtain the LFWF it is necessary to obtain the values of the BSWF for all $\omega \in \mathbb{C}$ (or at least, in an appropriate domain), from the information given by the BSE. This will be achieved by analytic continuation of the results of the BSE in $\omega \in [-1, 1]$ using the Schlessinger method (details in section 3.5.1).

The path in $\sqrt{x}$ used in the BSE already avoids the branch cuts of the propagators G_0, so as long as the same path is used, there is no risk of the propagator singularities interfering in the ω integration. The only unknown of this integration relates to the analytic structure of the amplitude ψ itself. The BSE guarantees that there are no singularities for $|\omega| \leq 1$. For comparisons, it is instructive to consider a monopole ansatz for the amplitude:

$$\psi = \frac{m^2}{q^2 + m^2\gamma} = \frac{1}{x + \gamma + \alpha^2 t + 2\alpha\sqrt{x}\sqrt{t}\omega}, \tag{3.70}$$

where γ is a numerical constant. It has a single pole in ω:

$$\omega_0 = -\frac{x + \gamma + \alpha^2 t}{2\alpha\sqrt{x}\sqrt{t}}, \qquad \sqrt{x}_0^{\lambda} = -\alpha\sqrt{t}\left[\omega + i\lambda\sqrt{\omega^2 - 1 + \frac{\gamma}{\alpha^2 t}}\right]. \tag{3.71}$$

The cut produced is just like the ones from the propagator, and the path in $\sqrt{x}$, should, in principle, avoid it already. As an additional check, the amplitude was analytically continued and it was empirically verified that the integration path $\omega \in (-\infty, \infty)$ is free of singularities, because these only appear near the imaginary axis, outside the $|\omega| < 1$ region.

Although a more rigorous statement about the analytic structure of the amplitude is desirable and will be the subject of future work, the fact that the application of the method is possible even without this statement is one of its advantages.

3.5 Numerical methods

After defining the equations and integrations needed, we now describe briefly the numerical methods used.

For this work, the focus is mainly on two numerical problems: the solution of integrals and integral equations, as well as the numerical analytic continuation of functions based on samples calculated on a finite set of points in a specific domain.

In this work, for the contour deformation method, the solution of the BSE of (3.34) is based on Gauss-Legendre ($W(x) = 1$) integration for the x' variable, and a Gauss-Chebyshev ($W(x) = \sqrt{1 - x^2}$) for the ω' variable. More details about these integration methods can be found in appendix B. Both the Gauss-Legendre and Chebyshev integrations are done in the domain $[-1, 1]$. This is the reason why the path segments of section 3.4.3 were parametrized from $[-1, 1]$. In the cases where the cuts do not cross the real axis and the usual integration path $\sqrt{x'} \in [0, \infty)$ can be used with no deformation, the

following mapping transforms the $u \in [-1, 1]$ interval into $\sqrt{x'} \in [0, \infty)$:

$$\sqrt{x'} = \frac{1+u}{1-u}, \qquad d\sqrt{x'} = \frac{2}{(1-u)^2} du. \tag{3.72}$$

In the case of the LFWF in equation (3.66), another mapping is used to convert the Gauss-Legendre integration in the range $u \in [-1, 1]$ (note that the $\sqrt{1-\omega^2}$ factor is not present) into $\omega \in (-\infty, \infty)$:

$$\omega = \frac{u}{1-u^2}, \qquad d\omega = \frac{1+u^2}{(1-u^2)^2} du. \tag{3.73}$$

In the ω' integration of the Bethe-Salpeter equation, although the selected path in x' avoids the propagator singularities, they can still get close to the integration path and cause a more vigorous variation of the integrand. Using the fact that the Chebyshev polynomials of the second kind $U_l(x)$ have a higher density of zeros near the end-points (as seen in the right of figure B.1), one can define an adaptative ω integration which ensures that there is a greater density of sampling points near the singularities in the ω plane.

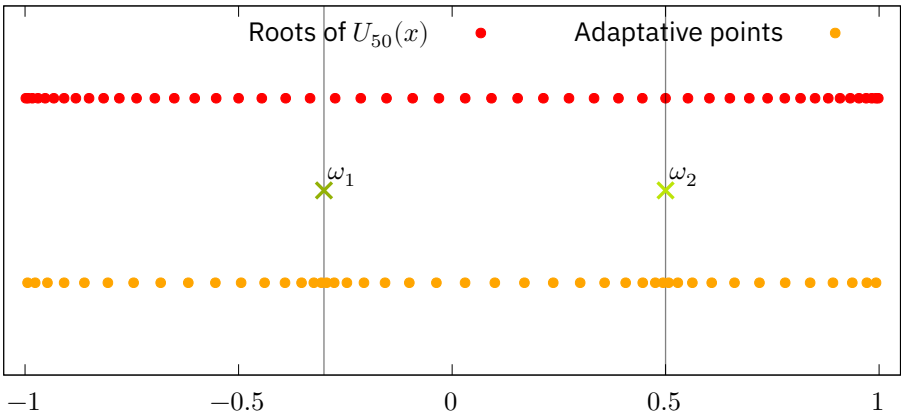

Figure 3.5: Comparison between the usual sampling by the roots of the $U_{50}(x)$ polynomial, and the adaptative ω integration method, for two example roots ω_1 and ω_2. Both sets contain 50 points.

The basic idea is that, if the singularities in the complex ω plane are within a certain distance to the path $\omega \in [-1, 1]$, the integration is split into three: one that starts at $\omega = -1$ and goes until the real part of the first singularity; another that then goes to the real part of second singularity and the last that brings it to the $\omega = 1$ point. As can be seen in figure 3.5, this method increases the density of sampling points near the singularities.

With the sample points determined and the weights calculated, for both the x' and ω' integrations, the integration of (3.34) can be written as:

$$\Psi(x_m, \omega_n) = \sum_i^{N_x} \sum_j^{N_\omega} \mathcal{K}(x'_i, \omega'_j; x_m, \omega_n) \Psi(x'_i, \omega'_j) w_i^x w_j^z, \tag{3.74}$$

where the product of G_0 and the integration in y of the interaction kernel have been combined into the function $\mathcal{K}$. The function Ψ will be sampled on a discrete number of points — the domain has been discretized into a grid of $N_x \times N_\omega$ points.

Looking closely at equation (3.74), one can identify the resemblance to the multiplication of a matrix with a vector. Just like the usual infinite-dimensional vector spaces for functions, it is possible to associate the discretized Ψ as a vector in some vector space $\mathcal{S}$ — finite-dimensional in this case, with

dimensions $N_x \times N_\omega$. In that case, the integration in x' and ω' of some function Ψ multiplied by $\mathcal{K}$ can be seen as an operator $\mathcal{K} : \mathcal{S} \to \mathcal{S}$.

The vector space of dimension N_x relating to discretized functions of x' is defined as S_x, and the one of dimension N_ω relating to functions of ω is similarly defined as S_ω. A definite integral $I = \int h(x)f(x)dx$ of a vector f in these spaces is represented by a $(1 \times N)$ matrix so that the end result is a scalar value: $\mathcal{J} : S \to \mathbb{C}$ and:

$$\mathcal{J} = \begin{bmatrix} h(x_1)w_1 & h(x_2)w_2 & h(x_3)w_3 & h(x_4)w_4 & ... \end{bmatrix}. \tag{3.75}$$

An integral which has an external dependency, like $I(z) = \int H(z, z')f(z')dz'$ is represented as a square matrix $(N \times N)$, and $I(z) : S \to S$ can be represented as:

$$I(z) = \begin{bmatrix} H(z_1, z_1)w_1 & H(z_1, z_2)w_2 & H(z_1, z_3)w_3 & H(z_1, z_4)w_4 & ... \\ H(z_2, z_1)w_1 & H(z_2, z_2)w_2 & H(z_2, z_3)w_3 & H(z_2, z_4)w_4 & ... \\ \vdots & \vdots & \vdots & \vdots & \ddots \end{bmatrix}. \tag{3.76}$$

In this context, the vector Ψ:

$$\Psi = \begin{bmatrix} \Psi(x_1, \omega_1) & ... & \Psi(x_2, \omega_1) & ... & \Psi(x_{N_x}, \omega_{N_\omega}) \end{bmatrix}^T, \tag{3.77}$$

is in the product vector space $S_x \otimes S_\omega$, of dimension $N_x \times N_\omega$, and similarly, the integral operator is also in the product space and will be represented by a square $N_x N_\omega \times N_x N_\omega$ matrix. It is the tensorial product of two integrations, one in S_x and the other in S_ω. In this perspective it is simple to write the matrix form of $I(x, \omega) = I(x) \otimes I(\omega)$ as

$$\begin{bmatrix} \left[\mathcal{K}(x_1, x_1)_{ij} w_j^\omega\right] w_1^x & \left[\mathcal{K}(x_1, x_2)_{ij} w_j^\omega\right] w_2^x & \left[\mathcal{K}(x_1, x_3)_{ij} w_j^\omega\right] w_3^x & \left[\mathcal{K}(x_1, x_4)_{ij} w_j^\omega\right] w_4^x & ... \\ \left[\mathcal{K}(x_2, x_1)_{ij} w_j^\omega\right] w_1^x & \left[\mathcal{K}(x_2, x_2)_{ij} w_j^\omega\right] w_2^x & \left[\mathcal{K}(x_2, x_3)_{ij} w_j^\omega\right] w_3^x & \left[\mathcal{K}(x_2, x_4)_{ij} w_j^\omega\right] w_4^x & ... \\ \left[\mathcal{K}(x_3, x_1)_{ij} w_j^\omega\right] w_1^x & \left[\mathcal{K}(x_3, x_2)_{ij} w_j^\omega\right] w_2^x & \left[\mathcal{K}(x_3, x_3)_{ij} w_j^\omega\right] w_3^x & \left[\mathcal{K}(x_3, x_4)_{ij} w_j^\omega\right] w_4^x & ... \\ \left[\mathcal{K}(x_4, x_1)_{ij} w_j^\omega\right] w_1^x & \left[\mathcal{K}(x_4, x_2)_{ij} w_j^\omega\right] w_2^x & \left[\mathcal{K}(x_4, x_3)_{ij} w_j^\omega\right] w_3^x & \left[\mathcal{K}(x_4, x_4)_{ij} w_j^\omega\right] w_4^x & ... \\ \vdots & \vdots & \vdots & \vdots & \ddots \end{bmatrix}, \tag{3.78}$$

where the shorthand notation $\left[\mathcal{K}(x_1, x_1)_{ij} w_j^\omega\right]$ represents a $N_\omega \times N_\omega$ matrix just like equation (3.76).

The calculation of equation (3.74) is simply the multiplication of the matrix $I(x, \omega)$ with the vector Ψ. It is in this sense that the operators in equation (3.21) can be numerically defined and manipulated.

Seeing equation (3.74) in this perspective has two main advantages:

- As the integral and the function are simply matrices and vectors, the structure of (3.34) is an eigenvalue equation, where the standard linear algebra tools and algorithms can be applied. For example, in this work the ground state (largest eigenvalue) is obtained by the power method, that is, starting with an initial guess for Ψ and iterating repeatedly the application of the integration operation. More sophisticated methods for obtaining the eigenspectrum can also be used, granting access to other eigenvectors and eigenvalues.

- It is also possible to do basis transformations. In the discussion so far, a basis comprised of the elements $e_{ij} = \delta_{ij}$ was used — which corresponds to functions which are zero everywhere, except for the point (x_i, ω_j), where they take the value of 1. If suitable, it is possible to expand the functions in any set of orthonormal functions allowing, for example, for the exploitation of some symmetries in the system, or the imposition of a particular desired form.

3.5.1 Numerical Analytic Continuation

Analytic continuation is the problem of extending the domain in the complex plane where a particular analytic function is defined.

In this work, analytic continuation is used for two purposes.

- The first use is to extend the domain of the BSWF in the ω variable, from $\omega \in [-1, 1]$ given by the BSE, to $\omega \in \mathbb{C}$ needed in the definition of the LFWF.

- The second use is to evaluate both the BSWF and the LFWF on the real axis of x after it has been computed for $x \in \mathbb{C}$, for the cases where the cuts prevent the direct integration in the real axis.

The method used for the calculation of the analytic continuations is based on the Padé approximants method. A Padé approximant of some function $f(x)$ is a rational function of some order, whose power series matches the one for f (again up to some power in x, which defines the order) [57, 58]:

$$R(x) = \frac{P_N(x)}{Q_M(x)} = \frac{\sum_k^N p_k x^k}{1 + \sum_k^M q_k x^k} \approx \sum_k f_k x^k, \tag{3.79}$$

where f_k are the coefficients of the power series for f. The main advantages of this method, compared, for example to a polynomial expansion, is the ablity to reproduce the poles of the function f.

In the cases considered in this work, the available information is the set of function values given in a grid, not their series coefficients. For that reason, a modification of the Padé method, the *Schlessinger Point method*, is used instead [58].

Taking as input $n_p \equiv N + M + 1$ points $\{x_i, f(x_i)\}$, the idea is to define a rational function, such that $R(x_i) = f(x_i)$ at the input points. The points are arbitrary and can be chosen to best capture the desired properties of f. $R(x)$ is defined via a continued fraction:

$$R(x) = \cfrac{f(x_1)}{1 + \cfrac{a_1(x - x_1)}{1 + \cfrac{a_2(x - x_2)}{1 + \cfrac{a_3(x - x_3)}{1 + \cfrac{a_4(x - x_4)}{1 + \ldots}}}}} \tag{3.80}$$

or, by defining a set of functions $\mathcal{Z}_k$:

$$R(x) = \frac{f(x_1)}{1 + \mathcal{Z}_1} = \cfrac{f(x_1)}{1 + \cfrac{a_1(x - x_1)}{1 + \mathcal{Z}_2}} = \ldots, \qquad \mathcal{Z}_k = \frac{a_k(x - x_k)}{1 + \mathcal{Z}_{k+1}} \Leftrightarrow \mathcal{Z}_{k+1} = \frac{a_k(x - x_k)}{\mathcal{Z}_k} - 1, \tag{3.81}$$

where, if $x = x_k$, then $\mathcal{Z}_k = 0$, effectively truncating the continued fraction.

Imposing the condition $R(x_i) = f(x_i)$ leads to recorrence conditions that allow for the calculation of the $\{a_j\}$ coefficients. Starting with the simplest case, substituting x_1 into R leads to:

$$R(x_1) = \frac{f(x_1)}{1 + 0} = f(x_1). \tag{3.82}$$

Then, substituting in x_2 and imposing $R(x_2) = f(x_2)$ leads to :

$$f(x_2) = \frac{f(x_1)}{1 + a_1(x_2 - x_1)}, \qquad \mathcal{Z}_1 = \frac{f(x_1)}{f(x_2)} - 1 \Leftrightarrow a_1 = \frac{\mathcal{Z}_1}{x_2 - x_1}, \tag{3.83}$$

providing the first term in the set $\{a_k\}$, which has exactly $n_p - 1$ elements.

The calculation of the remaining a coefficients is done by recurrence using equation (3.81). For example, to calculate the i-th coefficient, a_i:

$$\mathcal{Z}_1 = \frac{f(x_1)}{f(x_{i+1})} - 1, \qquad \mathcal{Z}_{k+1} = \frac{a_k(x_{i+1} - x_k)}{\mathcal{Z}_k} - 1, \qquad \mathcal{Z}_{i+1} = 0 = \frac{a_i(x_{i+1} - x_i)}{\mathcal{Z}_i} - 1. \tag{3.84}$$

There are, however, some caveats in algorithms like these. Firstly, although the order in which the input points are fed into the algorithm should result in the same function, the individual coefficients will be different. Secondly, it is advisable to avoid inputting points x_i where $f(x_i) = 0$. Looking at (3.84), it is simple to see that, if $f(x_{i+1}) = 0$, then $\mathcal{Z}_1 \to \infty$, which implies that the coefficient $c \to \infty$, prematurely truncating the continued fraction. Similarly, points x_i such that $f(x_i) = f(x_1)$ will cause the same situation, but in the $\mathcal{Z}_2$ coefficient.

Lastly, as all coefficients are calculated from the previous, any uncertainties in the input data will propagate along the calculations. This may cause some significant deviations in the function evaluation, mainly in regions far away from the input points. This issue may become important, for example, when working with functions that depend on external variables and where some expected symmetries might not be preserved exactly realized when the continuation is performed.

Nevertheless, if the application of the Schlessinger method is done with these caveats in mind, it can be a very powerful extrapolation method, as can be seen from the following example.

Suppose the exact function to be continued is $f(x) = \frac{1}{1+(2x)^2}$. The series expansion of f, which is defined as $g(x)$ is, up to the 8th power:

$$g(x) = 1 - 4x^2 + 16x^4 - 64x^6 + 256x^8 + \mathcal{O}(x^9), \tag{3.85}$$

with convergence radius $|x| < \frac{1}{2}$.

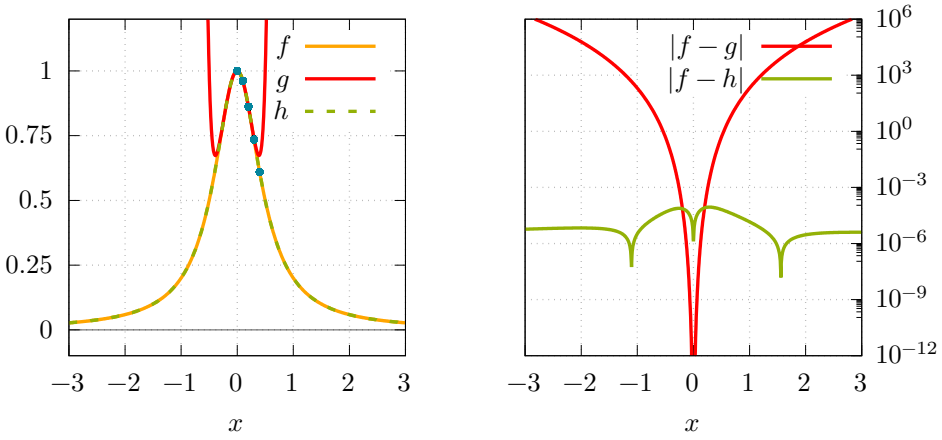

Figure 3.6: Comparison between the two approximation methods for the function f: series expansion g and the Schlessinger point method h. The blue points are the ones used as input to the Schlessinger method. On the right: logarithmic plot of the absolute error of the approximations.

In practical uses, there are limitations in the number of points x_i and the numerical precision of the function values $f(x_i)$. Suppose, in this case, that is only possible to compute five points up to the sixth decimal place from the function f. The application of the Schlessinger method calculates the function $h(x)$ from the five points, shown in table 3.1.

x_i	$f(x_i)$
0	1.000000
0.1	0.961538
0.2	0.862069
0.3	0.735294
0.4	0.609756

Table 3.1: List of the input points used in the application of the Schlessinger method the function $f(x)$.

The result for $h(x)$ is:

$$h(x) = \frac{0.250009 - 0.0000193172x}{0.250009 - 0.0000152177x + x^2} = \frac{1 - 0.0000772659x}{1 - 0.000608687x + 3.99986x^2}, \tag{3.86}$$

which is a very good numerical approximation to the function $f(x)$, as can also be seen in 3.6. Note that the unwanted linear terms in x are very small compared to the other terms. Improving the numerical precision of the samples $f(x_i)$ will improve this approximation even further, and an increase in the number of points will increase the order of the numerator and the denominator (and special care must be taken, as increasing the order does not necessarily increase the accuracy). Increasing the number of points increases the order of the polynomials, which, depending on the quality of the input points, might appear with significant coefficients. This might create numerical instabilities, or worse, create spurious poles which spoil the continuation as the denominator of (3.79) always has as many zeros as its order.

Chapter 4

Results

Having established the method proposed in this work in the previous chapter 3, the results obtained by its application will now be presented. As a reminder, the main goal of this work is to provide a new method for the calculation of the light-front wavefunction (and the parton distribution amplitude), for a system of two interacting scalar particles using the model of section 3.2, which is based on contour deformations (section 3.4).

This chapter is structured as follows. In the beginning, the Nakanishi results of [31, 32] will be recreated using an implementation of the Nakanishi method created during this work (based on [31]). This implementation serves as a benchmark for some of the results obtained via the contour deformations method. Afterwards, the results for the Bethe-Salpeter amplitude and wavefunction obtained by the contour deformation method will be presented, and compared with the implementation of the Nakanishi method. Finally, the results for the light-front wavefunction and the parton distribution amplitude, obtained from the contour deformation method are presented and compared with the Nakanishi results from [31, 32].

4.1 Nakanishi method implementation

The first step of this study was to establish an implementation of the Nakanishi method following [31] that can reproduce the results from [31, 32].

Starting from the description of the Nakanishi method in section 3.3, the objective is to develop a numerical method that can solve equation (3.17), or, more specifically, the discretized version of (3.21):

$$\lambda \mathbf{B} h = \mathbf{K} h \implies \lambda h = \mathbf{B}^{-1}\mathbf{K} h. \tag{4.1}$$

The operators $\mathbf{B}$ and $\mathbf{K}$ can be written as:

$$\mathbf{B} = \int dx' B_{mn}(x,x') h_n(x'), \quad B_{mn}(x,x') = \int dz \left(\frac{2}{\pi}\sqrt{1-z^2}\right) \frac{Y_m(z) Y_n(z)}{\left[x' + \mathcal{N}(x,z)\right]^2}, \tag{4.2}$$

$$\mathbf{K} = \int dx' K_{mn}(x,x') h_n(x'), \quad K_{mn}(x,x') = \int dz \left(\frac{2}{\pi}\sqrt{1-z^2}\right) Y_m(z) \int dz' Y_n(z) V(x,z,x',z'). \tag{4.3}$$

In the previous definitions, the integral operators $\mathbf{B}$ and $\mathbf{K}$ are built in a matrix form like the ones at the end of the discussion in section 3.5, and a basis change is implicit in the z variable. Instead of the usual basis, where the vector elements coordinates indicate the value of the function at a discrete

point z_i, they are now the coefficients of a Chebyshev (of the second kind) polynomial expansion in z:

$$h(x,z) = \sum_n h_n(x) U_n(z) \Leftrightarrow h_n(x) = \int_{-1}^{1} dz \left(\frac{2}{\pi}\sqrt{1-z^2}\right) U_n(z) h(x,z), \tag{4.4}$$

$$\tag{4.5}$$

where $U_l(z)$ indicates the Chebyshev polynomial of degree l. The basis elements $Y_n(z)$ satisfy orthonormality relations

$$\int_{-1}^{1} dz \left(\frac{2}{\pi}\sqrt{1-z^2}\right) Y_m(z) Y_n(z) = \delta_{mn}. \tag{4.6}$$

The matrix $\mathbf{B}$ was inverted using the Crout algorithm with partial pivoting, as described in [57], and a regularization parameter $\epsilon\mathbb{1}$ was added to $\mathbf{B}$ before inversion, as discussed in [31, 32]. To confirm the quality of our implementation, we decided to replicate the plots of the longitudinal light-front distribution in figure 3 of [32]. The longitudinal light-front distribution $\Phi(z)$ in [31, 32] differs from our definition of the PDA (keeping in mind that $\alpha = -z$):

$$\text{PDA}: \quad \phi(\alpha) \propto \int dx \Psi_{LF}(x,\alpha), \qquad \text{LF dist.}: \quad \Phi(z) \propto \int dx \Psi^2_{LF}(x,z). \tag{4.7}$$

In the calculation of the light-front distributions, the weight function h was obtained by integration on a grid with $N_x = 40$ and $N_z = 30$. Three different values of $\frac{\mu}{m}$ were used, and four values of $\sqrt{t} \in \{0, 0.50i, 0.75i, 0.90i\}$ for each of them. The values were normalized by dividing by $\mathcal{I} = \frac{1}{2}\int_{-1}^{1} \Phi(z) dz$.

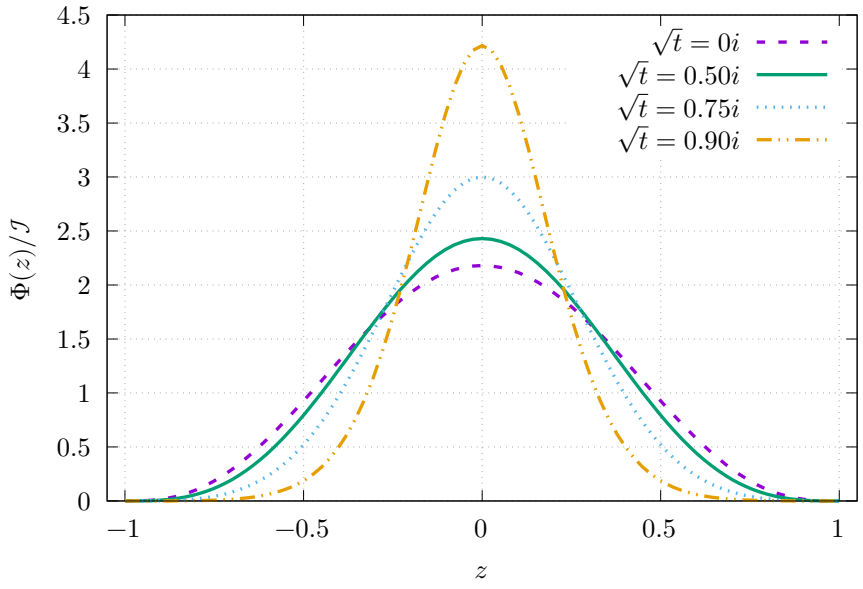

Figure 4.1: Numerical result for the light-front distribution, using our implementation of the Nakanishi method, for $\frac{\mu}{m} = 0.05$.

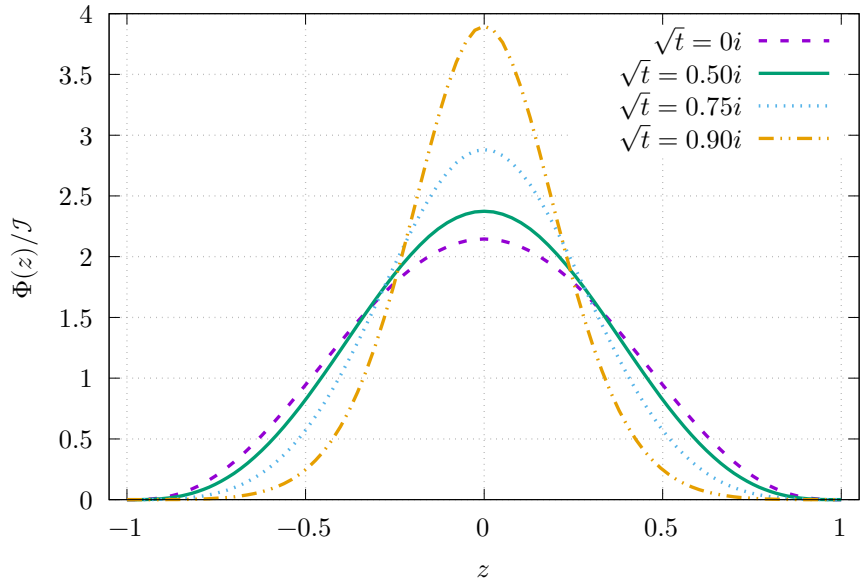

Figure 4.2: Numerical result for the light-front distribution, using our implementation of the Nakanishi method, for $\frac{\mu}{m} = 0.15$.

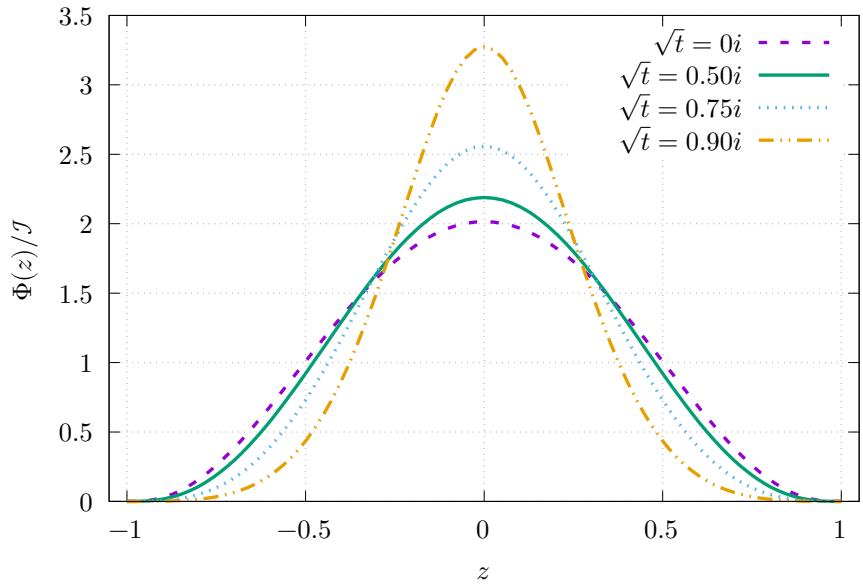

Figure 4.3: Numerical result for the light-front distribution, using our implementation of the Nakanishi method, for $\frac{\mu}{m} = 0.50$.

The obtained curves are a perfect match to the plots in figure 3 of [32]. This establishes our implementation of the Nakanishi method as a useful tool for comparison with the following solutions from the contour deformation method.

The curves in figures 4.1 to 4.3 show the generic features that are expected of the light-front distribution function, and the light-front wave function, in its z dependence (α in our defintions in sections 3.2), which are: even parity in z, which is the result of the symmetry of (3.25) and vanishing values at the end points, as the probability that one particle carries most of the fraction of the momentum is smaller than the average case of $z = 0$.

4.2 Bethe-Salpeter Amplitude

4.2.1 Amplitude and eigenvalues

The first result to be obtained via the contour deformation method, and also the first step in the calculation of the light-front wave function, is the Bethe-Salpeter amplitude ψ which is related to the Bethe-Salpeter wavefunction Ψ by $\Psi = G_0\psi$.

To obtain the Bethe-Salpeter amplitude it is necessary to solve the equation (3.34) numerically. For that, the integration in $\sqrt{x'}$ and ω' was written in a matrix form, like (3.78), and applied to a vector Ψ, using the power method to get the first eigenvector and eigenvalue, starting from an initial guess $\Psi = 1$.

As hinted in section 3.4.2.2, particularly in figure 3.3, one can see that for values of $\beta = \frac{\mu}{m} \to 0$, the cuts get closer to the point $\sqrt{x}$. The pratical effect is that, for $\beta \to 0$, an increasing amount of points in the integration in $\sqrt{x'}$ is needed to get a good numerical output. For that reason, a large value of $\beta = 4$ is used so that smaller number of points N_x and N_ω can be used.

The parameters used in the following were $N_x = 96$, $N_\omega = 95$ and $\beta = 4$. In (3.34), α is taken as an external parameter, so it is necessary to solve the BSE for each value of α. The number of points in α was selected to be $N_\alpha = 36$ — note that because α is external, this value does not have implications on the convergence of the BSE, altough, naturally, a larger N_α will reveal more details in the α dependence, but at the cost of increased computation time. The values of α were defined to be the roots of the N_α-th order Legendre polynomial, because these points will be useful to do integrations in α if needed.

The path in $\sqrt{x'}$ used was the one indicated in section 3.4.3, composed of the three parts (3.56), (3.57) and (3.62). The N_x integration points in $\sqrt{x'}$ are evenly split among the three path components.

Three values of $\sqrt{t}$ will be used. These were selected by the following criteria: one that does not require contour deformation, $\sqrt{t} = 0.20 + 0.20i$; one that requires contour deformations, but is below the threshold $M^2 = 4m^2$, $\sqrt{t} = 0.20 + 0.80i$; and finally, one above the threshold $\sqrt{t} = 0.20 + 1.20i$.

Figure 4.4 is the inverse eigenvalue $1/\lambda$ obtained from the solution of the BSE, as a function of α.

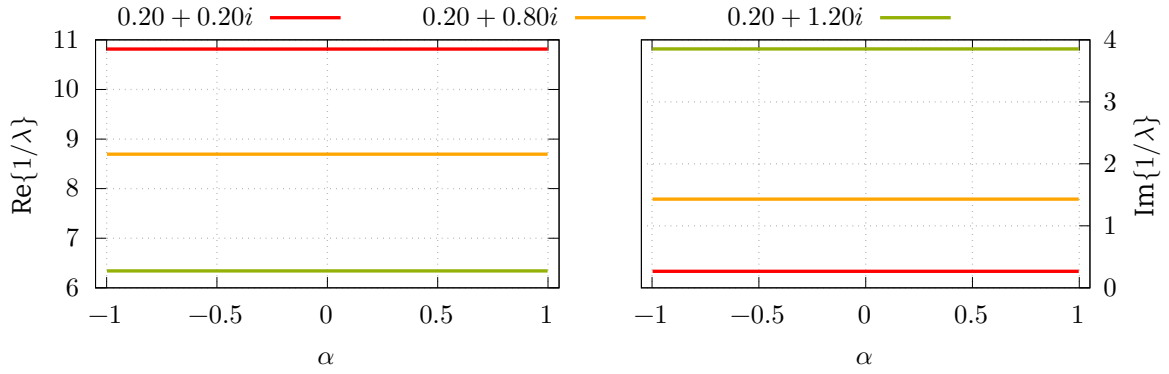

Figure 4.4: Inverse eigenvalues $1/\lambda$ as a function of α, for three values of $\sqrt{t}$: $0.20 + 0.20i$,$0.20 + 0.80i$, $0.20 + 1.20i$.

One can see that the eigenvalue is constant in α. This is the expected behavior as the mass of the bound state - which is determined by the eigenvalue - should not depend on the internal distribution of momentum between the interacting constituents.

The evaluation path of the Bethe-Salpeter amplitude in the variable $\sqrt{x}$ in the equation is the same as the integration path in $\sqrt{x'}$. If contour deformations are needed, then the result of the BSE will also only be known along that path. For that reason, the results that used contour deformations were analytically continued to the real x axis, using the Schlessinger method of section 3.5.1. This was done

by using as input 24 points in the path of x' for each value of ω' and the output points are the roots of the N_x-th order Legendre polynomial, mapped to $[0, \infty)$ by (3.72) - that is, the integration path for the case where contour deformations are not needed.

Figure 4.5 presents an overview of the result obtained for the Bethe-Salpeter amplitude. It is however also instructive to look at some particular values of the arguments. For that, in figure 4.6, for the real and imaginary part of the amplitude ψ, a plot of the α dependency for nine combinations of three values in x and ω is presented. Three values in x are selected: one in the low-momentum region, $x_1 \approx 0.94$, one in the mid-momentum region, at $x_2 \approx 11$ and finally one in the ultraviolet region at $x_3 \approx 101$. The selected values of ω were $\omega_1 = -0.5$, $\omega_2 = 0$ and $\omega_3 = -0.5$. The selected points are indicated by blue crosses in figure 4.5.

From figure 4.6 two observations can be made. The first is related to the particle exchange symmetry of (3.25), which, as can be seen in the plots, is realized in the numerical solution.

The second observation is that the Bethe-Salpeter amplitude varies slowly with the α parameter. A modest dependence on ω is also visible by comparing the values in the same row in 4.6, for the same value of α.

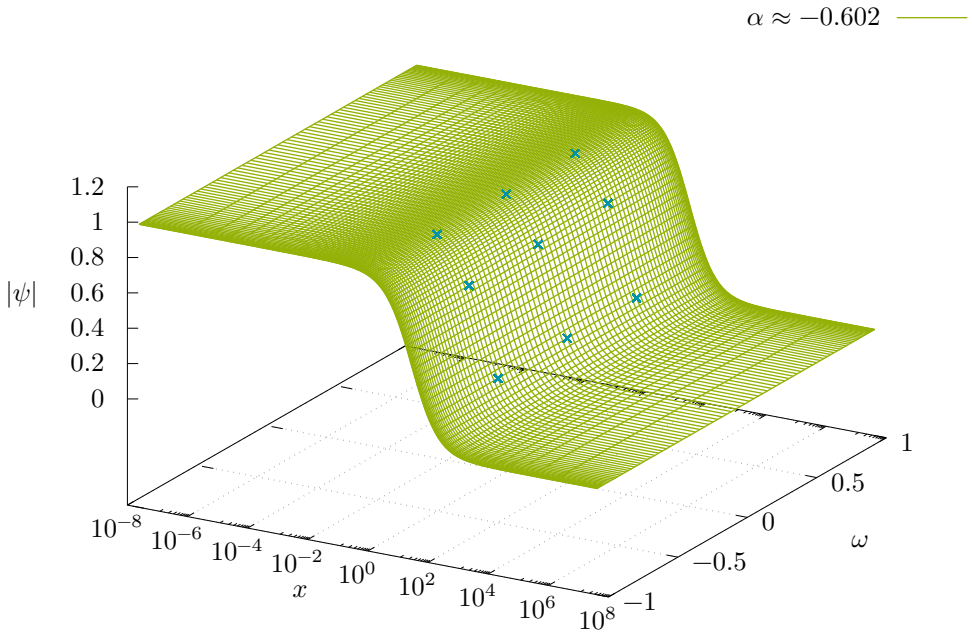

Figure 4.5: Absolute value of the Bethe-Salpeter amplitude $|\psi|$ as function of x and ω, for $\sqrt{t} = 0.20 + 0.20i$ and $\alpha = -0.602$. The blue crosses represent nine points of interest that are shown in more detail in the analysis below.

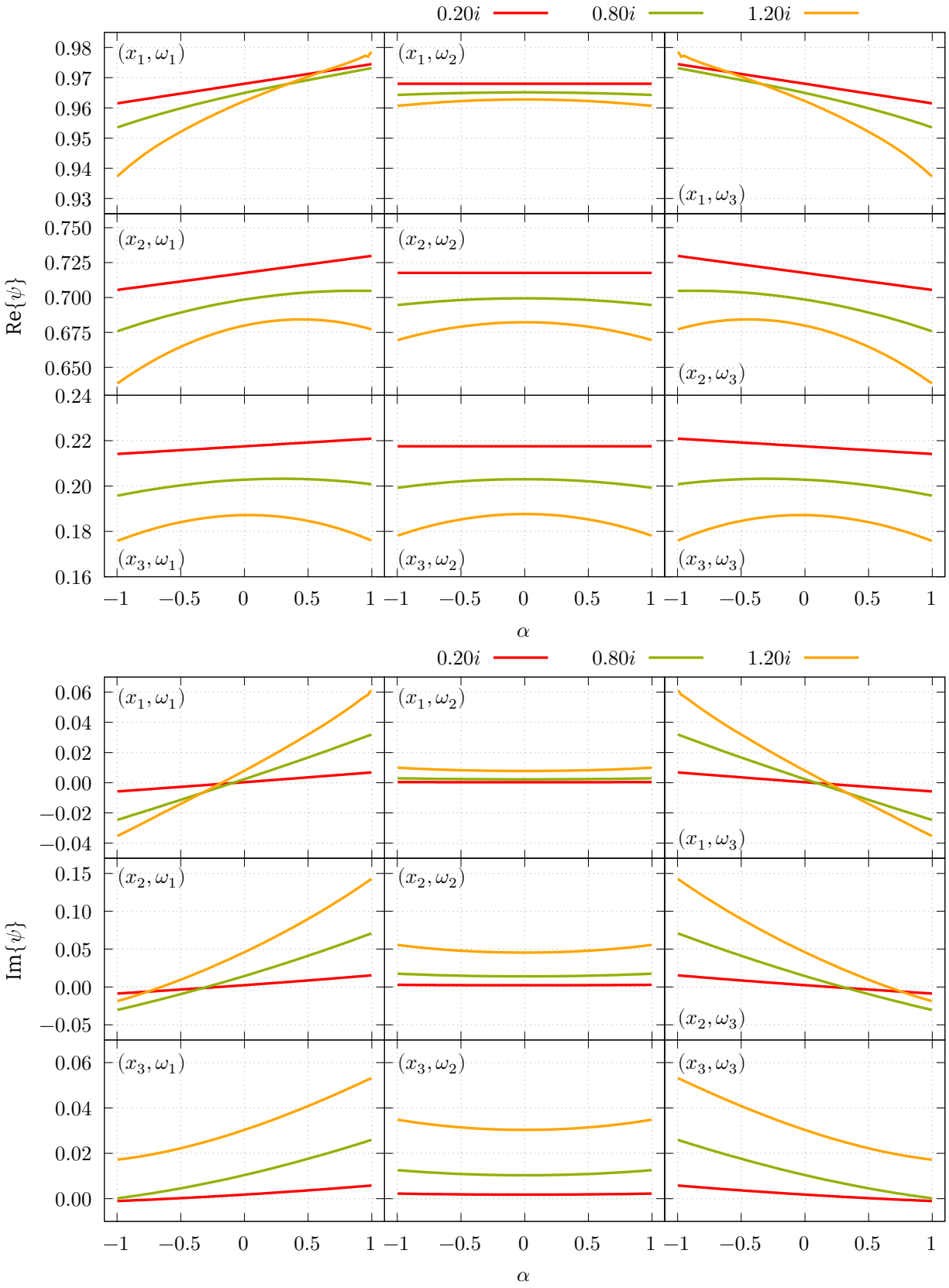

Figure 4.6: Real (top) and imaginary (bottom) parts of the Bethe-Salpeter amplitude as a function of α for nine points (x, ω) and $\mathrm{Re}\{\sqrt{t}\} = 0.2$ and three values of $\mathrm{Im}\{\sqrt{t}\}$.

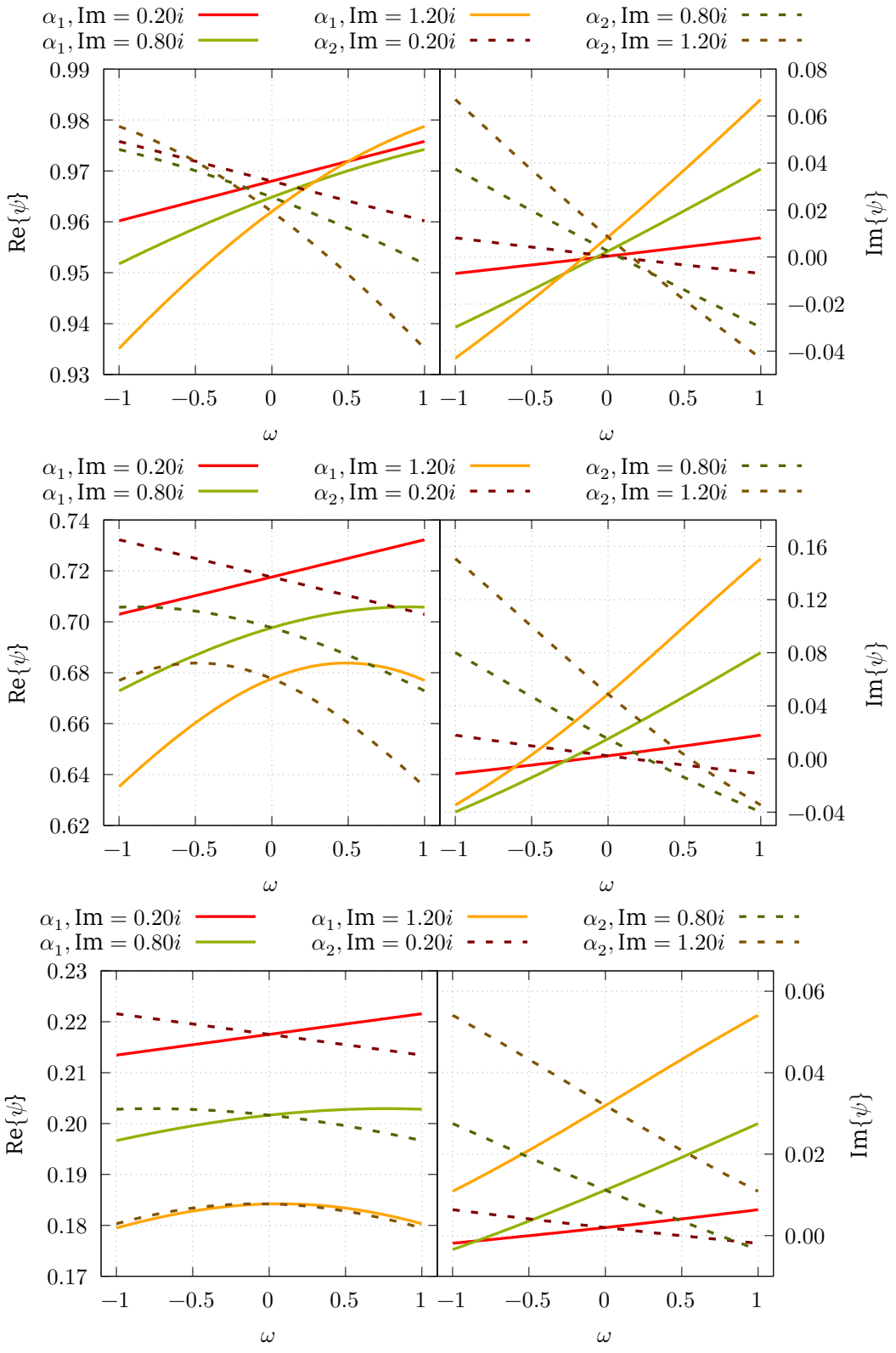

Figure 4.7: Real (left) and imaginary (right) parts of the Bethe-Salpeter amplitude for two fixed points in α, $\alpha_1 = -0.602$ and $\alpha_2 = 0.602$ and three fixed points in x: x_1 (top), x_2 (center) and x_3 (bottom). Three values of the imaginary part of $\sqrt{t}$ were chosen.

In the set of plots of figure 4.7, the dependence on the variable ω is studied, using the same values of x, and two values of $\alpha = \{-0.602, 0.602\}$. The solid colored curves correspond to the $\alpha = \alpha_1$ case

and the dashed grey curves are the $\alpha = \alpha_2$ case.

The dependence of ψ with x is displayed in figure 4.8. As the function is practically constant in ω and α, the plot shows a single value of $\omega = 0$ and $\alpha = -0.602$, and three values of $\sqrt{t}$. On the left plot of figure 4.8, the three curves are overlapped.

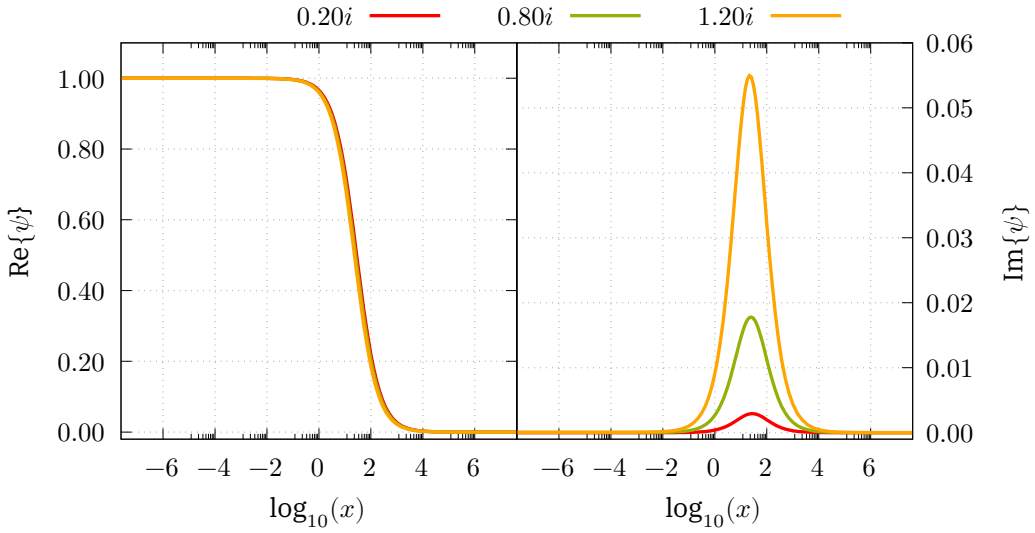

Figure 4.8: Real (left) and imaginary (right) parts of the Bethe-Salpeter amplitude ψ as a function of x, for fixed values of $\omega = 0$ and $\alpha = -0.602$ and three different imaginary parts of $\sqrt{t}$.

Comparing figure 4.8 with the plots showing the dependence of ψ in the variables α and ω, one can see that the variation in x dominates over the other two. The amplitude ψ is almost constant in both the large and small x limit, and it is in the intermediate regime where most of the variation occurs.

Because the BS eigenvalue depends on $\sqrt{t}$, one can furthermore obtain the eigenvalue spectrum numerically by varying $\sqrt{t}$. In figure 4.9 the eigenvalue spectrum is presented as a function of $\mathrm{Im}\{\sqrt{t}\}$, for six different values of $\mathrm{Re}\{\sqrt{t}\}$, using $N_x = 128$ and $N_\omega = 96$ to improve the numerics at the smaller values of $\mathrm{Re}\{\sqrt{t}\}$.

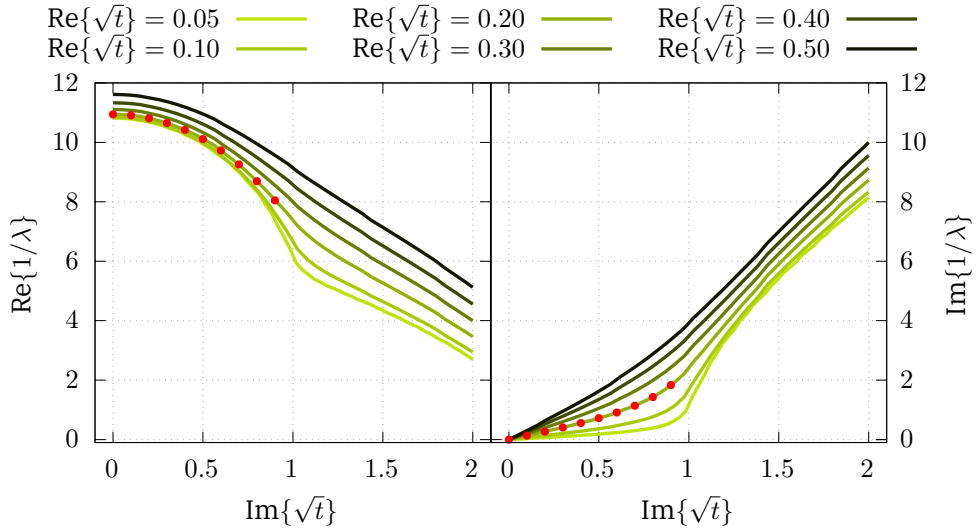

Figure 4.9: Real (left) and imaginary (right) parts of the inverse eigenvalue $1/\lambda$ of the Bethe-Salpeter equation, as a function of $\mathrm{Im}\{\sqrt{t}\}$ for different values of $\mathrm{Re}\{\sqrt{t}\}$. Overlayed, in red, are the results for $\mathrm{Re}\{\sqrt{t}\} = 0.20$ obtained via the Nakanishi method.

The results obtained via contour deformations are in excellent agreement with those obtained by the N method, as shown by the red dots in figure 4.9 (see also figure 11 of [33])

An exploration of the numerical stability of the solution of the BSE is presented in appendix C.

4.3 Light-Front wavefunctions and parton distribution amplitudes

After having obtained the results of the Bethe-Salpeter amplitude from its equation and established that the numerical method is sound and reproduces some results from the literature ([33]), one can now proceed to the next step and calculate the light-front wavefunctions using a numerical implementation of (3.66).

As a reminder, the needed ingredients for the computation of the light-front wavefunction are the propagators G_0, (which are known analytically), and the Bethe-Salpeter amplitude ψ which was calculated in the previous section 4.2 in the $\omega \in [-1, 1]$ region. For the LFWF it is necessary however to know the amplitude over the whole $\omega \in (-\infty, \infty)$ domain.

The analytic continuation of the amplitude to $\omega \in (-\infty, \infty)$, as discussed in section 3.4.4 is made using the Schlessinger method of section 3.5.1.

The following results were obtained with the amplitudes calculated in section 4.2.1, with $\beta = 4$, $N_x = N_\omega = 96$, $N_\alpha = 36$ and the same three values of $\mathrm{Im}\{\sqrt{t}\}$ as in section 4.2.1 for $\mathrm{Re}\{\sqrt{t}\} = 0.20$. The integration 3.66 is done with $N_\omega^{LF} = 500$ points. Note that these points are generated by the Schlessinger method, and each point requires almost no computational power to calculate, in contrast to the Bethe-Salpeter equation where each point in ω requires the solution of the integral equation for that point.

The light-front wavefunction is a function of x and α, and as such it is only known in the same points in x and α as the amplitude ψ. This implies that, when contour deformations are needed, the light-front wavefunction is evaluated along the integration path in $\sqrt{x}$, and not along $\sqrt{x} \in \mathbb{R}_0^+$. In a similar way as for the results of the amplitude, in those cases the Schlessinger method is used to extrapolate the obtained information to the real axis in $\sqrt{x}$.

Figure 4.10 shows the main features that are expected of the light-front wavefunctions. Firstly, it is symmetric in α. This is a manifestation of the particle exchange symmetry of (3.25). As the variable ω was integrated over, the only symmetry remaining is the one on α. Secondly, as discussed in section 2.5, the light-front wave functions have a probabilistic interpretation. They are proportional to the probability that the particles that form the bound state are found in the configuration (α, x). This indicates that configurations with lower values of x, which is proportional transverse momentum, are more likely than higher x configurations, whose probability tends to zero, as $x \to 0$, which allows for a finite integration along x [32]. The probabilistic view also explains the vanishing of the wavefunction at $\alpha = \pm 1$, as these configurations correspond to the particles having all of the total longitudinal momentum, which is not possible if the other particle has a non-zero mass.

In the following plots, the Nakanishi results from (3.16) are divided by $1 - \alpha^2$ so that they match the definition (3.66). The obtained light-front wavefunction is then normalized by imposing that:

$$\int dx \int d\alpha \; \Psi_{LF}^{contour}(x, \alpha) = 1 \tag{4.8}$$

This normalization is done in order to remove the prefactor introduced in equation (3.66) by the constant d and allowing comparison with the Nakanishi method.

Figure 4.12 shows the dependence in x of the calculated light-front wave function on x, for fixed points in α, while figure 4.11 shows the opposite case: the dependence on α for fixed values of x.

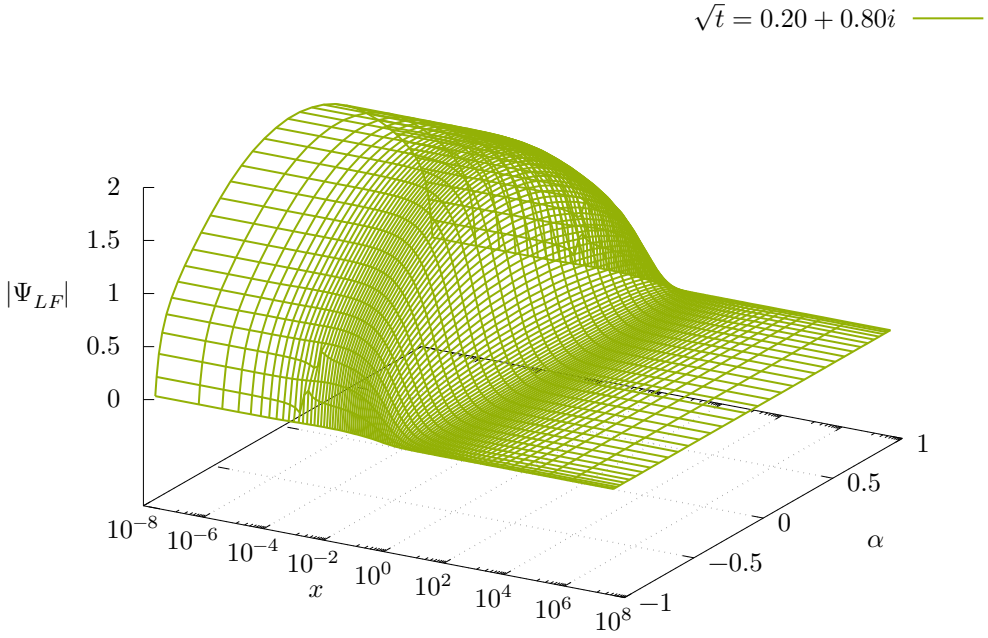

Figure 4.10: Absolute value of the obtained light-front wavefunction (not normalized) for $\beta = 4$ and $\sqrt{t} = 0.20 + 0.80i$.

The results show a very good agreement between the solutions obtained in the contour deformation method and the Nakanishi method. The low x region is where the most numerical complications are expected. Looking at the definition (3.66), and assuming that the light-front wave function is a finite constant $\mathcal{A}$ at $x \to 0$, equation (3.66) can be seen as a limit when $x \to 0$:

$$\widetilde{\Psi}_{LF} = \frac{2\sqrt{x}\sqrt{t}}{i\pi} \int_{-\infty}^{\infty} d\omega \, \Psi(x, \omega, \alpha, t) = \frac{2\sqrt{x}\sqrt{t}}{i\pi} \mathcal{I} \Rightarrow \mathcal{A} = \frac{2\sqrt{t}}{i\pi} \lim_{x \to 0} \sqrt{x}\mathcal{I} = 0 \cdot \lim_{x \to 0} \mathcal{I}, \tag{4.9}$$

which shows that $\mathcal{A}$ can only be finite if the limit of $\mathcal{I}$ diverges, generating a $0 \cdot \infty$ indeterminate form. The numerical method for the small x regions must strike a balance between the vanishing $\sqrt{x}$ term and the diverging integral.

Figure 4.11 reveals an interesting property of the light-front wavefunction for $\mathrm{Im}\{\sqrt{t}\} = 1$ as it shows that, instead of the single-peaked distributions of the other values of $\mathrm{Im}\{\sqrt{t}\}$ below the threshold, above the threshold, the single peak is transformed into two distinct peaks, which move away from the center $\alpha = 0$ to regions of higher $|\alpha|$, while still maintaining the particle exchange symmetry.

In both figures 4.12 and 4.11 there are no Nakanishi results for $\mathrm{Im}\{\sqrt{t}\} = 1.20$ because the Nakanishi method cannot go beyond the $\mathrm{Im}\{\sqrt{t}\} = 1.0$ threshold, as discussed in section 3.3.

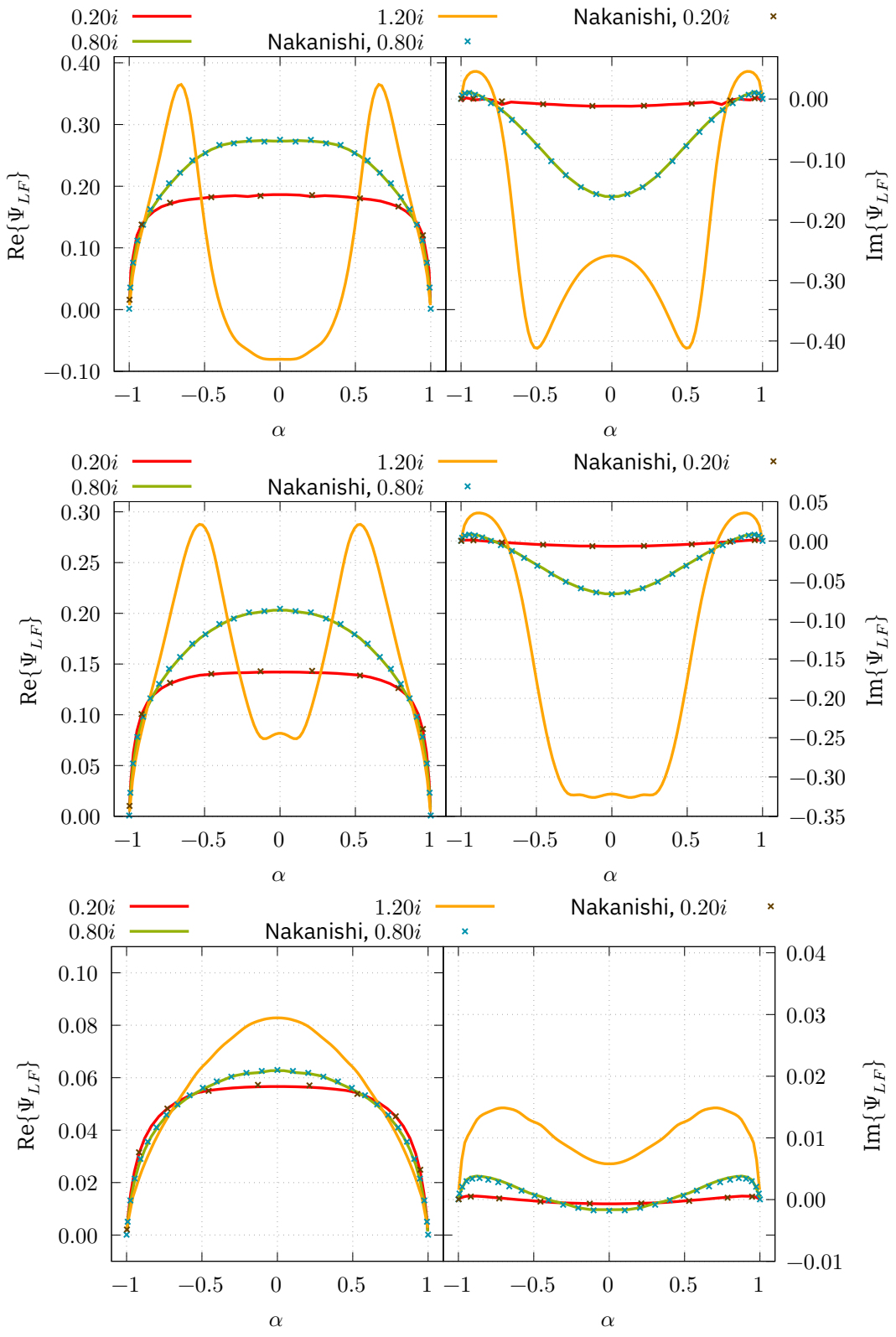

Figure 4.11: Dependence in α of the real (left) and imaginary (right) parts of the light-front wavefunction for $\mathrm{Re}\{\sqrt{t}\} = 0.20$ and three values of $\mathrm{Im}\{\sqrt{t}\}$, at three points in x: 0.039 (top), 0.326 (middle) and 2.05 (bottom).

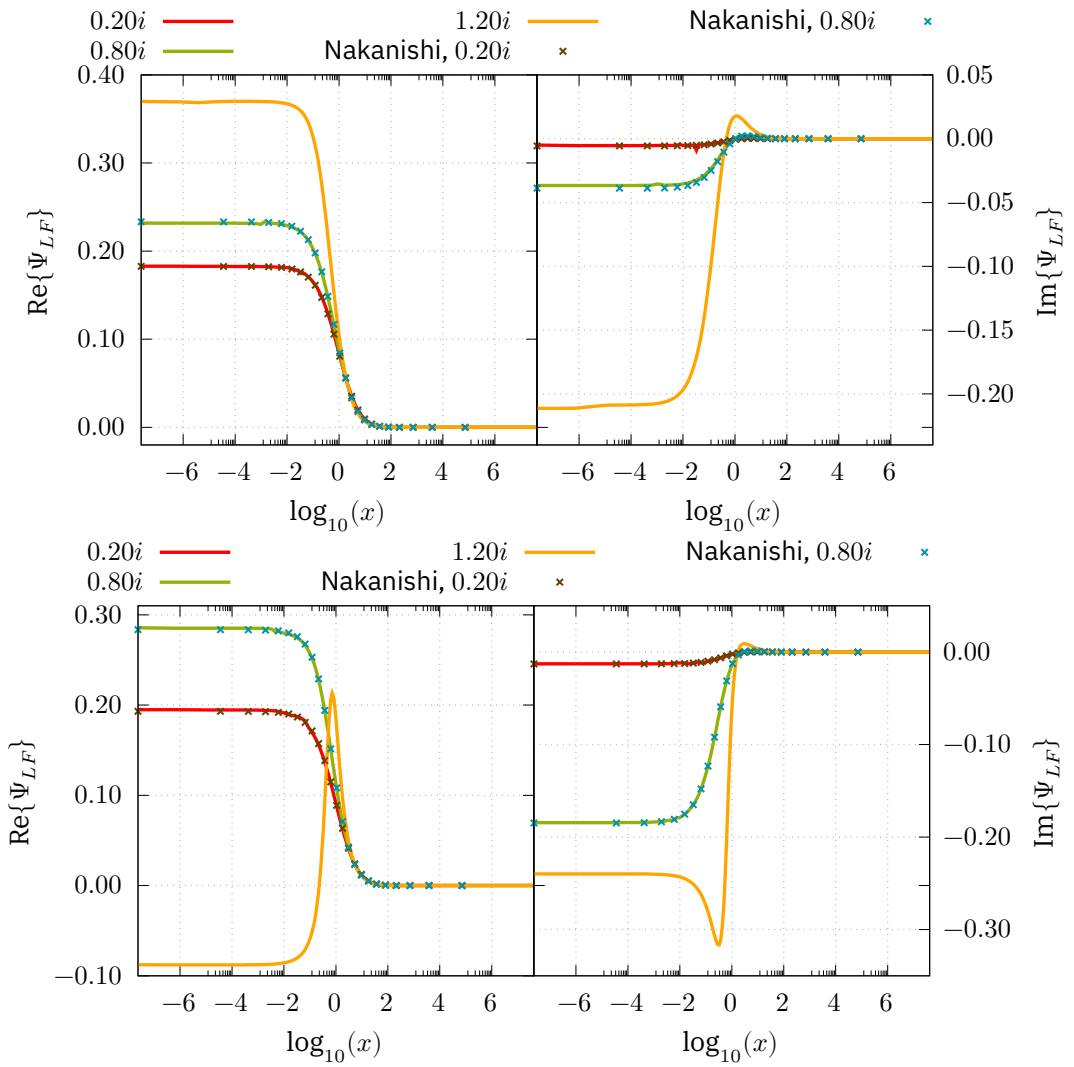

Figure 4.12: x dependence of the real (left) and imaginary (right) parts of the light-front wavefunction for $\mathrm{Re}\{\sqrt{t}\} = 0.20$ and three values of $\mathrm{Im}\{\sqrt{t}\}$ at two points in α: 0.668 (top) and 0.043 (bottom).

4.3.1 Parton distribution amplitudes

After having calculated the light-front wavefunction, the parton distribution amplitudes are obtained by integrating the light-front wavefunction in x.

These distribution amplitudes, which only depend on α, give the probability of finding the constituent particles in a kinematical configuration with a given value of α. The distributions carry the same properties in α as the original light-front wave functions.

A normalization condition, similar to the one used in the light-front wavefunction can be defined by imposing:

$$1 = \frac{1}{2}\int d\alpha\, \phi(\alpha). \tag{4.10}$$

The results for the parton distribution amplitudes from the previously calculated light-front wavefunctions are shown in figure 4.13. Once again, the contour deformation method is in good agreement with the results from the Nakanishi method.

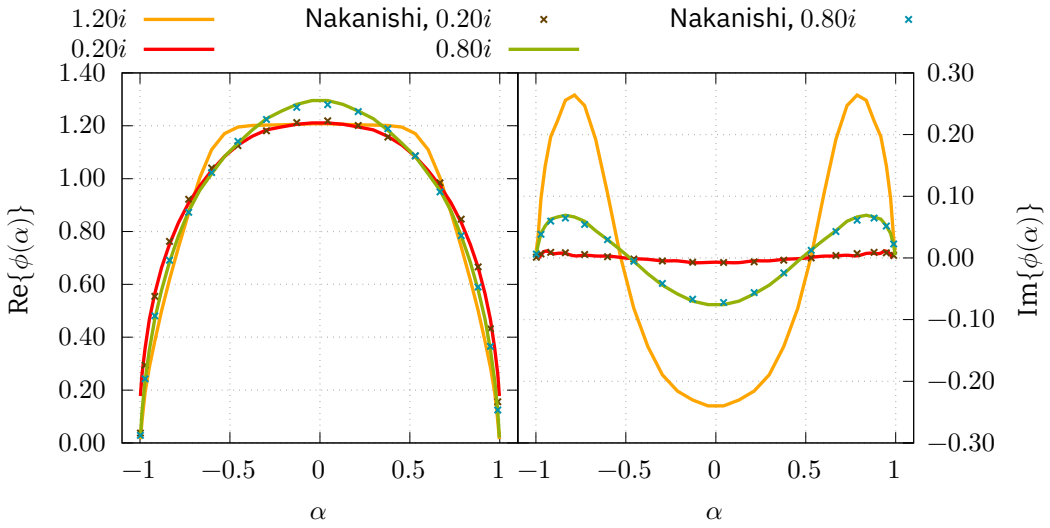

Figure 4.13: Parton distribution amplitude $\phi(\alpha)$, for three different values of $\mathrm{Im}\{\sqrt{t}\}$ and a fixed real part $\mathrm{Re}\{\sqrt{t}\} = 0.20$.

We further define a new set of quantities extracted from the PDA, the *Mellin moments*, in terms of the momentum fraction ξ:

$$\langle \xi^m \rangle = \int_0^1 d\xi\, \xi^m \phi(\xi) = \frac{1}{2} \int_{-1}^1 d\alpha \left(\frac{1+\alpha}{2} \right)^m \phi(\alpha). \tag{4.11}$$

The Mellin moments are used for the reconstruction of the PDFs and other hadronic distribution functions in both functional and lattice QCD calculations [59–61]. Equation (4.10) normalizes the PDA so that the zeroth moment $\langle \xi^0 \rangle$ is equal to 1. A list of the five calculated Mellin moments is given in table 4.1.

	$\langle \xi^0 \rangle$	$\langle \xi^1 \rangle$	$\langle \xi^2 \rangle$	$\langle \xi^3 \rangle$	$\langle \xi^4 \rangle$	$\langle \xi^5 \rangle$
$\mathrm{Im}\{\sqrt{t}\} = 0.20$	1	0.500	0.316	$0.223 + 0.001i$	$0.169 + 0.001i$	$0.134 + 0.001i$
$\mathrm{Im}\{\sqrt{t}\} = 0.80$	1	0.500	$0.311 + 0.003i$	$0.217 + 0.005i$	$0.162 + 0.006i$	$0.126 + 0.006i$
$\mathrm{Im}\{\sqrt{t}\} = 1.20$	1	0.500	$0.310 + 0.012i$	$0.216 + 0.018i$	$0.160 + 0.021i$	$0.125 + 0.021i$

Table 4.1: The first six Mellin moments of the parton distribution amplitudes, for three values of $\mathrm{Im}\{\sqrt{t}\}$ and a fixed value of $\mathrm{Re}\{\sqrt{t}\} = 0.20$, up to the third decimal place.

The zeroth Mellin moment in 4.1 is always 1 because of the normalization of the distribution amplitude. The first Mellin moment, $\langle \xi^1 \rangle$, is the mean value of ξ, in the distribution. The value $\langle \xi^1 \rangle = 0.5$ indicates that the distributions are centered around the $\xi = 0.5$ point, that is, $\alpha = 0$, as seen in figure 4.13

Chapter 5

Extensions of the Scalar Model

Having established the description of the contour deformations method in chapter 3 and confirmed that it provides results in agreement with other methods in the literature, some extensions to the scalar model of section 3.2 will now be considered to help bridge the gap towards QCD.

Two modifications will be made and analyzed separately. The first is the generalisation to different constituent masses so that one can be heavier than the other, as it is the case in a large number of mesons which are made of quarks with different masses [19].

The other is the inclusion of complex conjugate poles in the ϕ particle propagator. This will be important when using quark propagators calculated from a *rainbow-ladder* truncated Dyson-Schwinger equation, which typically produces complex conjugate poles [13].

5.1 Unequal masses

In section 3.2, a momentum partitioning parameter η was introduced in the definition of q:

$$q = k + (\xi + \eta)P = k + \left(\frac{\alpha - \varepsilon}{2}\right), \qquad \varepsilon = 2\eta - 1. \tag{5.1}$$

The parameter $\varepsilon \in [-1, 1]$ (or $\eta \in [0, 1]$) is arbitrary and should not affect the physical result, but will influence the position of the threshold $2m\sqrt{t} = iM$. For constituent masses m_1 and m_2, the optimal value of ε,

$$\varepsilon = \frac{m_1 - m_2}{m_1 + m_2} = \frac{m_1 - m_2}{2m}, \tag{5.2}$$

maximizes the calculable domain in $\sqrt{t}$, so that the threshold remains at $\mathrm{Im}\,\sqrt{t} = 1$ also for unequal masses. The scale m used in the scalar model in chapter 3 is defined as:

$$2m = m_1 + m_2. \tag{5.3}$$

So far, both the optimal ε parameter and the scale m are functions of the masses m_i. It is useful, however, to invert these relations. Forcing ε to take the optimal value of equation (5.2) and the scale m as in (5.3), one can write the masses m_i as functions of ε and m:

$$m_1 = (1 + \varepsilon)m, \qquad m_2 = (1 - \varepsilon)m, \qquad \frac{m_1}{m_2} = \frac{1 + \varepsilon}{1 - \varepsilon}. \tag{5.4}$$

The parameter $\varepsilon \in [-1, 1]$ controls the ratio between the masses. The limit $\varepsilon \to -1$ leads to $m_1 = 0$ and $m_2 = \infty$, and vice-versa for $\varepsilon \to 1$. If $\varepsilon < 0$, then m_2 is the more massive particle, and for $\varepsilon > 0$,

m_1 is the heavier one. The equal mass results are recovered for $\varepsilon = 0$, providing a good test for the calculated results. The variable m can be handled just like in the equal mass case and be taken out of the calculations, so that it sets the scale.

Using the definitions of equations (3.13) and (3.14), and the kinematics of (3.22), the propagator product G_0 can be written as:

$$\begin{aligned} m^4 G_0(x,\omega,t,\alpha,\varepsilon) &= \frac{m^2}{q_1^2+m_1^2}\frac{m^2}{q_2^2+m_2^2} = \\ &= \frac{m^2}{\left(k^2+(1+\alpha)^2\frac{P^2}{4}+(1+\alpha)k\cdot P+m_1^2\right)}\frac{m^2}{\left(k^2+(1-\alpha)^2\frac{P^2}{4}-(1-\alpha)\,k\cdot P+m_2^2\right)}. \end{aligned} \tag{5.5}$$

Note that the parts of the denominators relating to q_1^2 and q_2^2 are identical to the equal mass system, in (3.26). The ε parameter only comes in the definitions of m_1^2 and m_2^2. This is the manifestation of the statement that the momentum partition variable should not be physically observable.

Again, using the Lorentz invariants of equation (3.23),

$$x = \frac{k^2}{m^2}, \qquad \omega = \hat{k}\cdot\hat{P}, \qquad t = \frac{P^2}{4m^2} = -\frac{M^2}{4m^2}, \tag{5.6}$$

the propagator product G_0 becomes:

$$\begin{aligned} m^4 G_0(x,\omega,t,\alpha,\varepsilon) &= \\ &= \frac{1}{\left(x+(1+\alpha)^2 t+2(1+\alpha)\omega\sqrt{x}\sqrt{t}+(1+\varepsilon)^2\right)}\frac{1}{\left(x+(1-\alpha)^2 t-2(1-\alpha)\omega\sqrt{x}\sqrt{t}+(1-\varepsilon)^2\right)}. \end{aligned} \tag{5.7}$$

Simplifying further leads to an expression similar to (3.28):

$$m^4 G_0(x,\omega,t,\alpha,\varepsilon) = \frac{1}{\left(x+1+t+\alpha^2 t+2\alpha\omega\sqrt{x}\sqrt{t}+\varepsilon^2\right)^2-4\left(\alpha t+\sqrt{x}\sqrt{t}\omega+\varepsilon\right)^2}. \tag{5.8}$$

Note that the equal mass expression is recovered when $\varepsilon = 0$, as expected.

The propagator has two poles in ω, labeled $\omega_\pm^\varepsilon$, whose anayltical expressions are:

$$\omega_+^\varepsilon = -\frac{x+(1+\varepsilon)^2+(1+\alpha)^2 t}{2(1+\alpha)\sqrt{x}\sqrt{t}}, \qquad \omega_-^\varepsilon = \frac{x+(1-\varepsilon)^2+(1-\alpha)^2 t}{2(1-\alpha)\sqrt{x}\sqrt{t}}. \tag{5.9}$$

After the integration in ω', they will generate cuts in the $\sqrt{x}$ plane, just like in the equal masses case, however with the additional parameter ε. The cuts in $\sqrt{x}$, can, again, be parametrized by the functions $\sqrt{x}_\chi^\lambda$, which depend on the variable $\omega \in [-1,1]$, and with $\chi = \pm$ and $\lambda = \pm$:

$$\sqrt{x}_\chi^\lambda = A(\chi,\alpha)\left[\sqrt{t}\omega + i\lambda\sqrt{t(1-\omega^2)+\left(\frac{1+\chi\varepsilon}{1+\chi\alpha}\right)^2}\right], \qquad A(\chi,\alpha) = \begin{cases} -(1+\alpha), & \chi = + \\ (1-\alpha), & \chi = - \end{cases}. \tag{5.10}$$

This again reduces to the equal masses curves for $\varepsilon = 0$. These cuts have exactly the form of equation (A.2), with a C variable of the form:

$$C = i\sqrt{1+\frac{\kappa^2}{\tau}}, \qquad \kappa^2 = (1+\chi\varepsilon)^2, \qquad \tau = A(\chi,\alpha)^2 t, \tag{5.11}$$

where $\kappa^2 \in [0,2]$, for $\varepsilon \in [-1,1]$.

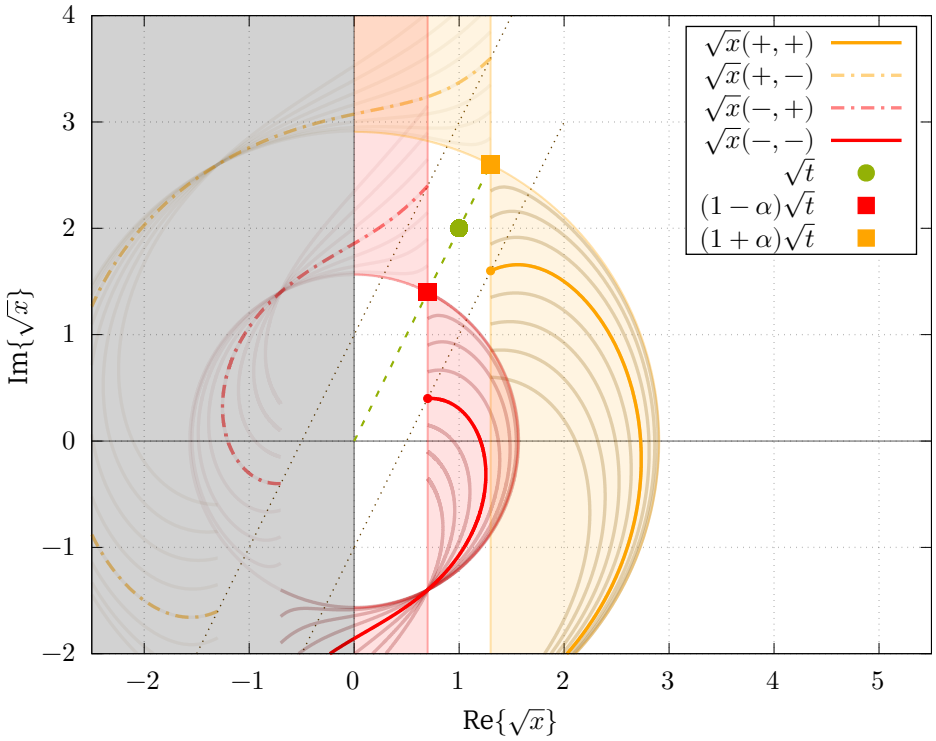

Figure 5.1: Branch cuts $\sqrt{x}^{\lambda}_{\chi} \equiv \sqrt{x}(\chi,\lambda)$ of G_0 in the complex $\sqrt{x}$ plane, for $\alpha = 0.3$ and $\sqrt{t} = 1 + 2i$. The shaded areas indicate the regions of the $\sqrt{x}$ plane where there might be branch cuts, as the value of ϵ varies. The faint dark colored lines near the cuts represent the configurations for different values of $\epsilon \in [-1, 1]$.

The contours in section 3.4.3 were designed to avoid the cuts for any $\kappa^2 > 0$, therefore they will also be valid for this case, as can be seen in figure 5.1.

Looking at equation (5.1), with q' being the loop momentum, one finds

$$q - q' = k - k', \tag{5.12}$$

like in the equal masses case. As the vectors k and k' do not depend on the momentum partitioning parameter ε in their definition, $k - k'$ is the same as in the equal mass case.

This behavior is expected, because the kernel should depend only on the transferred momentum by the exchanged χ particle, which, of course, is independent of the mass of the interacting particles.

The interaction kernel does not change with the introduction of unequal masses, and the integration path in $\sqrt{x'}$ for the equal masses can also accommodate the alterations in the propagator cuts, so the integration path for the equal masses case can also be used in this problem, with no modification.

The BSE to solve is the same as in the equal mass case, just with the added ε parameter in the propagators G_0:

$$\begin{aligned}&\psi(x,\omega,t,\alpha,\varepsilon) = \\ &= \frac{g^2}{m^2}\frac{1}{(2\pi)^3}\frac{1}{2}\int_0^\infty dx' x' \int_{-1}^{1} d\omega' \sqrt{1-\omega'^2} G_0(x',\omega',t,\alpha,\varepsilon) \int_{-1}^{1} dy K(x,\omega,x',\omega',y)\psi(x',\omega',t,\alpha).\end{aligned} \tag{5.13}$$

Note that the particle exchange symmetry of equation (3.25) is explicitly broken by the introduction of the ε parameter, as it is now possible to distinguish the interacting particles by their mass. The result is that the amplitude is no longer symmetric for transformations like (3.25), and both the light-front

wave function and the parton distribution function are no longer even in α.

The light-front wave function and the parton distribution amplitudes now have a maximum at $\alpha \neq 0$. If the heavier particle is m_1, then the maximum is at $\alpha > 0$, and if m_2 is the heavier, then the maximum is at $\alpha < 0$, which reflects the fact that, on average, the heavier particle has a higher fraction of the total momentum.

Figure 5.2 are shows the inverse eigenvalues obtained by the contour deformation method, for five different values of ε, $\beta = 4$ and $\sqrt{t} = 0.2 + 0.8i$. As in the case of section 4.2.1, the eigenvalues do not change with α, but do have a dependence in ε. Note that ε is no longer the momentum partitioning parameter but now sets the mass ratio between the particles, influencing the physical outcome.

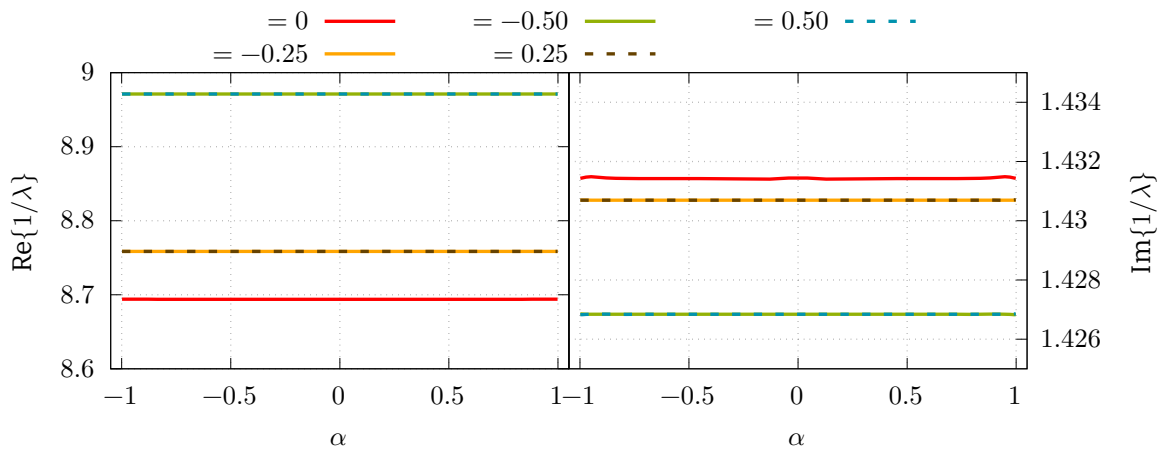

Figure 5.2: Inverse eigenvalues $1/\lambda$ for five values of ε.

The obtained eigenvalues are even in ε. This is the manifestation of a *new* version of the particle exchange symmetry of (3.25). The only distinguishing characteristic of the particles is their mass. It is not relevant to know which particle has the larger mass, just that there is a mass difference, which remains the same under $\varepsilon \to -\varepsilon$.

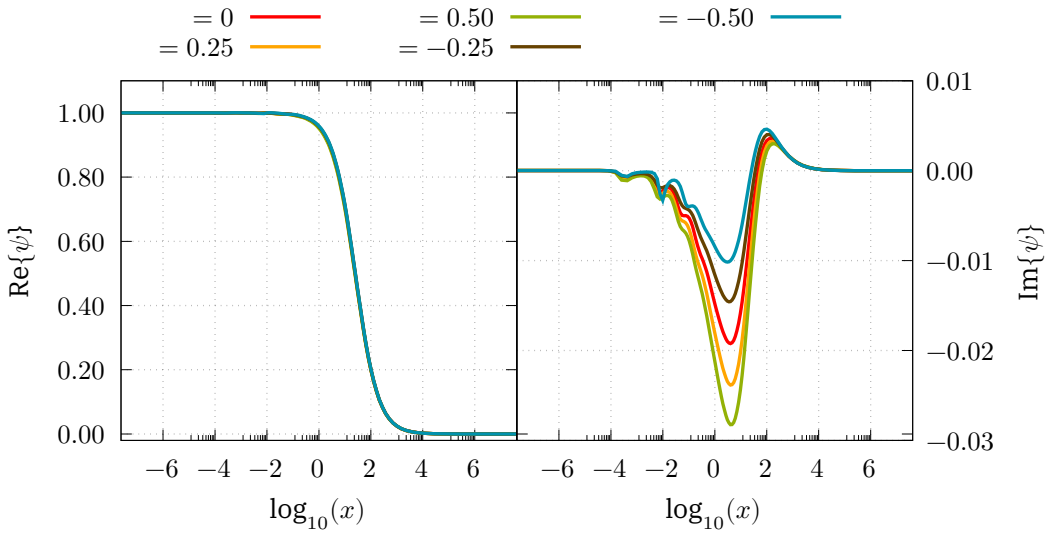

Figure 5.3: x dependence of the Bethe-Salpeter amplitude ψ for five values of ε.

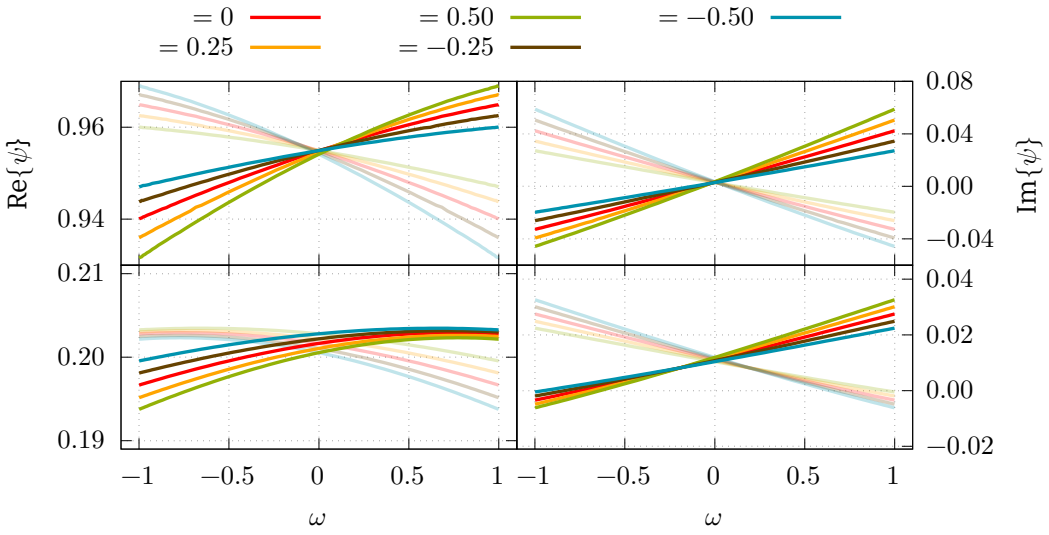

Figure 5.4: ω dependence of the amplitude ψ for five different values of ε. Two points in x were used: $x = 1.22$ (top) and $x = 101.5$ (bottom). The solid lines are for $\alpha = -0.602$ and the faint lines are for $\alpha = 0.602$.

Figure 5.3 shows the x dependence of the Bethe-Salpeter amplitudes ψ for the same five values of ε, $\alpha = -0.602$ and $\omega = -0.512$. Although the real part of ψ does not change appreciably — the curves on the left plot in 5.3 are all overlapped — the imaginary part shows a clear difference for each value of ε. Figure 5.3 also hints at possible interesting behaviour in the ω variable. Figure 5.4 shows the ω dependence for $\alpha = -0.602$ and two values of x. The particle exchange symmetry has now an extra element:

$$\alpha \to -\alpha, \qquad \varepsilon \to -\varepsilon, \qquad \omega \to -\omega. \tag{5.14}$$

From the calculated amplitudes, the LFWFs and subsequently the PDAs were extracted. Using the same normalizations of section 4.3, the light-front wavefunctions are shown in figure 5.5, for the α dependence, and in figure 5.6, for the x dependence.

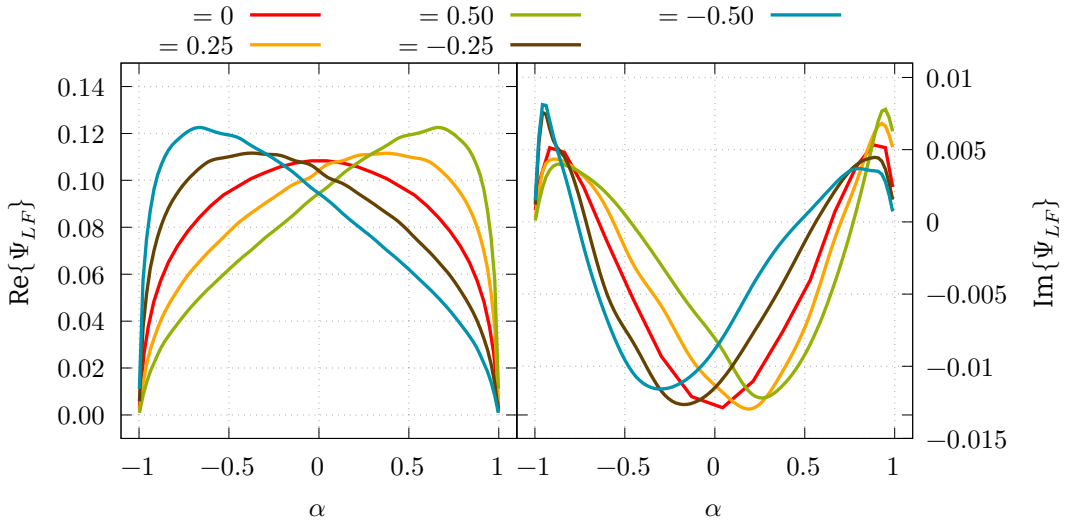

Figure 5.5: Dependence of the light-front wavefunction Ψ_{LF} on α, for five different values of ε.

Figure 5.5 illustrates the defining feature of the unequal mass system: the light-front wavefunction, and subsequently, the parton distribution amplitude are no longer centered at $\alpha = 0$, but are instead skewed to one side, towards $\alpha > 0$ for $\varepsilon > 0$, or towards $\alpha < 0$ if $\varepsilon < 0$. The peak, therefore, follows the heavier particle.

On the other hand, the dependence in x is similar to the one of chapter 4, as seen in figure 5.6.

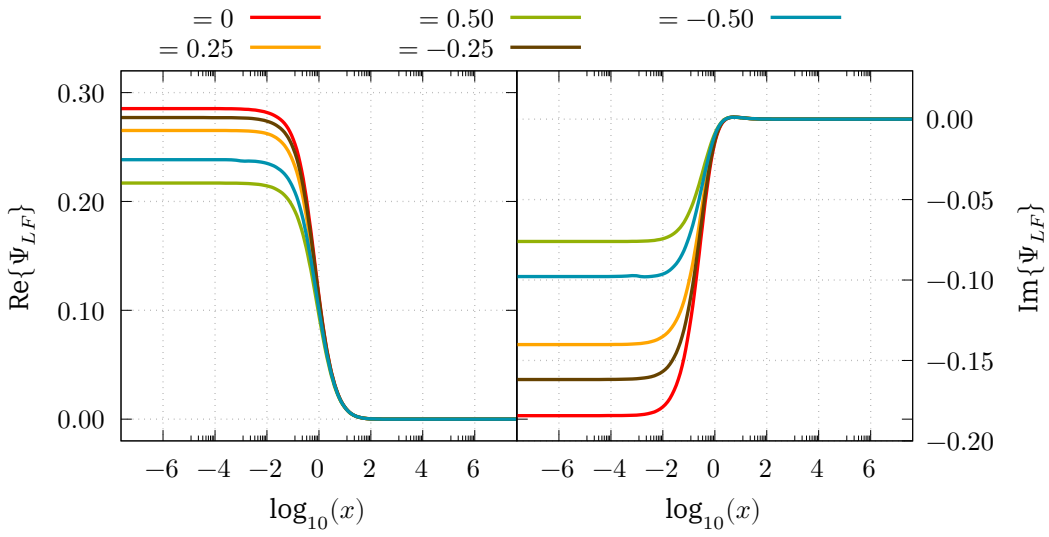

Figure 5.6: Dependence on x of the light-front wavefunction, Ψ_{LF}, for five different values of ε.

Finally, the parton distribution amplitudes $\phi(\alpha)$, which exhibit the same features in their α dependence as the light-front wavefunction, are shown in figure 5.7.

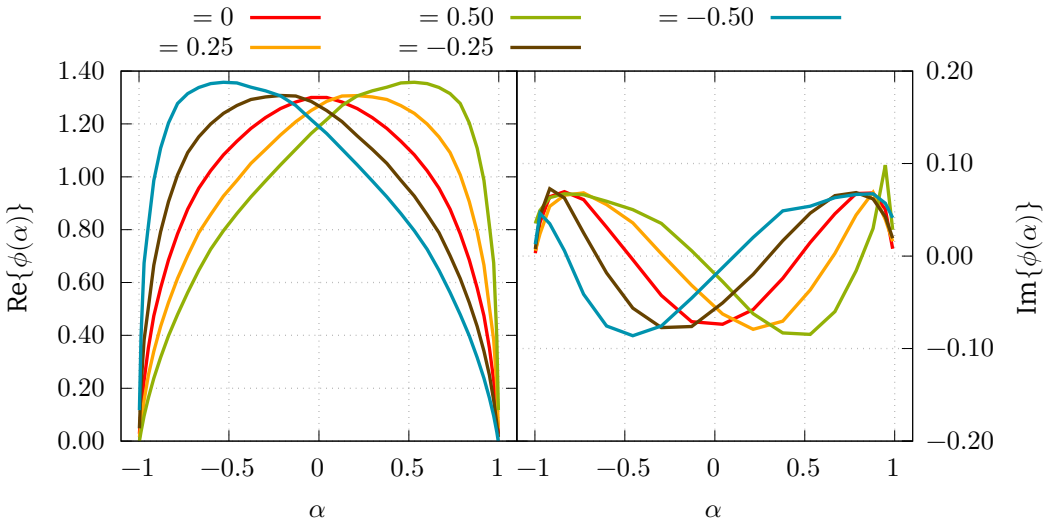

Figure 5.7: Parton distribution amplitudes $\phi(\alpha)$ for five different values of ε.

5.2 Complex conjugate poles

The other useful extension of the scalar model in section 3.2 is the inclusion of complex conjugate poles in the ϕ particle propagators $D_\phi(q)$:

$$D_\phi(q) = \frac{1}{q^2 + m^2} \longrightarrow \frac{1}{2}\left(\frac{1}{q^2 + m^2} + \frac{1}{q^2 + (m^*)^2}\right). \tag{5.15}$$

Although this study will focus on a single pair of complex conjugate poles, it is possible to introduce more pairs.

In equation (5.15) the squared mass m^2 is a complex number. In what follows, the masses are parametrized as:

$$m^2 \to m^2(1 + i\delta). \tag{5.16}$$

The parameter m^2 sets the absolute value of the complex number and $\delta \in \mathbb{R}$ controls the ratio between the imaginary and real parts. The variable δ in this case is unbounded, that is, it can take any value in $(-\infty, \infty)$, and the limit $\delta = 0$ recovers the real masses case. There is a natural symmetry in respect to the $\delta \to -\delta$ transformation, as it is equivalent to the conjugation operation applied on the masses, and the propagator (5.15) includes the complex conjugate pair of masses. Therefore, the δ case is the same as the $-\delta$ case.

Just as in the unequal masses case of the previous section, the kernel is not affected by this modification, as again, it is independent of the mass of the interacting particles. The discussion of section 3.4.2.2 still applies in this case.

Writing the product of the propagators G_0 is somewhat more involved than for the real mass case, because each single particle propagator is now the sum of two terms. For simplicity, we only consider the case where both interacting particles have the same complex mass $m^2(1 + i\delta)$; nevertheless, it is also possible to add a second complex mass by introducing another δ parameter and another absolute value.

Before deriving the full expression for G_0, it is helpful to simplify the expressions for the single-particle propagators:

$$D_\phi(q) = \frac{1}{2}\left(\frac{1}{q^2 + m^2(1 + i\delta)} + \frac{1}{q^2 + m^2(1 - i\delta)}\right) = \frac{q^2 + m^2}{(q^2 + m^2)^2 + \delta^2 m^4}. \tag{5.17}$$

Next, explicit expression for the product of the propagators, G_0, is written:

$$m^4 G_0(x, \omega, t, \alpha, \delta) = D_\phi(q_1^2) D_\phi(q_2^2) = m^4 \frac{A_1}{A_1^2 + \delta^2 m^4} \frac{A_2}{A_2^2 + \delta^2 m^4}, \tag{5.18}$$

$$A_1 = q_1^2 + m^2 = \left(k^2 + \frac{P^2}{4}(1 + \alpha)^2 + (1 + \alpha)k \cdot P + m^2\right), \tag{5.19}$$

$$A_2 = q_2^2 + m^2 = \left(k^2 + \frac{P^2}{4}(1 - \alpha)^2 - (1 - \alpha)k \cdot P + m^2\right). \tag{5.20}$$

The terms A_1 and A_2 can be expressed through the usual Lorentz invariants (equation (3.23)):

$$A_1 = m^2\left(x + t + 1 + \alpha^2 t + 2\alpha t + 2\omega\sqrt{x}\sqrt{t} + 2\alpha\omega\sqrt{x}\sqrt{t}\right), \tag{5.21}$$

$$A_2 = m^2\left(x + t + 1 + \alpha^2 t - 2\alpha t - 2\omega\sqrt{x}\sqrt{t} + 2\alpha\omega\sqrt{x}\sqrt{t}\right). \tag{5.22}$$

It is also be useful to write the results for A_1^2 and A_2^2:

$$\begin{aligned} A_1^2 &= \left(x+t+1+\alpha^2 t+2\alpha\omega\sqrt{x}\sqrt{t}\right)^2+4t\left(\alpha\sqrt{t}+\omega\sqrt{x}\right)^2 \\ &\quad +4\sqrt{t}\left(\alpha\sqrt{t}+\omega\sqrt{x}\right)\left(x+t+1+\alpha^2 t+2\alpha\omega\sqrt{x}\sqrt{t}\right) \\ &\quad \equiv \Gamma+\zeta, \end{aligned} \tag{5.23}$$

$$\begin{aligned} A_2^2 &= \left(x+t+1+\alpha^2 t+2\alpha\omega\sqrt{x}\sqrt{t}\right)^2+4t\left(\alpha\sqrt{t}+\omega\sqrt{x}\right)^2 \\ &\quad -4\sqrt{t}\left(\alpha\sqrt{t}+\omega\sqrt{x}\right)\left(x+t+1+\alpha^2 t+2\alpha\omega\sqrt{x}\sqrt{t}\right) \\ &\quad \equiv \Gamma-\zeta, \end{aligned} \tag{5.24}$$

thus defining the variables Γ and ζ, which will help in the construction of the full form of G_0 which after collecting the results of the A terms and simplifying (as much as possible) is written as:

$$m^4 G_0 = \left[\left(x+1+t+\alpha^2 t+2\alpha\omega\sqrt{x}\sqrt{t}\right)^2-4t\left(\alpha\sqrt{t}+\omega\sqrt{x}\right)^2\right]\frac{1}{\left(\Gamma+\delta^2\right)^2-\zeta^2}. \tag{5.25}$$

When both particles have the same complex mass, the particle exchange symmetry of (3.25) appears again, and it is expected that all physical quantities are invariant under the following combined transformation:

$$\alpha \to -\alpha, \qquad \omega \to -\omega. \tag{5.26}$$

The denominator of G_0 is of fourth power in ω and G_0 has now have four poles, labeled ω_χ^ν, with $\chi,\nu=\{+,-\}$:

$$\omega_+^\nu = -\frac{x+1+(1+\alpha)^2 t+i\nu\delta}{2(1+\alpha)\sqrt{x}\sqrt{t}}, \qquad \omega_-^\nu = \frac{x+1+(1-\alpha)^2 t+i\nu\delta}{2(1-\alpha)\sqrt{x}\sqrt{t}}. \tag{5.27}$$

As expected, for $\delta=0$, because $\omega_\chi^+=\omega_\chi^-$, the four singularities will reduce to just two, which are the singularities of equation (3.37) for the real masses case. The integration in ω during the solution of the Bethe-Salpeter equation produces, again, branch cuts in the $\sqrt{x}$ complex plane. However, instead of only four cuts, the complex conjugate case now has eight branch cuts, two for each pole in ω.

Labeling the cuts as $\sqrt{x}_\chi^{\{\lambda,\nu\}}$, where χ controls the sign of the α terms, λ distinguishes between the plus and minus solutions for each pole in ω, and ν controls the sign on δ terms, it is possible to write the branch cuts in a similar form as equations (3.41) to (3.38):

$$\sqrt{x}_\chi^{\{\lambda,\nu\}} = A(\chi,\alpha)\left[\sqrt{t}\omega+i\lambda\sqrt{t(1-\omega^2)+\frac{1+\nu i\delta}{(1+\chi\alpha)^2}}\right], \quad A(\chi,\alpha)=\begin{cases}-(1+\alpha), & \chi=+\\ (1-\alpha), & \chi=-\end{cases}. \tag{5.28}$$

Equation (5.28) marks the point where the complex conjugate poles case diverges fundamentally from the real masses case. Even though these cuts appear to have the same functional form as the ones in section 3.4.2.1, the difference becomes clear when written in the variables of appendix A. Specifically, the variable C becomes:

$$C = i\sqrt{1+\frac{\kappa^2}{t(1+\chi\alpha)^2}}, \qquad \kappa^2=(1+\nu i\delta)\in\mathbb{C}. \tag{5.29}$$

In contrast to the previous cases, the parameter κ^2 is no longer a real number. The practical consequence is that the cuts are rotated when $\delta\neq 0$, with the $+i\delta$ and the $-i\delta$ curves rotating in opposite

directions, which implies that, for values of $\delta > \delta_{crit}$, the cuts cross each other and the contour deformation procedure is no longer possible.

The following analysis is based on the discussion at the end of appendix A, but generalized for $\kappa^2 \in \mathbb{C}$. The first step is to define $\sqrt{\tau} = A(\chi, \alpha)\sqrt{t}$ and to write the end points $\omega = \pm 1$, for a cut with $\delta \neq 0$ and labels $\{\lambda, \nu\}$,

$$\begin{aligned} \omega = -1 \rightarrow \quad & \{+,+\} : -\sqrt{\tau} + i\kappa, & \{-,+\} : -\sqrt{\tau} - i\kappa, \\ & \{+,-\} : -\sqrt{\tau} + i\kappa^*, & \{-,-\} : -\sqrt{\tau} - i\kappa^*, \end{aligned} \tag{5.30}$$

$$\begin{aligned} \omega = 1 \rightarrow \quad & \{+,+\} : \sqrt{\tau} + i\kappa, & \{-,+\} : \sqrt{\tau} - i\kappa, \\ & \{+,-\} : \sqrt{\tau} + i\kappa^*, & \{-,-\} : \sqrt{\tau} - i\kappa^*. \end{aligned} \tag{5.31}$$

The line that connects the $\omega = 1$ and $\omega = -1$ end points for opposite values of λ which for $\kappa^2 \in \mathbb{R}$ was a vertical line in the $\sqrt{x}$ plane, is now rotated around the $\sqrt{t}$ point. More importantly, the points for the same ω and the opposite λ form two lines that meet at the origin, as in figure 5.8 which shows four sets of lines: four brown (for the $\chi = +$ case) and four grey (for the $\chi = -$ case), the solid lines are for $\nu = +$ and the dashed are for $\nu = -$.

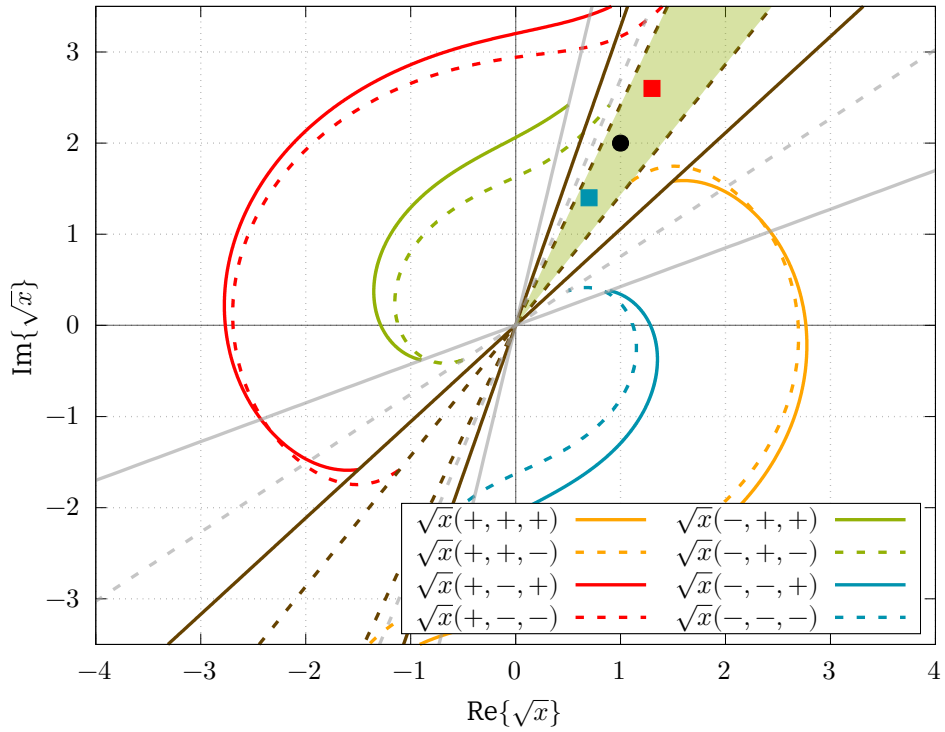

Figure 5.8: Propagator cuts $\sqrt{x}_{\chi}^{\{\lambda,\nu\}} = \sqrt{x}(\chi, \lambda, \nu)$ with complex conjugate mass poles. The used parameters were $\alpha = 0.3$, $\delta = 0.3$, $\sqrt{t} = 1.0 + 2.0i$.

These lines, for the $\nu = +$ case, rotate towards each other as the value of δ increases and vice-versa for the $\nu = -$ case. When the two lines meet, the cuts overlap, making it impossible to avoid crossing a cut. The safe region for δ, in the $\nu = +$ case is given by the following condition, and seen as the green shaded region in 5.8, bounded by the dahsed lines for the $\nu = +$ case:

$$\arg\left(\sqrt{\tau} - i\sqrt{1 + i\delta}\right) < \arg\left(\sqrt{\tau} + i\sqrt{1 + i\delta}\right), \tag{5.32}$$

which simplifies to:

$$\mathrm{Im}\{\sqrt{\tau}\} < \frac{\mathrm{Im}\{i\sqrt{1+i\delta}\}\,\mathrm{Re}\{\sqrt{\tau}\}}{\mathrm{Re}\{i\sqrt{1+i\delta}\}}. \tag{5.33}$$

Note that the condition for the $\nu = -$ case can be found by doing the transformation $\delta \to -\delta$ in equation (5.33). These correspond to the area bounded by solid brown lines in figure 5.8. The valid region for the solution of the Bethe-Salpeter amplitude is the intersection of the $\nu = +$ and $\nu = -$ conditions. This condition is also independent of α (and, by association, of χ as well), by the definition of $\sqrt{\tau}$.

The calculation of the LFWF has a small detail that needs to be taken into account, as the integration in ω is along the entire real axis. This implies that the cuts (5.28) are parametrized in $\omega \in (-\infty, \infty)$. The condition (5.33) (and the analogue for the $\nu = -$ case) still applies, as can be seen in figure 5.9. Figure 5.9 shows one of the cuts from figure 5.8 and the region determined by the condtions (5.28) for different values of δ.

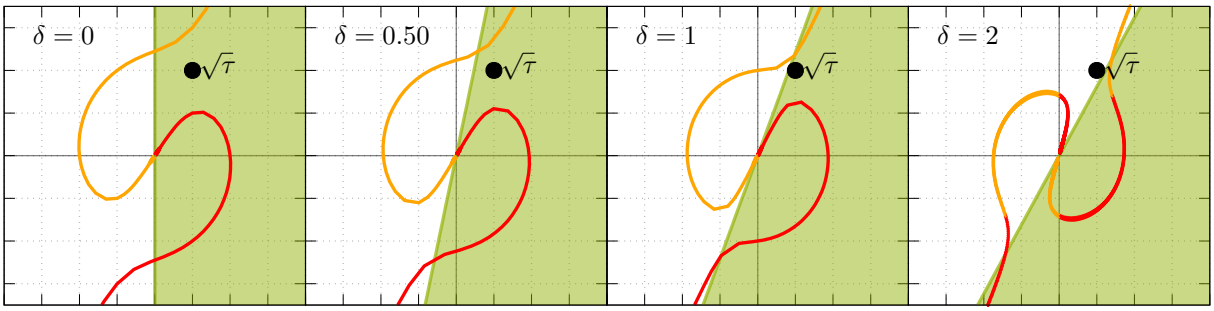

Figure 5.9: Schematic plot of the evolution of the cuts in $\sqrt{x}$ for various values of δ. If the point $\sqrt{\tau}$ is inside the green region, then a contour deformation is possible.

In the left three plots of figure 5.9 one can see that for increasing values of $|\delta|$, the cuts get closer to the integration path that goes from the origin to the point $\sqrt{\tau}$. The practical consequence is that, even though the cuts may not yet overlap, it might still not be possible to get a good numerical convergence for high values of δ.

With this, all the needed ingredients to solve the Bethe-Salpeter equation have been gathered and analyzed, and it is possible to solve the equation numerically.

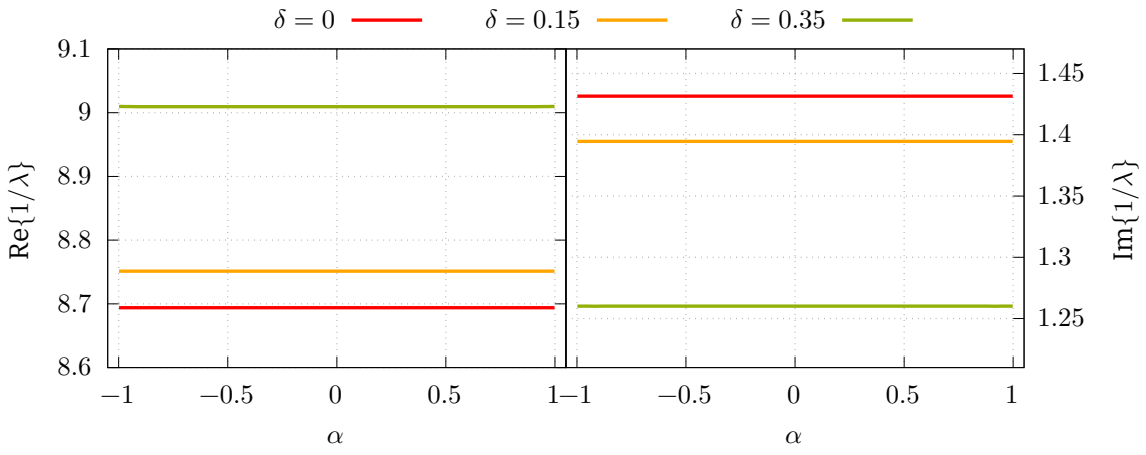

Figure 5.10: Inverse eigenvalues $1/\lambda$ for three different values of δ as functions of α.

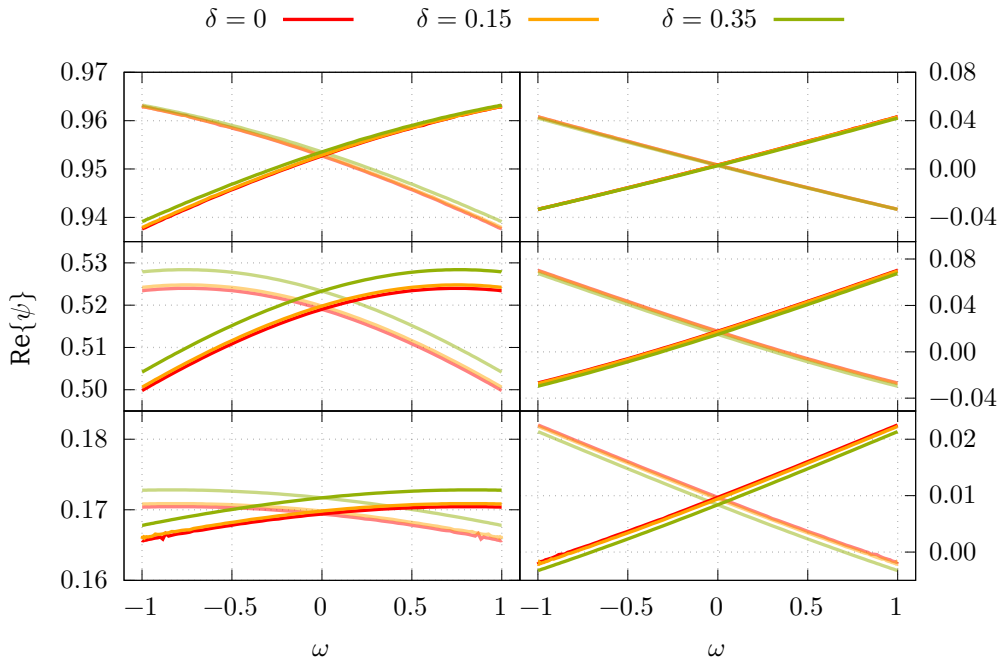

Figure 5.11: ω dependency of the real (left) and imaginary (right) parts of the Bethe-Salpeter amplitude ψ for a value of $\alpha = -0.602$ and three values of δ and three values of x: 1.27 (top), 23.89 (middle) and 125.50 (bottom). The faint lines are the results for $\alpha = 0.602$.

Figure 5.10 shows the inverse eigenvalues $1/\lambda$ for a value of $\beta = 4$, $\sqrt{t} = 0.2 + 0.8i$, $N_x = 128$ and $N_z = 96$ and three different values of $\delta = \{0, 0.15, 0.35\}$. The integration path used was the one from section 3.4.3, which still avoids the cuts. For the selected value of $\sqrt{t}$, the maximum δ is at $|\delta| = \frac{8}{15}$.

Figure 5.10 shows that, as expected, there is no α dependence of the eigenvalues. It also shows that incrasing the value of δ leads to increased $1/\lambda$. The dependency of the amplitudes ψ on the ω variable is seen in figure 5.11.

The amplitude ψ does not seem to be much affected by the value of δ in its ω dependency, as seen in figure 5.11. The symmetry of equation (5.26) is also visible in the results. The dependence on x is shown in figure 5.12. As in the unequal masses case, the variation with the value of δ is more pronounced on the imaginary part. The results have, nevertheless, a similar form to the regular case of chapter 3. In

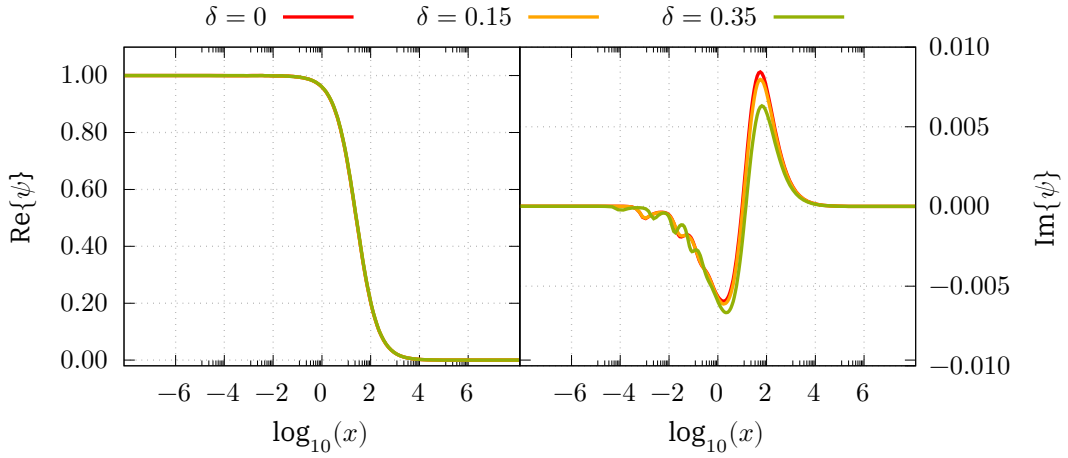

Figure 5.12: x dependency of the real(left) and imaginary (right) parts of the Bethe-Salpeter amplitude ψ for different values of δ and a fixed value of $\omega = -0.24$ and $\alpha = -0.602$.

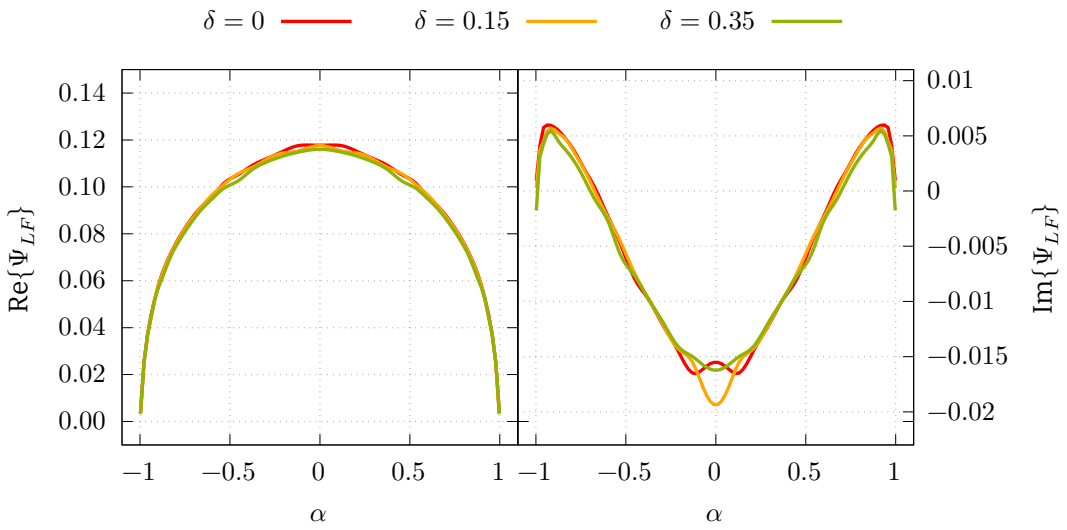

Figure 5.13: Real (left) and imaginary (right) parts of the light-front wavefunction as a function of α, for $x = 0.95$ and three values of δ.

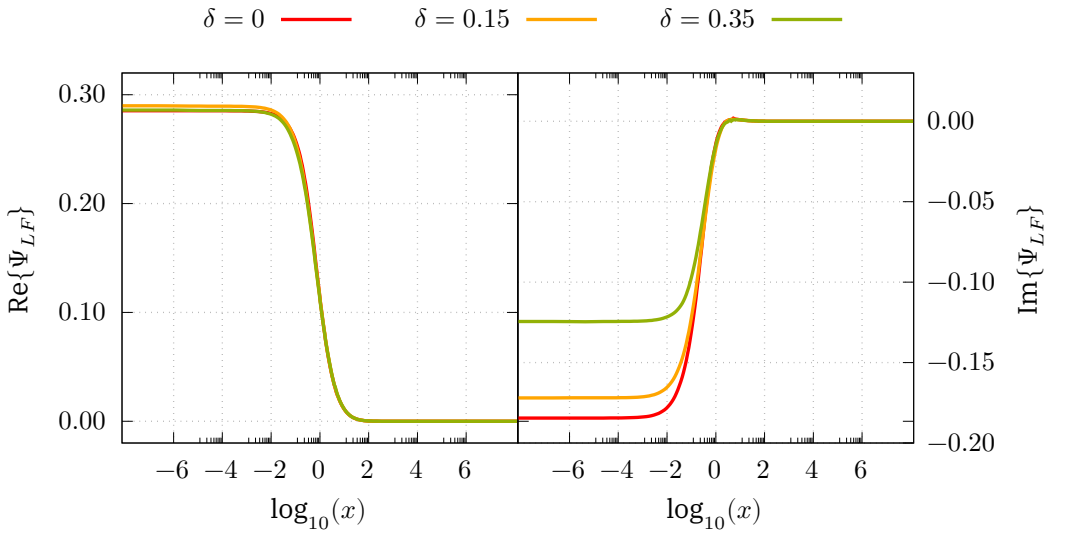

Figure 5.14: Real (left) and imaginary (right) parts of the light-front wavefunction as a function of x, for $\alpha = -0.04$ and three values of δ.

the left plot of 5.12 the three lines are overlapped.

After having obtained numerically the Bethe-Salpeter amplitude, the next step is to calculate the light-front wavefunction and the parton distribution amplitude for the complex conjugate masses case. The results for the LFWF, obtained from the previously calculated amplitudes ψ are presented in figure 5.13 for the α dependence and in figure 5.14 for the x dependence.

The light-front wavefunctions and the parton distribution amplitudes were normalized like in section 4.3.

Again, both the α and the x dependence do not differ by much from different values of δ, however, there is a small difference in the x dependence. The curves look similar to the regular case of $\delta = 0$.

Finally, the parton distribution amplitudes obtained from the LFWFs are shown in figure 5.15. In conclusion, the obtained results demonstrate that it is possible to tackle the complex conjugate masses problem with the contour deformation method — at least when the mass poles are not too far from the real axis, that is, a low value of δ.

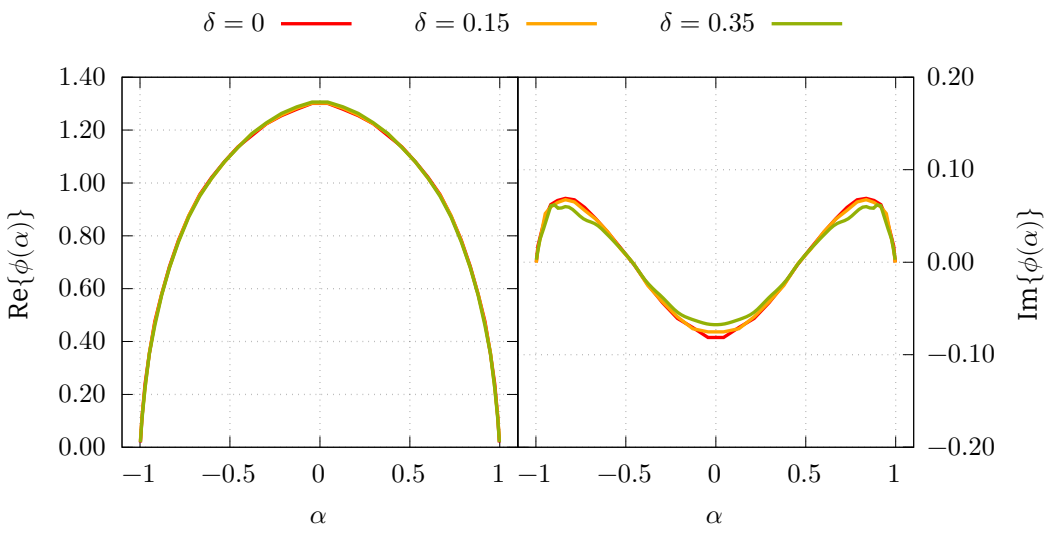

Figure 5.15: Parton distribution amplitudes $\phi(\alpha)$, for three different values of δ.

Chapter 6

Concluding Remarks

In this work we explored a new method for calculating light-front wavefunctions (LFWF) based on contour deformations. Starting with their successful application in the calculation of the Bethe-Salpeter wavefunction, the main motivation for this work was to understand how the contour deformation method could be extended to calculate the LFWF. From the LFWFs other hadronic structure functions can be extracted, such as the PDFs.

The results of chapter 4 clearly show that the contour deformation method is well-suited for the calculation of the LFWFs for the scalar model. The validity of the obtained results is also demonstrated by the excellent agreement with the results from the Nakanishi method, which is well established in the community.

The contour deformation method has several advantages. It is computationally fast, as the solution of the BSE in equation (3.34) requires only two integrations (in the rest frame): one in x' and one in ω'. By contrast, the Nakanishi method, not only needs more integrations, as seen in equations (3.17) and (3.20) but also requires a matrix inversion (equation (3.21)), making it computationally more expensive. Additionally, the analytic continuation from the Schlessinger method is computationally also not very demanding, so the calculation of equation (3.66) does not add a significant overhead.

Second, the contour deformation method can be used even in cases where the full analytic structure of the interaction is not known, as it is the case for many practical calculations in QCD. In principle, if one can find an integration region that is free of singularities, then the method can be applied without difficulties. Finally, the contour deformation method is also applicable beyond the physical threshold, giving access to the resonance spectrum.

The results in chapter 5 are encouraging because they demonstrate that the contour deformation method can be applied in systems that mimic two characteristics that are expected of QCD calculations. First, the unequal mass case will be useful due to the different masses of the quark flavors. This aspect will be particularly relevant in the study of mesons that, for example, combine light up and down quarks with heavier flavors, like the strange or the charm. Second, the fact that the contour deformation method is capable handling complex conjugate poles will be helpful when working with dynamically calculated quark propagators.

Naturally, even though the contour deformation method proved successful, some caveats remain. The first one is the limitation mentioned in equation (3.47) which prevents calculations for values of $\sqrt{t} = iM/2m$ on the imaginary axis, i.e., for a real bound-state mass M. For practical calculation, it is necessary to make $\sqrt{t}$ slightly complex. Taking the limit $\mathrm{Re}\{\sqrt{t}\} \to 0$ becomes increasingly hard in the computational point of view, as the cuts get closer to the integration contour. The same happens for the limit $\beta = \mu/m \to 0$, i.e., for a vanishing exchange particle mass. This issue may be resolved by using the Schlessinger method to extrapolate from the results calculated in regions where the computation

is not very demanding.

The second caveat is related to the Schlessinger method itself. Although it is very powerful and capable of producing good results, as demonstrated by the results of the contour deformation method, a more detailed and systematic study of its properties and numerical stability is desirable. In line with the comments of the end of section 3.5.1, it is usually necessary to fine-tune the number of points used as input to the Schlessinger method based on the properties of the target function. For example, in problems where it is hard to obtain a good precision on the input points, using too many of them might create a large deviation from the correct function. On the other hand, using fewer points as input might not capture enough detail from the target function, again spoiling the analytic continuation. During this work, we found that the best results were obtained by using between 24 and 48 input points.

It is also important to note that the order in which the points are used in the determination of the analytic continuation will lead to different coefficients of the continued fraction in equation (3.80) — a specific order may be more accurate than another. For example, a slight deviation of one of the input points will propagate to all the subsequent coefficients of the continued fraction through the recurrence relations of equation (3.84).

All these issues can, however, be mitigated if one takes some time to experiment with the number of input points in the Schlessinger method to get an idea of its behavior before doing actual calculations. If one is mindful of these caveats, then the contour deformation method is stable, fast, and very effective, as exemplified by the results presented in this work.

In the near future, there are, at least, two lines of work that can derive from this work. The first is the adaptation of the contour deformation method to QCD, based on the work of chapter 5, to calculate LFWF and distribution amplitudes of hadrons.

The second is focused on the study of the correlation functions in section 2.5.1, from where a wide range of hadronic structure observables can be extracted in a similar way to how the LFWF can be extracted from the BSWF. Given a method to calculate these correlation functions, then, in principle, one can apply the contour deformation method in the same way for those functions, such as the generalized parton and transverse momentum distributions. The construction of the Electron-Ion Collider at the Brookhaven National Laboratory [15] and the COMPASS++/AMBER facility at CERN [16] provides a strong motivation for such kinds of studies into the structure of hadrons on the light-front.

Bibliography

[1] F. Halzen and A. D. Martin. *QUARKS AND LEPTONS: AN INTRODUCTORY COURSE IN MODERN PARTICLE PHYSICS*. 1984. ISBN: 978-0-471-88741-6.

[2] A. D. Angelis and M. J. M. Pimenta. *Introduction to Particle and Astroparticle Physics. Questions to the Universe*. Undergraduate Lecture Notes in Physics. Springer, Milano, 2015. DOI: https://doi.org/10.1007/978-88-470-2688-9.

[3] M Gell-Mann. "THE EIGHTFOLD WAY: A THEORY OF STRONG INTERACTION SYMMETRY". In: (Mar. 1961). DOI: 10.2172/4008239. URL: https://www.osti.gov/biblio/4008239.

[4] M. Gell-Mann. "A schematic model of baryons and mesons". In: *Physics Letters* 8.3 (1964), pp. 214–215. ISSN: 0031-9163. DOI: https://doi.org/10.1016/S0031-9163(64)92001-3. URL: https://www.sciencedirect.com/science/article/pii/S0031916364920013.

[5] G Zweig. *An SU_3 model for strong interaction symmetry and its breaking; Version 1*. Tech. rep. Geneva: CERN, 1964. URL: https://cds.cern.ch/record/352337.

[6] G Zweig. "An SU_3 model for strong interaction symmetry and its breaking; Version 2". In: (1964). Version 1 is CERN preprint 8182/TH.401, Jan. 17, 1964, 80 p. URL: https://cds.cern.ch/record/570209.

[7] E. D. Bloom et al. "High-Energy Inelastic $e-p$ Scattering at 6° and 10°". In: *Phys. Rev. Lett.* 23 (16 1969), pp. 930–934. DOI: 10.1103/PhysRevLett.23.930. URL: https://link.aps.org/doi/10.1103/PhysRevLett.23.930.

[8] G. Dissertori. "The Determination of the Strong Coupling Constant". In: *The Standard Theory of Particle Physics* (2016), pp. 113–128. ISSN: 1793-1339. DOI: 10.1142/9789814733519_0006. URL: http://dx.doi.org/10.1142/9789814733519_0006.

[9] J. Greensite. *An introduction to the Confinement Problem*. 1st ed. Springer-Verlag Berlin Heidelberg, 2011. ISBN: 978-3-642-14382-3. DOI: 10.1007/978-3-642-14382-3.

[10] C. Gattringer and C. B. Lang. *Quantum Chromodynamics on the Lattice. An Introductory Presentation*. Springer-Verlag Berlin Heidelberg, 2010. ISBN: 978-3-642-01849-7. DOI: 10.1007/978-3-642-01850-3.

[11] S. Capstick and W. Roberts. "Quark models of baryon masses and decays". In: *Prog. Part. Nucl. Phys.* 45 (2000), S241–S331. DOI: 10.1016/S0146-6410(00)00109-5. arXiv: nucl-th/0008028.

[12] S. Scherer. "Introduction to chiral perturbation theory". In: *Adv. Nucl. Phys.* 27 (2003). Ed. by J. W. Negele and E. W. Vogt, p. 277. arXiv: hep-ph/0210398.

[13] G. Eichmann et al. "Baryons as relativistic three-quark bound states". In: *Progress in Particle and Nuclear Physics* 91 (2016), pp. 1–100. ISSN: 0146-6410. DOI: https://doi.org/10.1016/j.ppnp.2016.07.001. URL: https://www.sciencedirect.com/science/article/pii/S0146641016300424.

[14] H. Sanchis-Alepuz and R. Williams. “Hadronic Observables from Dyson-Schwinger and Bethe-Salpeter equations”. In: *J. Phys. Conf. Ser.* 631.1 (2015). Ed. by N. E. Mavromatos et al., p. 012064. DOI: 10.1088/1742-6596/631/1/012064. arXiv: 1503.05896 [hep-ph].

[15] A. Accardi et al. “Electron Ion Collider: The Next QCD Frontier: Understanding the glue that binds us all”. In: *Eur. Phys. J. A* 52.9 (2016). Ed. by A. Deshpande, Z. E. Meziani, and J. W. Qiu, p. 268. DOI: 10.1140/epja/i2016-16268-9. arXiv: 1212.1701 [nucl-ex].

[16] B. Adams et al. “Letter of Intent: A New QCD facility at the M2 beam line of the CERN SPS (COMPASS++/AMBER)”. In: (Aug. 2018). arXiv: 1808.00848 [hep-ex].

[17] G. Eichmann. *QCD and Hadron Physics Lecture Notes*. 2020. URL: http://cftp.tecnico.ulisboa.pt/~gernot.eichmann/lecture-notes.

[18] G. Aad et al. “Determination of the parton distribution functions of the proton from ATLAS measurements of differential $W^{\pm}$ and Z boson production in association with jets”. In: *JHEP* 07 (2021), p. 223. DOI: 10.1007/JHEP07(2021)223. arXiv: 2101.05095 [hep-ex].

[19] P. Zyla et al. “Review of Particle Physics”. In: *PTEP* 2020.8 (2020), p. 083C01. DOI: 10.1093/ptep/ptaa104.

[20] K. Cichy. “Progress in x-dependent partonic distributions from lattice QCD”. In: *38th International Symposium on Lattice Field Theory*. Oct. 2021. arXiv: 2110.07440 [hep-lat].

[21] H.-W. Lin et al. “Parton distributions and lattice QCD calculations: a community white paper”. In: *Prog. Part. Nucl. Phys.* 100 (2018), pp. 107–160. DOI: 10.1016/j.ppnp.2018.01.007. arXiv: 1711.07916 [hep-ph].

[22] M. Constantinou. “The x-dependence of hadronic parton distributions: A review on the progress of lattice QCD”. In: *Eur. Phys. J. A* 57.2 (2021), p. 77. DOI: 10.1140/epja/s10050-021-00353-7. arXiv: 2010.02445 [hep-lat].

[23] C. Mezrag, H. Moutarde, and J. Rodriguez-Quintero. “From Bethe–Salpeter Wave functions to Generalised Parton Distributions”. In: *Few Body Syst.* 57.9 (2016), pp. 729–772. DOI: 10.1007/s00601-016-1119-8. arXiv: 1602.07722 [nucl-th].

[24] F. E. Serna et al. “Distribution amplitudes of heavy mesons and quarkonia on the light front”. In: *Eur. Phys. J. C* 80.10 (2020), p. 955. DOI: 10.1140/epjc/s10052-020-08517-3. arXiv: 2008.09619 [hep-ph].

[25] K. D. Bednar, I. C. Cloët, and P. C. Tandy. “Distinguishing Quarks and Gluons in Pion and Kaon Parton Distribution Functions”. In: *Phys. Rev. Lett.* 124.4 (2020), p. 042002. DOI: 10.1103/PhysRevLett.124.042002. arXiv: 1811.12310 [nucl-th].

[26] S.-S. Xu et al. “Pion and kaon valence-quark parton quasidistributions”. In: *Phys. Rev. D* 97.9 (2018), p. 094014. DOI: 10.1103/PhysRevD.97.094014. arXiv: 1802.09552 [nucl-th].

[27] P. A. M. Dirac. “Forms of Relativistic Dynamics”. In: *Rev. Mod. Phys.* 21 (3 1949), pp. 392–399. DOI: 10.1103/RevModPhys.21.392. URL: https://link.aps.org/doi/10.1103/RevModPhys.21.392.

[28] G. A. Miller and B. C. Tiburzi. “The Relation Between Equal-Time and Light-Front Wave Functions”. In: *Phys. Rev. C* 81 (2010), p. 035201. DOI: 10.1103/PhysRevC.81.035201. arXiv: 0911.3691 [nucl-th].

[29] C. Lorce, B. Pasquini, and M. Vanderhaeghen. “Unified framework for generalized and transverse-momentum dependent parton distributions within a 3Q light-cone picture of the nucleon”. In: *JHEP* 05 (2011), p. 041. DOI: 10.1007/JHEP05(2011)041. arXiv: 1102.4704 [hep-ph].

[30] N. Nakanishi. “Partial-Wave Bethe-Salpeter Equation”. In: *Phys. Rev.* 130 (3 1963), pp. 1230–1235. DOI: 10.1103/PhysRev.130.1230. URL: https://link.aps.org/doi/10.1103/PhysRev.130.1230.

[31] C. L. G. Gomez. “Minkowski space Bethe-Salpeter equation within Nakanishi representation”. en. PhD thesis. Universidade Estadual Paulista, Instituto de Física Teórica, 2016, p. 163. URL: http://hdl.handle.net/11449/144735.

[32] T. Frederico, G. Salmè, and M. Viviani. “Quantitative studies of the homogeneous Bethe-Salpeter equation in Minkowski space”. In: *Phys. Rev. D* 89 (1 2014), p. 016010. DOI: 10.1103/PhysRevD.89.016010. URL: https://link.aps.org/doi/10.1103/PhysRevD.89.016010.

[33] G. Eichmann et al. “Scattering amplitudes and contour deformations”. In: *Phys. Rev. D* 100 (9 2019), p. 094001. DOI: 10.1103/PhysRevD.100.094001. URL: https://link.aps.org/doi/10.1103/PhysRevD.100.094001.

[34] S. Pokorski. *Gauge Field Theories*. 2nd ed. Cambridge Monographs on Mathematical Physics. Cambridge University Press, 2000. DOI: 10.1017/CBO9780511612343.

[35] J. F. Donoghue, E. Goldwich, and B. R. Holstein. *Dynamics of the Standard Model*. 2nd ed. Cambridge Monographs on Particle Physics, Nuclear Physics and Cosmology. Cambridge University Press, 2014. DOI: https://doi.org/10.1017/CBO9780511803512.

[36] R. Aaij et al. “Observation of New Resonances Decaying to $J/\psi K^+$ and $J/\psi\phi$”. In: *Phys. Rev. Lett.* 127 (8 2021), p. 082001. DOI: 10.1103/PhysRevLett.127.082001. URL: https://link.aps.org/doi/10.1103/PhysRevLett.127.082001.

[37] LHCb collaboration. “Observation of structure in the J/ψ-pair mass spectrum”. In: *Science Bulletin* 65.23 (2020), pp. 1983–1993. ISSN: 2095-9273. DOI: https://doi.org/10.1016/j.scib.2020.08.032. URL: https://www.sciencedirect.com/science/article/pii/S2095927320305685.

[38] M. Ablikim et al. “Observation of a Charged Charmoniumlike Structure in $e^+e^- \to \pi^+\pi^- J/\psi$ at $\sqrt{s}$=4.26 GeV”. In: *Phys. Rev. Lett.* 110 (25 2013), p. 252001. DOI: 10.1103/PhysRevLett.110.252001. URL: https://link.aps.org/doi/10.1103/PhysRevLett.110.252001.

[39] Z. Q. Liu et al. “Study of $e^+e^- \to \pi^+\pi^- J/\psi$ and Observation of a Charged Charmoniumlike State at Belle”. In: *Phys. Rev. Lett.* 110 (25 2013), p. 252002. DOI: 10.1103/PhysRevLett.110.252002. URL: https://link.aps.org/doi/10.1103/PhysRevLett.110.252002.

[40] R. Aaij et al. “Observation of $J/\psi p$ Resonances Consistent with Pentaquark States in $\Lambda_b^0 \to J/\psi K^- p$ Decays”. In: *Phys. Rev. Lett.* 115 (7 2015), p. 072001. DOI: 10.1103/PhysRevLett.115.072001. URL: https://link.aps.org/doi/10.1103/PhysRevLett.115.072001.

[41] E. E. Salpeter and H. A. Bethe. “A Relativistic Equation for Bound-State Problems”. In: *Phys. Rev.* 84 (6 1951), pp. 1232–1242. DOI: 10.1103/PhysRev.84.1232. URL: https://link.aps.org/doi/10.1103/PhysRev.84.1232.

[42] R. W. McAllister and R. Hofstadter. “Elastic Scattering of 188-Mev Electrons from the Proton and the Alpha Particle”. In: *Phys. Rev.* 102 (3 1956), pp. 851–856. DOI: 10.1103/PhysRev.102.851. URL: https://link.aps.org/doi/10.1103/PhysRev.102.851.

[43] J. D. Bjorken. “Asymptotic Sum Rules at Infinite Momentum”. In: *Phys. Rev.* 179 (1969), pp. 1547–1553. DOI: 10.1103/PhysRev.179.1547.

[44] G. Altarelli and G. Parisi. “Asymptotic freedom in parton language”. In: *Nuclear Physics B* 126.2 (1977), pp. 298–318. ISSN: 0550-3213. DOI: https://doi.org/10.1016/0550-3213(77)90384-4. URL: https://www.sciencedirect.com/science/article/pii/0550321377903844.

[45] Y. L. Dokshitzer. “Calculation of the Structure Functions for Deep Inelastic Scattering and e+ e- Annihilation by Perturbation Theory in Quantum Chromodynamics.” In: *Sov. Phys. JETP* 46 (1977), pp. 641–653.

[46] V. N. Gribov and L. N. Lipatov. “Deep inelastic e p scattering in perturbation theory”. In: *Sov. J. Nucl. Phys.* 15 (1972), pp. 438–450.

[47] F. J. Dyson. “The S Matrix in Quantum Electrodynamics”. In: *Phys. Rev.* 75 (11 1949), pp. 1736–1755. DOI: 10.1103/PhysRev.75.1736. URL: https://link.aps.org/doi/10.1103/PhysRev.75.1736.

[48] J. Schwinger. “On the Green’s functions of quantized fields. I”. In: *Proceedings of the National Academy of Sciences* 37.7 (1951), pp. 452–455. ISSN: 0027-8424. DOI: 10.1073/pnas.37.7.452. eprint: https://www.pnas.org/content/37/7/452.full.pdf. URL: https://www.pnas.org/content/37/7/452.

[49] C. D. Roberts and A. G. Williams. “Dyson-Schwinger equations and their application to hadronic physics”. In: *Progress in Particle and Nuclear Physics* 33 (1994), pp. 477–575. ISSN: 0146-6410. DOI: https://doi.org/10.1016/0146-6410(94)90049-3. URL: https://www.sciencedirect.com/science/article/pii/0146641094900493.

[50] G. C. Wick. “Properties of Bethe-Salpeter Wave Functions”. In: *Phys. Rev.* 96 (4 1954), pp. 1124–1134. DOI: 10.1103/PhysRev.96.1124. URL: https://link.aps.org/doi/10.1103/PhysRev.96.1124.

[51] R. E. Cutkosky. “Solutions of a Bethe-Salpeter Equation”. In: *Phys. Rev.* 96 (4 1954), pp. 1135–1141. DOI: 10.1103/PhysRev.96.1135. URL: https://link.aps.org/doi/10.1103/PhysRev.96.1135.

[52] G. A. Miller and B. C. Tiburzi. “The Relation Between Equal-Time and Light-Front Wave Functions”. In: *Phys. Rev. C* 81 (2010), p. 035201. DOI: 10.1103/PhysRevC.81.035201. arXiv: 0911.3691 [nucl-th].

[53] N. Nakanishi. “Partial-Wave Bethe-Salpeter Equation”. In: *Phys. Rev.* 130 (3 1963), pp. 1230–1235. DOI: 10.1103/PhysRev.130.1230. URL: https://link.aps.org/doi/10.1103/PhysRev.130.1230.

[54] J.-L. Zhang et al. “Measures of pion and kaon structure from generalised parton distributions”. In: *Physics Letters B* 815 (2021), p. 136158. ISSN: 0370-2693. DOI: 10.1016/j.physletb.2021.136158. URL: http://dx.doi.org/10.1016/j.physletb.2021.136158.

[55] K. Raya et al. *Revealing pion and kaon structure via generalised parton distributions*. 2021. arXiv: 2109.11686 [hep-ph].

[56] W. de Paula et al. “Observing the Minkowskian dynamics of the pion on the null-plane”. In: *Phys. Rev. D* 103 (1 2021), p. 014002. DOI: 10.1103/PhysRevD.103.014002. URL: https://link.aps.org/doi/10.1103/PhysRevD.103.014002.

[57] W. H. Press et al. *Numerical Recipes in C. The Art of Scientific Computing*. 2nd ed. Cambridge University Press, 1992. ISBN: 0-521-43108-5.

[58] L. Schlessinger. “Use of Analyticity in the Calculation of Nonrelativistic Scattering Amplitudes”. In: *Phys. Rev.* 167 (5 1968), pp. 1411–1423. DOI: 10.1103/PhysRev.167.1411. URL: https://link.aps.org/doi/10.1103/PhysRev.167.1411.

[59] C. Alexandrou et al. “Pion and kaon $\langle x3 \rangle$ from lattice QCD and PDF reconstruction from Mellin moments”. In: *Phys. Rev. D* 104.5 (2021), p. 054504. DOI: 10.1103/PhysRevD.104.054504. arXiv: 2104.02247 [hep-lat].

[60] C. Shi and I. C. Cloët. “Intrinsic Transverse Motion of the Pion’s Valence Quarks”. In: *Phys. Rev. Lett.* 122.8 (2019), p. 082301. DOI: 10.1103/PhysRevLett.122.082301. arXiv: 1806.04799 [nucl-th].

[61] L. Chang et al. “Imaging dynamical chiral symmetry breaking: pion wave function on the light front”. In: *Phys. Rev. Lett.* 110.13 (2013), p. 132001. DOI: 10.1103/PhysRevLett.110.132001. arXiv: 1301.0324 [nucl-th].

[62] M. Abramowitz and I. A. Stegun. *Handbook of mathematical functions*. 10th ed. National Bureau of Standards - Applied Mathematics Series. Dover Publications, 1964. ISBN: 0-486-61272-4.

Appendix A

General properties of the G_0 and K branch cuts

In the discussion of the branch cuts of the propagators G_0 and the interaction kernel K, in the context of the numerical solution of the Bethe-Salpeter equation for the scalar model of section 3.2, several branch cuts are found which obey a generic form:

$$f(\chi, z, C) = i\left[z + \chi\sqrt{z^2 + C^2}\right], \tag{A.1}$$

where $z \in \mathbb{R}$, $C = a + ib \in \mathbb{C}$ and $\chi = \{+, -\}$. These curves are parametrized by z, and follow a shape dictated by C. The cuts from equations (3.38) to (3.41) can be written in this form by factorizing $\sqrt{t}$:

$$\begin{aligned} &A(\alpha, \chi)\left[\sqrt{t}\omega + \lambda i\sqrt{t(1-\omega^2) + \frac{1}{(1+\chi\alpha)^2}}\right] \\ &\qquad = (A)(-\sqrt{t}i)\left[i\left(\omega - \lambda\sqrt{\omega^2 - \left(1 + \frac{1}{t(1+\chi\alpha)^2}\right)}\right)\right]. \end{aligned} \tag{A.2}$$

The prefactor $-A\sqrt{t}i$ has the effect of rotatating the plane (besides providing a scale factor), while the parenthesis follows the same behaviour as in the following analysis.

It is only necessary to consider cases where $a > 0$ and $b > 0$, that is, the upper right quadrant. The situation $a > 0$ and $b < 0$ is equivalent to the transformation $C \to C^*$, and the whole structure is mirrored along the imaginary axis. The cases where $a < 0$ can be identified with the transformation $C \to -C$, and as C only enters in (A.1) as C^2, they will be identical to the right half plane cases.

The first observations concern some special points in z.

For the limit $z \to -\infty$, the positive curve ($\chi = +$) starts at the origin. On the other hand, the $\chi = -$ curve starts at $i\infty$, that is, infinitely away from the origin, along the imaginary axis:

$$\lim_{z\to-\infty} i\left[z + \chi\sqrt{z^2 + C^2}\right] = i\left[z + \chi|z|\right] = \begin{cases} i\left[z - z\right] = 0, & \chi = + \\ i\left[z + z\right] = -i\infty, & \chi = - \end{cases}. \tag{A.3}$$

For the limit $z \to \infty$, the roles are reversed: the $\chi = +$ curve ends at $i\infty$, and the $\chi = -$ curve ends at the origin. These limits can be obtained from (A.3) by doing the transformation $z \to -z$.

The points $f(\chi, z=0, C)$ are also of interest. Pluging $z=0$ into equation (A.1) leads to:

$$f(\chi, z=0, C) = i\left[0 + \chi\sqrt{0^2+C^2}\right] = \begin{cases} iC, & \chi = + \\ -iC, & \chi = - \end{cases}, \tag{A.4}$$

where $\sqrt{C^2} = C$ in the upper right quadrant.

By rewriting the square root in the curves $f(\chi, z, C)$

$$f(\chi, z, C) = i\left(z + \chi\sqrt{z^2+C^2}\right) = i\left(z + \chi z\sqrt{1+\frac{C^2}{z^2}}\right) = iz\left(1 + \chi\sqrt{1+\frac{C^2}{z^2}}\right), \tag{A.5}$$

one can get the behaviour of said curves at a point near the origin, by writing the series expansion of the term inside the parenthesis up to second order. Taking the limit $z \to +\infty$ for $\chi = -$ and $z \to -\infty$ for $\chi = +$, to get near the origin:

$$\lim_{z\to\infty} f(-, z, C) = \lim_{z\to\infty} iz\left(1 - \sqrt{1+\frac{C^2}{z^2}}\right) = iz\left(1 - 1 - \frac{1}{2}\frac{C^2}{z^2}\right) = -\frac{iC^2}{2z}, \tag{A.6}$$

$$\lim_{z\to-\infty} f(+, z, C) = \lim_{z'\to\infty} -iz'\left(1 - \sqrt{1-\frac{C^2}{z'^2}}\right) = -iz'\left(1 - 1 - \frac{1}{2}\frac{C^2}{z'^2}\right) = \frac{iC^2}{2z'} = -\frac{iC^2}{2z}, \tag{A.7}$$

where in the last limit the substitution $z \to -z'$ was made so that $z \to -\infty \implies z' \to \infty$. As derived, both curves will follow the iC^2 line near the origin.

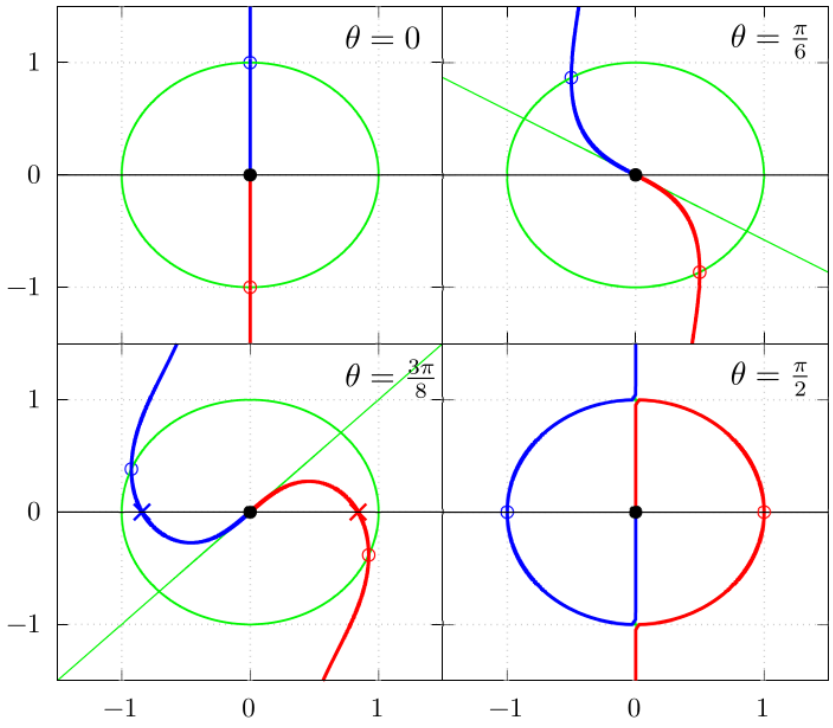

Figure A.1: Plots of the curves $f(+, z, C)$ and $f(-, z, C)$, in blue and red respectively, for four values of $C = e^{i\theta}$: $\theta = 0$, $\theta = \frac{\pi}{6}$, $\theta = \frac{3\pi}{8}$, $\theta = \frac{\pi}{2}$. The circle with radius $|C|$ is in green as well as the iC^2 line. The real axis is the solid black line. The special marked points are the origin, the intersections with the real axis and the intersections with the circle of radius $|C|$.

It is now clear that rotating C into the complex plane by increasing $\arg C$ rotates both curves counterclockwise, while still starting (ending) at the origin and ending (starting) at $i\infty$, for the $\chi = +$ ($\chi = -$) curve. There is a critical value $\varphi = \arg C$ where the curves cross the real axis, which requires a contour deformation when doing the integrations of chapter 3. The rotation $\arg C = \theta$ starts at the imaginary axis, as iC^2 is a pure imaginary number for $C \in \mathbb{R}$. The lines will cross the real axis when $iC^2 \in \mathbb{R}$, that is, iC^2 is a negative number:

$$\arg\left(iC^2\right) \geq \pi \Leftrightarrow 2\theta + \frac{\pi}{2} \geq \pi \implies \theta \geq \frac{\pi}{4}. \tag{A.8}$$

By the definition of the argument, one derives a relation between the real and the imaginary part of C:

$$\arg C = \theta \geq \frac{\pi}{4} = \tan^{-1}\frac{b}{a} \implies \frac{b}{a} \geq 1 \Leftrightarrow b \geq a, \tag{A.9}$$

where, as before, $C = a + ib$. In conclusion, when the imaginary part of C is larger than its real part, the curves cross the real axis and contour deformations is needed.

For the case where C is purely imaginary, $C = ib$, close to the origin, the curves follow along the imaginary axis, in an opposite direction to the $C \in \mathbb{R}$ case. While $z^2 > b^2$, the curves stay in the imaginary axis. When $z^2 < b^2$, the square root term is purely imaginary, and the curves describe a half-circle around the origin, of radius $b = |C|$. When the half circle reaches the imaginary axis again, the condition $z^2 > b^2$ is true again, and the curves follow to $\pm i\infty$. For the $\chi = -$ curve the behaviour is mirrored: it starts at $-i\infty$, followed by the half-circle, then back to the imaginary axis until reaching the origin. In these particular cases, there is no way of designing a path starting at a point inside the $|C|$ radius curve to one on the outside, without crossing any branch cut — contour deformations are not possible.

Going back to (A.2), one can see that the propagator and kernel cuts have a specific form for C:

$$C = i\sqrt{1 + \frac{\kappa^2}{\tau}}, \tag{A.10}$$

where $\kappa > 0 \in \mathbb{R}$, and $\tau \in \mathbb{C}$ is t or x for the propagator and the kernel respectively, and is considered an external variable. It is then possible to define the region where the cuts are confined to, for each specific value of τ, by considering all possible values of $z \in [-1, 1]$ and κ:

$$f(\tau; \lambda; z, \kappa) = \sqrt{\tau}\left(z + \lambda\sqrt{z^2 - \left(1 + \frac{\kappa^2}{\tau}\right)}\right). \tag{A.11}$$

In the first place, the end points $z = \pm 1$ for both the $\lambda = \pm$ curves define two vertical lines in the complex plane:

$$f(\tau, +, z = -1, \kappa) = -\sqrt{\tau} + i\kappa, \qquad f(\tau, +, z = 1, \kappa) = \sqrt{\tau} + i\kappa, \tag{A.12}$$

$$f(\tau, -, z = -1, \kappa) = -\sqrt{\tau} - i\kappa, \qquad f(\tau, -, z = 1, \kappa) = \sqrt{\tau} - i\kappa. \tag{A.13}$$

One line connects the $z = -1$ points, and the other connects the $z = 1$ points. The cuts start at one of the lines and end at the other. In the limit where $\kappa \to 0$, the cuts describe a half-circle around the origin of radius $|\sqrt{\tau}|$:

$$f(\tau, \lambda, z, \kappa \to 0) = \sqrt{\tau}\left(z + \lambda\sqrt{z^2 - 1}\right) = \sqrt{\tau}\left(z + i\lambda\sqrt{1 - z^2}\right). \tag{A.14}$$

The union of both $\lambda = \pm$ half-circles creates a full circle that intersects the vertical lines in (A.13) and (A.12) in four points: $\sqrt{\tau}$, $(\sqrt{\tau})^*$, $-\sqrt{\tau}$ and $-(\sqrt{\tau})^*$. Note that, because κ is strictly larger than zero, both $\sqrt{\tau}$ and $-\sqrt{\tau}$ are never crossed by any cuts.

The $\lambda = +$ curve crosses the $(\sqrt{\tau})^*$ point, while the $\lambda = -$ curve crosses the $-(\sqrt{\tau})^*$ point at

$$|z| = \frac{\frac{\kappa^2}{2} + R^2 - I^2}{R^2 + I^2}, \tag{A.15}$$

where $\sqrt{\tau} = R + iI$. Note that, for some combinations of κ and $\sqrt{\tau}$, this value might be outside the range $z \in [-1, 1]$. In those cases, the cuts are confined in a region outside the circle (A.14), but within the vertical lines (A.13) and (A.12).

The collection of all the derived properties can be seen in figure A.2.

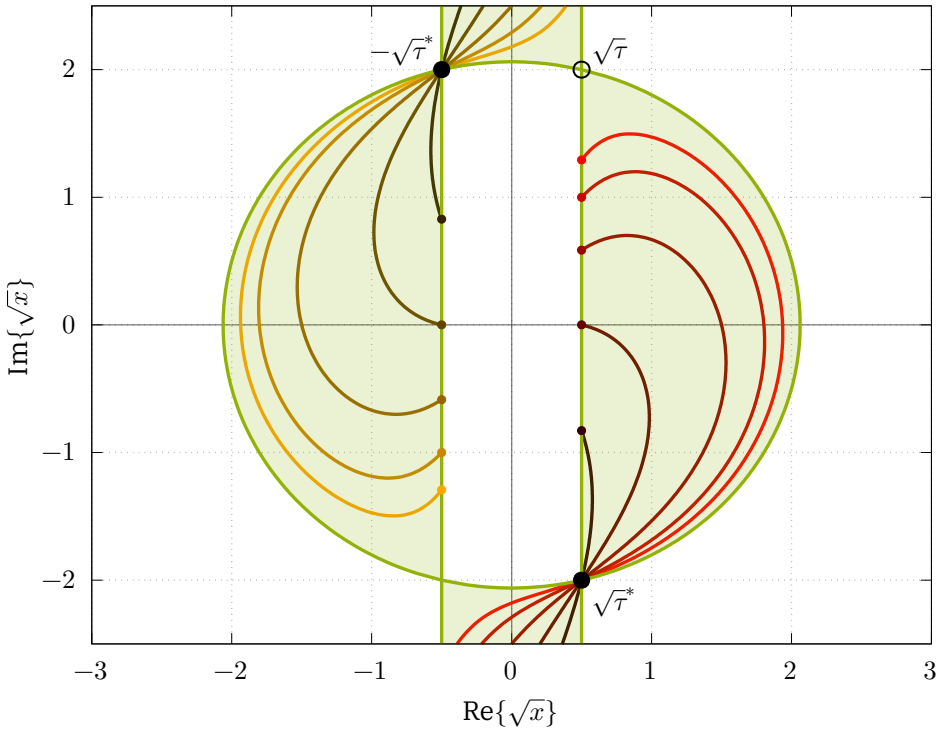

Figure A.2: Regions defined by running through the entire domain of z and κ for the curves $f(\tau, \lambda, z, \kappa)$. In this plot, $\tau = 0.5 + 2i$ and κ takes different values: $0.5, 1.0, 2.0, 4.0, 8.0$. The shaded areas represent regions in the complex plane where there might be cuts.

Appendix B

Numerical integration: Gaussian Quadrature

The goal of numerical integration is to provide an approximation to the numerical value of a definite integral, up to some desired degree of accuracy. In particular, quadrature methods attempt to provide this approximation by a summation of the value of the integrand at a sequence of sampling points inside the integration domain:

$$I = \int_a^b f(x)\,dx \approx \sum_n f(x_n)\,w_n, \tag{B.1}$$

where x_n are the sampling points and w_n a set of weights. Some methods choose x_n to be composed of a set of points separated by the same distance, while others sample at varying intervals. The weights w_n are also sometimes taken as constants, while in other methods they vary with the point x_n.

The Gaussian quadrature is one such method. It uses sampling points that are not equally spaced, as well as a set of w_n which vary for each n, doubling the degrees of freedom and achieving a higher-order approximation for the same number of function evaluations as methods with fixed spacings and weights — although high accuracy requires that the integrand is well approximated by a polynomial function. One can also extend the class of exact results from polynomials to polynomials multiplied by a known *weight* function $W(x)$, which can be used to make the integration better behaved numerically.

Gaussian quadrature methods approximate an integral as [57]:

$$I = \int_a^b W(x)\,f(x)\,dx \approx \sum_j f(x_j)\,w_j. \tag{B.2}$$

The function $W(x)$ dictates the appropriate sampling points and weights so that I is exact if f is a polynomial of degree $2N-1$ or lower. The determination of the sampling points and weights can be done by first considering the scalar product of two functions f and g induced by the weight function $W(x)$:

$$\langle f|g\rangle = \int_a^b W(x)f(x)g(x)dx. \tag{B.3}$$

Equation (B.3) defines a set of orthonormal functions according to that particular scalar product. A list of some of these sets is given in table B.1, according to the $W(x)$ function [62].

The set of sampling points to be used for the N-point Gaussian quadrature algorithm in the interval S is the set of zeros of the N-th order polynomial (induced by $W(x)$ and the domain S). For example, in the case of $S=[-1,1]$ and $W(x)=1$, the set of sampling points for the N-point quadrature is the set of zeros of the Legendre polynomial $L_n(x)$.

$W(x)$	Domain	Set of functions
1	$[-1, 1]$	Legendre Polynomials, $P_j(x)$
$\sqrt{1-x^2}$	$[-1, 1]$	Chebyshev polynomials of the 2nd kind, $U_j(x)$
$\frac{1}{\sqrt{1-x^2}}$	$[-1, 1]$	Chebyshev polynomials of the 1st kind, $T_j(x)$
$(1-x^2)^{\alpha-\frac{1}{2}}$	$[-1, 1]$	Gegenbauer-α polynomials, $C_j^{\alpha}(x)$

Table B.1: List of sets of orthonormal functions induced by the scalar product with different weight functions $W(x)$, with respective domains.

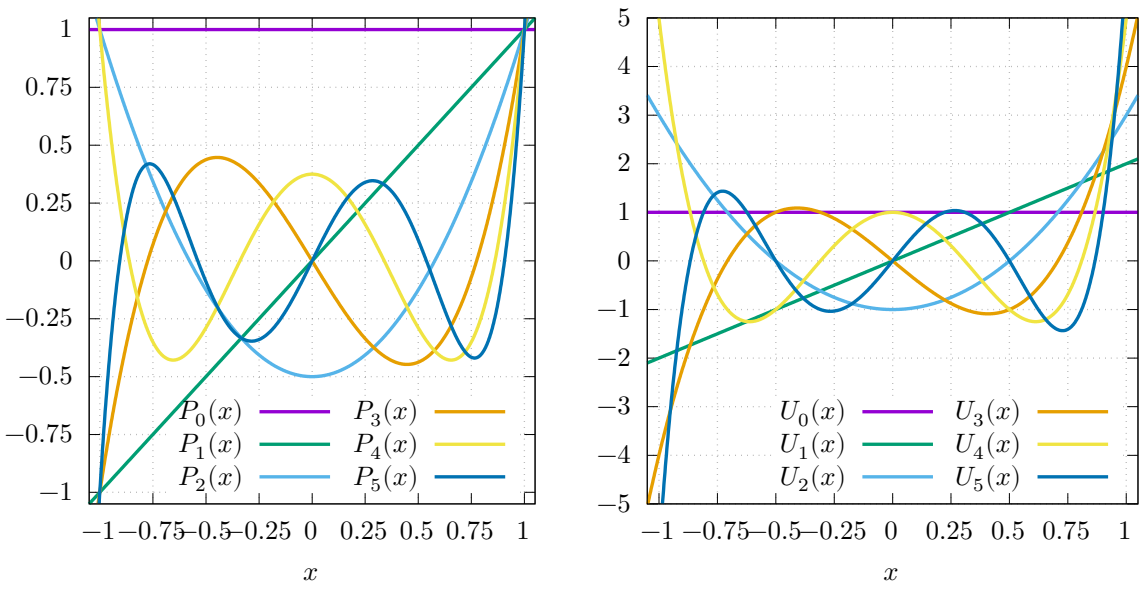

Figure B.1: Plot of the first six Legendre polynomials $P_n(x)$, on the left, and of the first six Chebyshev-U polynomials $U_n(x)$, on the right.

The weights are calculated from the set of sampling points x_n by [57]:

$$w_j = \frac{\langle p_{N-1}|p_{N-1}\rangle}{p_{N-1}(x_j)p_N(x_j)}, \tag{B.4}$$

where p_i is the i-th order orthonormal polynomial, and p_i' is its derivative with respect to x.

In general, the set of orthonormal polynomials can be obtained via recurrence relations, starting with the lowest order, allowing for a simple and quick numerical evaluation. For Legendre polynomials, the recurrence relation is given by [62]:

$$(n+1)P_{n+1}(x) = (2n+1)xP_n(x) - nP_{n-1}(x), \tag{B.5}$$

starting with the initial values of $P_0 = 1$ and $P_1 = x$. The derivative also follows a recurrence relation [62]:

$$(1-x^2)\frac{dP_n(x)}{dx} = -nxP_n(x) + nP_{n-1}(x). \tag{B.6}$$

Similarly, the Chebyshev polynomials (both the 1st and 2nd kind), also follow recurrence relations

[62]:

$$T_{n+1}(x) = 2xT_n(x) - T_{n-1}(x), \qquad T_0 = 1, \qquad T_1 = x, \tag{B.7}$$

$$U_{n+1}(x) = 2xU_n(x) - U_{n-1}(x), \qquad U_0 = 1, \qquad U_1 = 2x. \tag{B.8}$$

The recurrence relation for the derivatives is [62]:

$$(1-x^2)\frac{dT_n(x)}{dx} = -nxT_n(x) + nT_{n-1}(x), \tag{B.9}$$

$$(1-x^2)\frac{dU_n(x)}{dx} = -nxU_n(x) + (n+1)U_{n-1}(x). \tag{B.10}$$

Appendix C

Numerical stability

In the discussions of the propagator and kernel cuts in section 3.4.2, it was argued that in the limit $\mathrm{Im}\{\sqrt{t}\} \to 0$ the propagator cuts are ever closer to the imaginary axis, and there is less space for the path, bringing it closer to the cuts as well. For the kernel a similar situation exists as for $\beta \to 0$ the cuts get closer to the $\sqrt{x}$ point.

Both these situations will require a larger number of points in the integration to better sample the rapid variation of the integrand when near the cuts. On the other hand, a large number of points might be unnecessary if the cuts are far away, and one can very significantly save computational time and memory, as the dimension of the integration matrix (3.78) depends on the square of the number of points.

It is therefore important and instructive to analyze the numerical stability of the contour deformation method. This helps ensure that the numerical solution converges to a solution and how many integration points are needed for some region of the parameters. 2 For that purpose, two cases were studied: in the first, for three values of $\beta = \{4, 1, 0.25\}$ and a fixed value of $\sqrt{t} = 0.2 + 0.8i$, a variation on the number of points N_x was made; in the second, a similiar variation on N_x was made, for three values of $\mathrm{Re}\{\sqrt{t}\} = \{0.20, 0.10, 0.01\}$ and a value of $\beta = 2$ fixed.

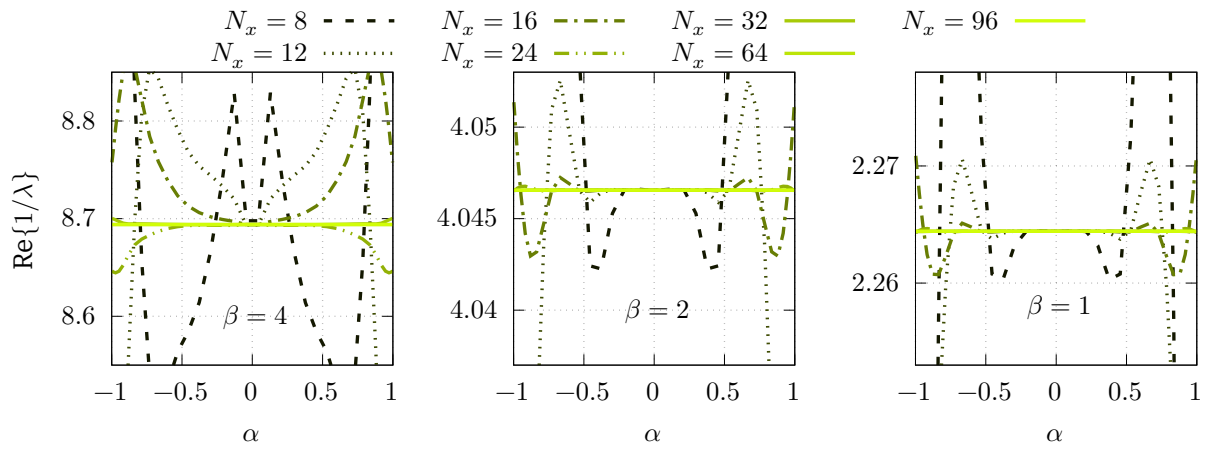

Figure C.1: Inverse eigenvalues $1/\lambda$ obtained for a fixed value of $\sqrt{t} = 0.20 + 0.80i$ and one of three values of β, for various number of points N_x in the integration in x. From left to right: $\beta = 4$, $\beta = 2$ and $\beta = 0.25$.

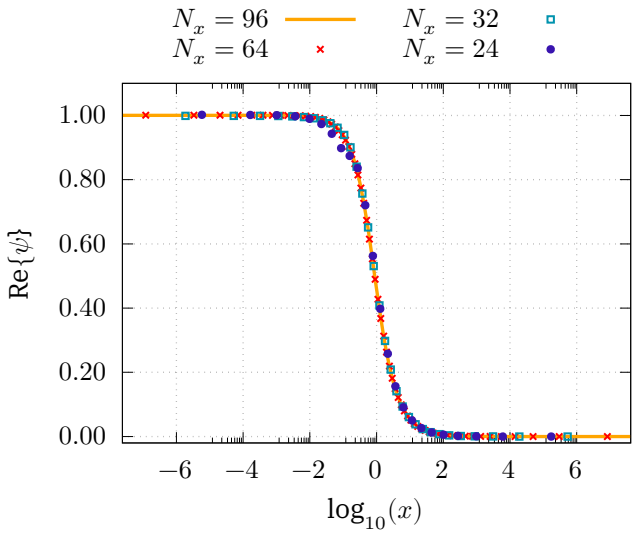

Figure C.2: x dependence in x of the real part of the amplitude ψ, for a fixed value of $\omega \approx 0.02$, $\alpha = -0.602$ and four values of the number of integration points in x, N_x.

A good place to start is by calculating the eigenvalues as it provides a good test for the quality of the numerical calculation — the eigenvalues should not depend on the α variable. In figure C.1 the results, obtained for the real part of the inverse eigenvalue $1/\lambda$ for $N_\omega = 96$ and $N_\alpha = 36$, are presented for different values of N_x.

It is seen in figure C.1 that increasing the number of points N_x improves the results of the eigenvalues. In fact, for the two cases of $\beta = \{1, 4\}$, selecting $N_x \geq 64$ results in good numerical results, as can be seen by the overlapping horizontal lines. The case $\beta = 0.25$ requires more points, and as such, only the line for $N_x = 96$ shows good results. For the $\beta = 0.25$ case, the calculation with $N_x = 8$ failed to converge.

In figure C.2, a comparison between the obtained values of the amplitude is made, for four of the different values of N_x used in figure C.1, and $\beta = 0.25$. A higher number of points provides better coverage in the whole domain of $\sqrt{x}$, mainly at the higher values of $x \gg 1$. For $N_x = 24$ is it possible to see some deviations to the correct curve.

One can repeat the same study by varying the number of points in the ω integration. Figure C.3

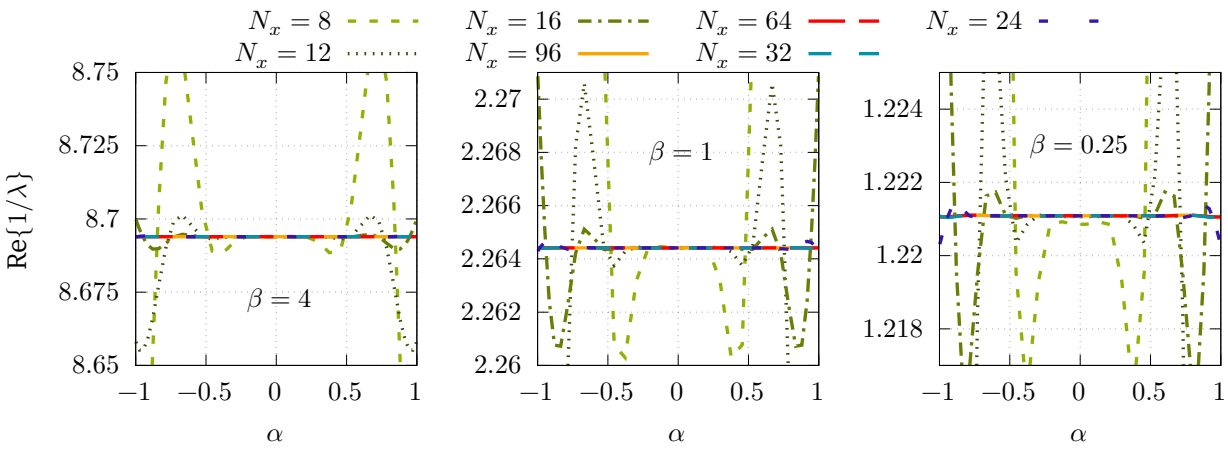

Figure C.3: Inverse eigenvalues $1/\lambda$ obtained for a fixed value of $\sqrt{t} = 0.20 + 0.80i$ and one of three values of β, for various number of points N_ω in the integration in ω.

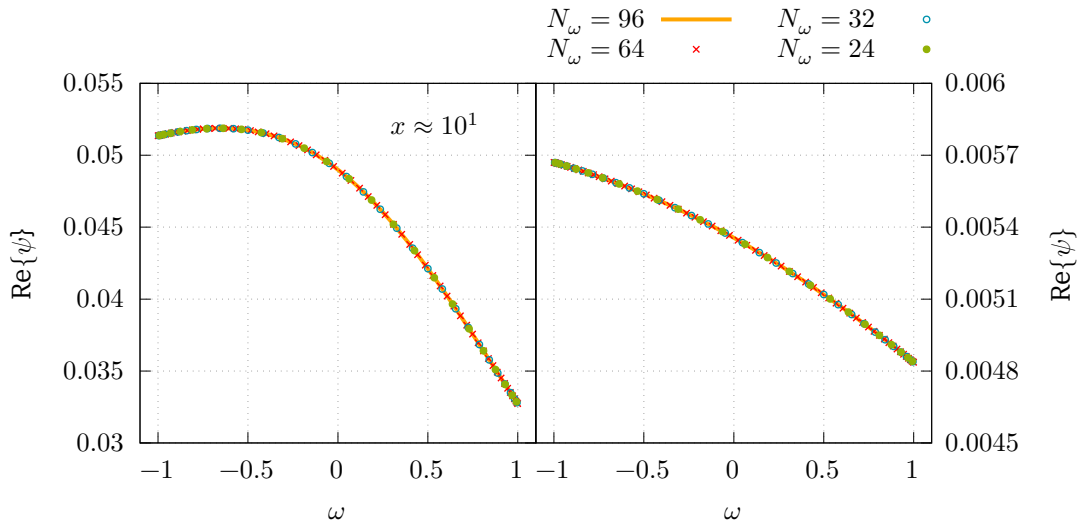

Figure C.4: ω dependence of the real part of the amplitude ψ, for two fixed value of x and $\alpha \approx -0.602$ and four values of the number of integration points in ω, N_ω.

shows the obtained inverse eigenvalues for the same three values of β as in the x case and the same value of $\sqrt{t} = 0.2 + 0.8i$, while varying the number of integration points N_ω and maintaining $N_x = 96$. For the values of $\beta = 4, 1$, a number $N_\omega \geq 32$ provides a good result for the eigenvalues, while a value of $N_\omega = 24$ for the $\beta = 1$ already shows some variation near the $\alpha = \pm 1$ points. For the $\beta = 0.25$ case, it it seems that even the $N_\omega = \{32, 64\}$ cases show a small oscillation near the $\alpha = \pm 1$ points.

In figure C.4 the obtained results for the ω dependence of ψ are shown, for a varying number of integration points N_ω, a value of $\beta = 0.25$ and $\alpha \approx -0.602$.

Having studied how the number of integration points N_x and N_ω influence the numerical outcome, mainly in the eigenvalue for different values of β, it is also instructive to do the same study, but with a fixed β and varying values of Re$\{\sqrt{t}\}$.

In figure C.5 the obtained inverse eigenvalues for different values of N_x are presented, for fixed values $\beta = 2$, Im$\{\sqrt{t}\} = 0.8$ and $N_\omega = 96$. In figure C.6 is presented the same study, but fixing $N_x = 96$ and letting N_ω vary.

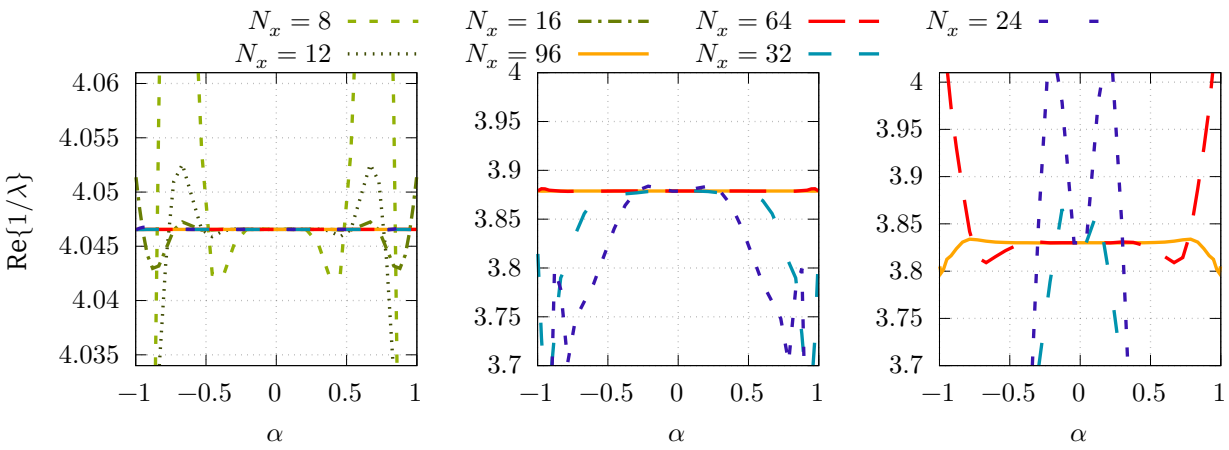

Figure C.5: Inverse eigenvalues $1/\lambda$ obtained for a fixed value of Im$\{\sqrt{t}\} = 0.80$ and one of three values of Re$\{\sqrt{t}\}$, for various number of points N_x in the integration in x. From left to right: Re$\{\sqrt{t}\} = 0.20$, Re$\{\sqrt{t}\} = 0.10$, Re$\{\sqrt{t}\} = 0.01$.

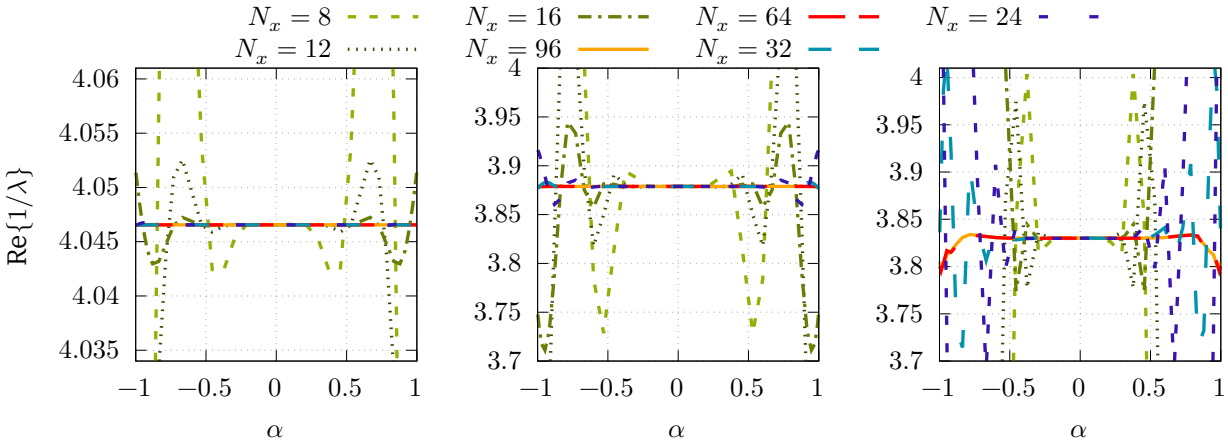

Figure C.6: Inverse eigenvalues $1/\lambda$ obtained for a fixed value of $\mathrm{Im}\{\sqrt{t}\} = 0.80$ and one of three values of $\mathrm{Re}\{\sqrt{t}\}$, for various number of points N_ω in the integration in ω. From left to right: $\mathrm{Re}\{\sqrt{t}\} = 0.20$, $\mathrm{Re}\{\sqrt{t}\} = 0.10$, $\mathrm{Re}\{\sqrt{t}\} = 0.01$.

From figure C.5 one concludes that the numerical method is more sensitive to the value of the real part of $\sqrt{t}$ than the value of β. In fact, for the values of $\mathrm{Re}\{\sqrt{t}\} \leq 0.10$, the numerical solution does not converge to a result for $N_x < 24$.

As $\mathrm{Re}\{\sqrt{t}\} \to 0$, the numerical method becomes increasingly unstable, requiring more integration points. This corresponds to the situation where the cuts in 3.2 get closer to the imaginary axis and the integration path.

The comparison between figures C.5 and C.6 indicates that this numerical problem is more sensitive to the number of points in the x integration than the ω integration.

Having established the numerical behavior of the contour deformation method in the calculation of the BSWF, we now focus our attention to the calculation of the LFWF from the BSWF via equation (3.66).

In the following plots, the influence of N_x and N_ω in the results for the LFWFs and the PDAs is studied. In the following plots, the LFWFs were obtained from the previously calculated BSWFs for the $\beta = 1$ case, and $\sqrt{t} = 0.20 + 0.80i$. In all subsequent plots, the number of points N_{schle} used as input to the Schlessinger method is $N_{schle} = 24$. All plots were normalized as in sections 4.3.

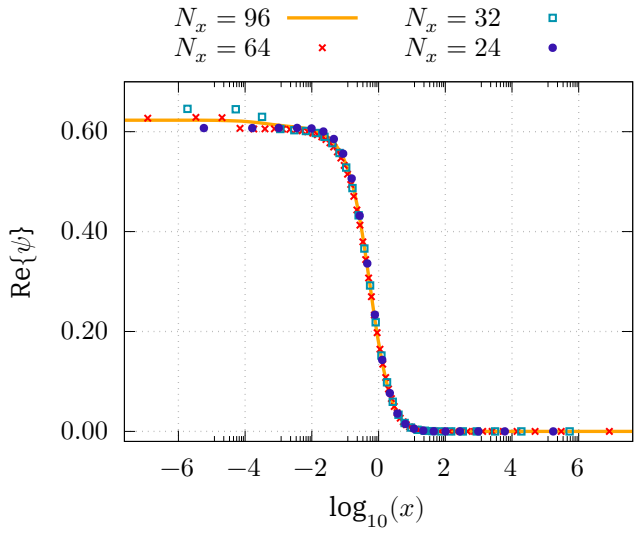

Figure C.7: x dependence of the LFWF for fixed $\alpha = 0.214$, $N_\omega = 96$ and four values of N_x.

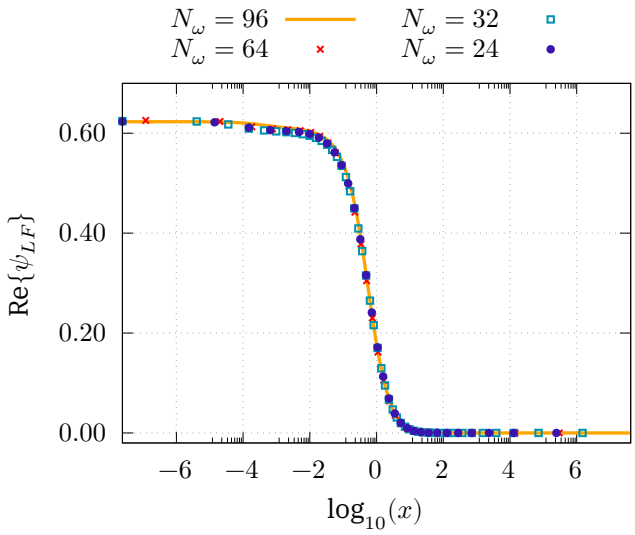

Figure C.8: x dependence of the LFWF for fixed $\alpha = 0.214$, $N_x = 96$ and four values of N_ω.

In figure C.7, the x dependence of the LFWF is shown for $N_\omega = 96$ fixed, and four values of $N_x = \{24, 32, 48, 64\}$. One can see that the calculation of the LFWFs is more sensitive to the number of integration points in x, mainly on the low x region which is more numerically demanding, as discussed in section 4.3.

Figure C.8 also shows the x dependence of the LFWF, but instead for fixed $N_x = 96$ and four values of $N_\omega = \{96, 64, 32, 24\}$. The results also show a deviation for the smaller values of N_ω in the low x region, albeit smaller than in the case for smaller values of N_x. Comparing C.7 and C.8 indicates that the LFWF is more sensible to the number of points in the x integration than on the ω integration.

The variation on the α dependence of the LFWFs with the different values of the number points in the integrations can be inferred by looking at the results from the PDAs, as these carry the properties in α of the LFWFs.

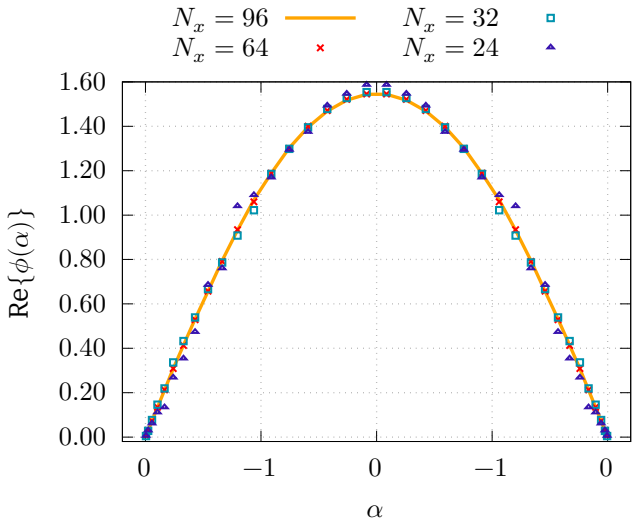

Figure C.9: Real part of the PDA for a fixed number of points in ω $N_\omega = 96$ and four different values of N_x.

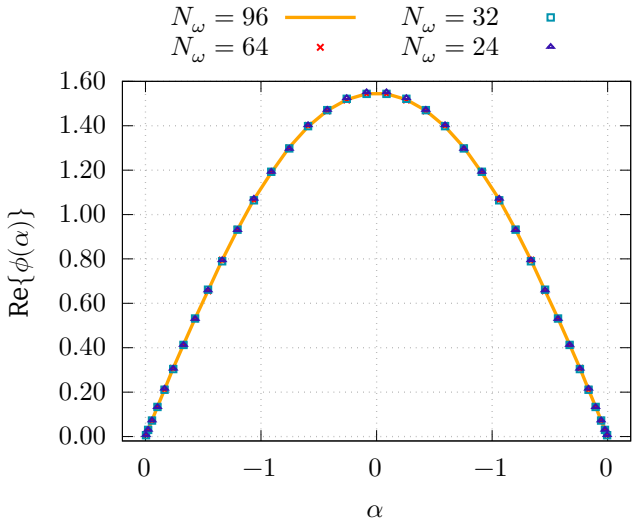

Figure C.10: Real part of the PDA for a fixed number of points in x $N_x = 96$ and four different values of N_ω.

In figure C.9 is shown the obtained PDAs for a fixed $N_\omega = 96$ and different values of N_x, and in figure C.10 $N_x = 96$ is fixed and different values of N_ω are selected. One can see again, that the numerical problem is more sensitive to the number of points in the x integration, which can be seen by the slight deviation for the low values of N_x near the $\alpha = 0$ region, in figure C.9.